2015

Molecular Dynamics Simulation of the Structure, Dynamics and Crystallization of Ionic Liquids under Confinement and Low Temperature

Xiaoxia He
Louisiana State University and Agricultural and Mechanical College, xhe6@tigers.lsu.edu

MOLECULAR DYNAMICS SIMULATION OF THE STRUCTURE, DYNAMICS AND CRYSTALLIZATION OF IONIC LIQUIDS UNDER CONFINEMENT AND LOW TEMPERATURE

A Dissertation

Submitted to the Graduate Faculty of the
Louisiana State University and
Agricultural and Mechanical College
in partial fulfillment of the
requirements for the degree of
Doctor of Philosophy

in

Cain Department of Chemical Engineering

by
Xiaoxia He
M.S., Tianjin University, 2010
B.S., Henan University of Science and Technology, 2008
December 2015

To my Parents

Huaisheng He & Aiqin Liu

my husband

Yuehao Li

and our baby boy

Ethan Li

Acknowledgements

I would like to express my sincere thanks to Dr. Francisco R. Hung for his continuous support of my research. Because of his enthusiasm, inspiration and patience, my research has become a lot of fun for me. His guidance has helped me all this time during my PhD studies. I also want to thank Dr. Erik E. Santiso in North Carolina State University. Thanks to his code and insightful advices, I have got a lot of inspiration on my research projects.

My group members and collaborators are well acknowledged as well. By discussing problems with my colleagues, I have learned a significant amount of techniques and gained knowledge in a much shorter time than that I would have spent if they had not helped me. Thanks to all the group members in Dr. Hung's research group: Mr. Yuwu Chen, Mr. Zenghui Zhang, Ms. Yan Shen and Ms. Rubaiyet Abedin as well as all former members Dr. Joshua Monk, Dr. Ramesh Singh, Dr. Nav Nidhi Rajput, Dr. Thilanga Liyana-Arachchi and Dr. Shivkumar Bale.

My special gratitude is to my husband, Yuehao Li. God has blessed me to meet him in LSU and marry him! He has contributed a great deal to my family and especially to my personal life. Without his encouragement and understanding, it would have been impossible for me to complete this work. He is such an amazing husband, and he is always available to give me good advice when I have trouble, and to comfort me when I am tired.

I sincerely acknowledge funding from the National Science Foundation (NSF) and the Louisiana Alliance for Simulation-Guided Materials Applications (LA-SiGMA). The technical support from HPC-LSU and LONI facilities is greatly acknowledged as well.

Table of Contents

Abstract

Ionic liquids (ILs) have sparked widespread interest due to their peculiar properties and the resulting possibility of manifold applications. In this dissertation, molecular dynamics (MD) simulations have been used to elucidate the dynamics, structure and crystallization of ionic liquids in the bulk and confinement.

First we studied the properties of the ILs [$dmim^+$][Cl^-] and [$emim^+$][NTf_2^-] when they are confined inside nanomaterials such as CMK-3, CMK-5 and an isolated amorphous carbon nanopipe (ACNP). The results indicate that the ions of the ILs form different layers inside these nanomaterials and their dynamics are slower due to the confinement. We also found significant differences in the densities and mobilities of ions caused by pore morphologies. Moreover, the presence of IL adsorbed in the outer surface of an uncharged ACNP in CMK-5 affects the dynamics and the density of an IL adsorbed inside the ACNP, and vice versa.

Biased MD simulations have been performed to study the homogeneous nucleation of IL [$dmim^+$][Cl^-] from its supercooled liquid in the bulk, as well as the heterogeneous nucleation of the same IL near a graphitic surface. The string method in collective variables (SMCV) and Markovian milestoning with Voronoi tessellations, when used in combination with suitable order parameters proposed for molecular crystals, allow us to sketch a minimum free energy path (MFEP) connecting the supercooled liquid and crystal phases, and to determine the free energy and the rates involving in the nucleation processes. The physical significance of the configurations found along these MFEPs is discussed with the help of calculations based on classical nucleation theory, as well as simulation snapshots. Analogies and differences between both nucleation processes are analyzed and discussed.

The simulation work described here is relevant to using ILs as electrolytes in energy-related devices, such as electrochemical double layer capacitors and dye-sensitized solar cells. Furthermore, nucleation of ILs is relevant to developing nanomaterials based on ILs.

Chapter 1 Introduction

In this dissertation we have conducted a series of molecular dynamics (MD) simulation studies with the following objectives: (1) understanding the structure and dynamical properties of liquid phases of ionic liquids (ILs) confined inside nanoporous carbons, and (2) understanding the nucleation of crystal phases of ILs from its supercooled liquid phase, both in the bulk (homogeneous nucleation) and near a graphene surface (heterogeneous nucleation). In addition to their fundamental scientific interest, these research topics are relevant to several practical applications. The first topic is relevant to potential uses of ILs as alternative electrolytes in energy storage devices, such as electrochemical double layer capacitors (EDLCs) and dye-sensitized solar cells (DSSCs), where an electrolyte is in contact with a nanoporous electrode. The second topic is relevant to the rational design of nanomaterials based on organic salts, in particular those where an organic salt solidifies into the pores of a hard template. In the rest of this chapter we provide some limited background on ILs and its applications (Section 1.1), uses of ILs as alternative electrolytes in EDLCs (Section 1.2) and the properties of ILs confined in different morphologies (Section 1.3). Furthermore, we give some introductions to ILs-based nanomaterials (Section 1.4), the nucleation theories for both homogeneous and heterogeneous nucleation (Section 1.5) and the molecular simulation methods involving in studying ILs (Section 1.6).

1.1 Ionic liquids (ILs) and its applications

ILs are salts with melting points below the boiling point of water[1]; therefore a significant number of ILs are in liquid state at room temperature (named RTILs; room temperature ionic liquids). ILs are made of ions that are poorly coordinated, or at least one ion has a delocalized

charge and one component is organic; therefore they have relatively low melting points compared to salts such as NaCl. The properties of ILs are highly tunable; as many as 10^9 to 10^{18} ILs could be formed by varying the cations and the anions[1-2]. Billions of ILs have been synthesized by selecting the proper combination of cations and anions for special applications. For this reason ILs have been termed "designer solvents".

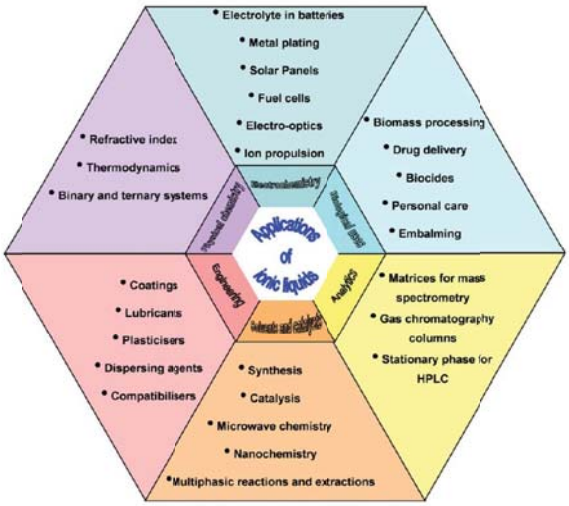

Figure 1.1 Applications of ILs in various fields of science and engineering[2]

The absence of volatility is one important property of ILs. Many ILs have low combustibility, excellent thermal stability, wide liquid regions, and favorable solvating properties for a range of polar and non-polar compounds, making ILs promising for a number of applications. ILs have uses as 'green' solvents for chemical synthesis, catalysis and separations and as electrolytes for electrochemistry and photovoltaics, among other applications. In Figure 1.1 several possible applications of ILs in different fields are summarized. The most successful application of ILs in an industrial technology is the BASIL (Biphasic Acid Scavenging utilizing ILs) process, which was introduced by the BASF site in Ludwigshafen, Germany, in 2002. They

replaced triethylamine by 1-methylimidazole, resulting in the formation of an IL(1-methylimidazolium chloride). The ILs can be separated out of the reaction mixture as a discrete phase and recycled.[3]

Several disadvantages have been encountered in possible applications of ILs in industrial settings. According to Walden's rule[4], the conductivity of an electrolyte correlates with its viscosity. High viscosity of ILs can lead to lower conductivity, poor mass transfer and mixing processes of ILs, which can limit their industrial applications. It is hard to get pure ILs because the preparation methods still need improvements. Another disadvantage is that most of the ILs are moisture/air sensitive. Hygroscopic ILs such as imidazolium-based cations can absorb significant amount of water vapor from air, which can change their chemical and physical properties such as reaction rates, selectivity, media polarity, viscosity, conductivity and solvation properties. Some reactions involving ILs have to be performed under vacuum, which limit their applications. Another disadvantage is that most ILs have high associated costs. Commercial uses of ILs at large scale are still limited.

1.2 ILs in electrochemistry

The performance of different electrochemical energy storage and conversion devices is compared in Figure 1.2. Batteries and fuel cells are typical low power devices (*i.e.*, they can store significant amounts of energy but can't deliver it very quickly). EDLCs, or supercapacitors, have larger energy densities than traditional capacitors, and their larger power density can be used to complement battery performance. EDLCs exhibit faster charge/discharge times, thus enabling energy recovery at much higher rates as well[5-6]. They also have higher cycle life and wider temperature operation range comparing with batteries[7-9]. ILs have been proposed as potential electrolytes for energy storage in EDLCs and DSSCs for conversion of solar energy and

lithium batteries. Traditional organic solvents have potential safety drawbacks related to their flammable and volatile nature, which can result in explosions or fire accidents. ILs exhibit high electrical conductivity, wide electrochemical stability window of up to 6.0 V, low volatility, and high chemical and thermal stability compared to 'conventional' electrolytes (*i,e*., aqueous or organic solution of 'small' ions)[10-14]. Their main drawback is their relatively high viscosity.

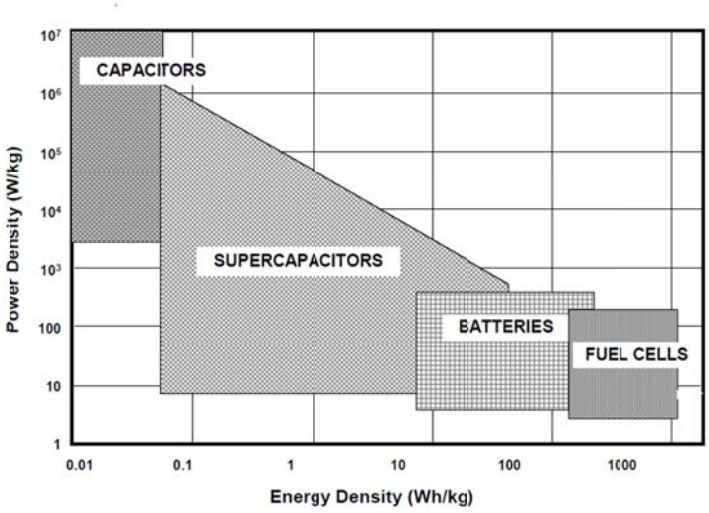

Figure 1.2 Sketch of Ragone plot for various energy storage and conversion devices. The indicated areas are rough guide lines.[15]

For a symmetrical capacitor the cell capacitance (C_{total}) can be obtained by

$$\frac{1}{C_{total}} = \frac{1}{C_{dl,+}} + \frac{1}{C_{dl,-}} \tag{1.1}$$

$$C_{dl} = \frac{\varepsilon A}{t} \tag{1.2}$$

The performance of EDLCs can be characterized by their energy and maximum power:

$$W = \frac{1}{2} C_{dl} V^2 \tag{1.3}$$

$$P = \frac{V^2}{4R} \tag{1.4}$$

C_{dl}, $C_{dl,+}$ and $C_{dl,-}$ represent the capacitance of the any electrode, positive electrode and negative electrode, respectively; ε is the dielectric constant of the electrical double-layer region; A is the surface-area of the electrode; t is the thickness of the electrical double layer; W is the energy stored in EDLCs; P is the power; V is the voltage; and R is the equivalent series resistance. Usually the energy and power densities are obtained by normalizing the energy and power (divided by the weight or volume of the device or the electrode)

The performance of EDLCs can be improved by increasing the capacitance which is controlled by the electrode/electrolyte interface (C_{dl} in Eqn. 1.3) or the cell voltage (V in Eqn. 1.3) which is mainly limited by the electrolyte interface. From Eqn. 1.2, we can see that in order to improve the capacitance of EDLCs we should use the electrode material with high surface-area (typically >1500 m^2g^{-1}) and extremely small charge separation layers (Angstroms). The EDLCs cell voltage is limited by the electrolyte decomposition at high potentials. Replacing aqueous electrolyte by organic electrolytes can greatly increase the cell voltage from 0.9 V to 2.5-2.7 V. In the applications, it also requires the electrolyte to have high conductivity, good corrosion resistance and high temperature stability. The electrodes should have controlled pore structure, processability and compatibility in composite materials and relatively low cost. In summary, to maximize the charge stored per unit of weight or volume of carbon, we need to optimize the adsorption of ions from the electrolyte by designing the electrode-electrolyte interface.

Conventional electrolytes are a mixture of a solvent and a salt (typically an alkylammonium salt dissolved in acetonitrile). The use of acetonitrile (AN) as solvent can increase the conductivity and ion transport of the electrolyte but the high volatility, flammability and toxicity properties raise safety and environment concerns. The mixture also has low flash point (10 °C) and emits toxic CN^- and NO_x as combustion products, which limit its applications.

ILs can be alternative electrolyte for energy storage in EDLCs and DSSCs. Experiments show that EDLCs with ILs as electrolyte can operate at higher voltages, boosting their specific energy and specific power. Another advantage is the use of ILs can open up the possibility of utilizing EDLCs at higher temperature[16], such as military devices, hand-held surgical tools for sterile surgical environments, subterranean probes and other power systems. The high viscosity of ILs can lead to slow ion transport and high internal resistance, which has limited their widespread applications. Several approaches have been undertaken to decrease the viscosity and improve their ionic conductivity. For example, mixing the ILs with various organic solvents such as propylene carbonate (PC), diethyl carbonate (EC), dimethyl carbonate (DMC), diethyl carbonate (DEC) or ethyl methyl carbonate (EMC)[17-20].

The storage density can be improved through using nanoporous materials such as slit-like, cylindrical and activated charcoal, in place of the conventional insulating barrier. The material used in EDLCs is mainly carbon since it offers a combination of electrical conductivity, high specific surface area and electrochemical stability over a wide range of potentials in both aqueous and non-aqueous electrolytes. Graphene, carbon nanotubes, carbon polymers, carbon aerogel and solid activated carbon are mainly used in the EDLCs. In Figure 1.3, we show a scheme of an EDLC in its charged state; the positive charged surface adsorbs the anions and the negative charged surface adsorbs cations. Because the size of the nanopore is much smaller than the thickness of the diffuse layer there is an overlapping of the two electrical double layers. Experimental and theoretical investigations show that the storage capacity of EDLCs can increase of up to 50% through controlling the nanostructure of porous carbons.[8, 21-22] The macroscopic performance of IL-based EDLCs and DSSCs is governed by the properties of the electrical double layer at the electrolyte-nanoporous electrode interface, which in turn are

determined by the structural and dynamical properties of electrolyte confined in the nanopores materials.

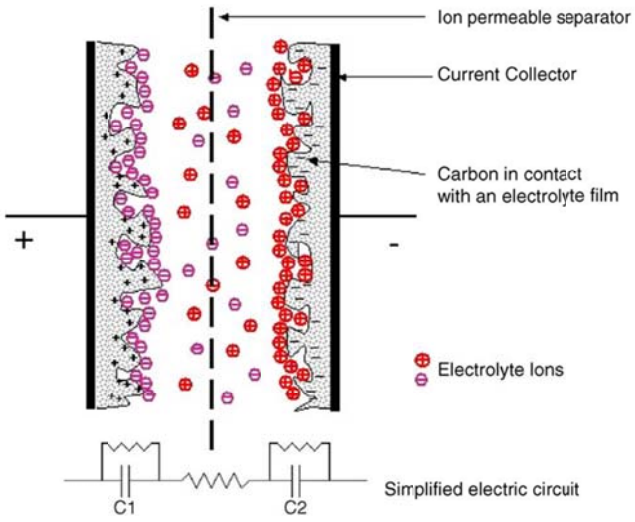

Figure 1.3 Representation of an electrochemical double layer capacitor (in its charged state)[21].

1.3 ILs confined in different morphologies

In IL-based EDLCs, the ILs are in contact with nanoporous electrodes, and therefore the morphology of the pores play an important role in the structural and dynamics of the confined ILs. An increased interaction between the IL and pore surface in the EDLCs can promote higher energy densities. Different nanoporous materials have been considered such as slit-like[23-28], carbon nanotubes[29-34], the onion-like carbon[35-38], carbide derived carbon (CDC)[39-40] and ordered mesoporous carbon (OMC)[41] (Table 1.1). Their large volumes of internal micropores and mesopores can result in high surface area, compared to small external surface area. The ILs are essentially confined within the carbon particles. Compared to the bulk IL, confinement plays an important effect on the density, viscosity and diffusion of the ILs. Furthermore, the properties of

confined ILs also depend on the morphology of nanomaterials such as pore structure, pore size and surface functional groups.

Table 1.1[22]: Different Carbon Structures Used in EDLCs with Onion-like Carbon (OLC), Carbon Nanotubes, Graphene, Activated Carbons, and Carbide-Derived Carbons

Material	Carbon onions	Carbon nanotubes	Graphene	Activated carbon	Carbide derived carbon	Templated carbon
Dimensionality	0-D	1-D	2-D	3-D	3-D	3-D
Conductivity	High	High	High	Low	Moderate	Low
Volumetric Capacitance	Low	Low	Moderate	High	High	Low
Cost	High	High	Moderate	Low	Moderate	High
Structure		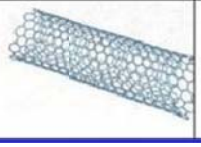	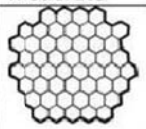	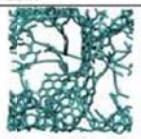	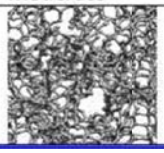	

In order to increase the capacitance of the energy storage devices, the combination of the right electrode with a proper electrolyte is required. Graphene electrode has higher charge-discharge rates compared to activated carbon, but graphene doesn't have higher volumetric capacitance than porous carbons. The exohedral nanoparticles such as carbon nanotubes and onion-like carbon can provide high power due to fast ion sorption-desorption on their outer surface. However, the production of highly homogenous carbon nanotubes or the purification of them according to their length, diameter and chirality is a big obstacle towards practical applications. Activated carbons have a three-dimensional porous network with micropores (pore size <2 nm) and mesopores (2-50 nm). Because their scalable manufacturing, reasonable cost and high capacitance, activated carbons are widely used in commercial devices. Carbide-Derived Carbons (CDCs) have high specific surface areas (1000-3000 m^2/g) with a controlled narrow pore size distribution, which make them attractive candidates as electrode in supercapacitor applications[42]. These materials have shown impressive specific capacitance when used as the

active material in supercapacitors with many electrolyte systems[42-44]. Templated carbons are produced by the carbonization an organic compound in nanospace of a template inorganic substance and then liberation of the carbon from the template. Therefore, the template technique allows precise control of the size and structure of carbon. Other carbons can be also used in supercapacitors such as carbon nanohorns[44] and aerogels; however the former are presently used for research purposes, whereas the later are limited to support pseudocapative materials.

1.4 ILs-based nanomaterials

Traditionally most of research regarding ILs has been focused on those whose melting temperatures are below room temperature, mainly because of their uses as solvents in reactions, material synthesis and separation process. In recent work, nanoparticles were synthesized from different organic salts that are in solid phase (frozen ILs) at room temperature by Dr. Warner's group (Chemistry, LSU) [45-49]. The melting temperature of these ILs is above room temperature. These organic salts were termed 'Group of Uniform Materials Based on Organic Salts (GUMBOS)[45-49]. The simplicity of the synthesis procedure, when combined with the versatility of the high-tunable properties of the ILs[1-2], suggest potential applications of these materials in fields as diverse as biomedical applications, analytical chemistry, optoelectronics, photovoltaics and separations. For example, in magnetic hyperthermia cancer treatment, magnetic nanoparticles are delivered to cancerous tumors, and heated using resonating magnetic fields to destroy cancer cells. Fluorescent, magnetic and gold-coated nanoparticles can be used to label tissues and cells in medical imaging. The magnetic and optical properties can be tuned by introducing shape anisotropy[50-58]. Furthermore, ionogels, a new class of hybrid materials[59-63], involve a solid-like network formed by immobilizing ILs within nanoporous solids (e.g., CNTs,

porous silicas, organic gelators, polyethyleneoxide, cellulose, etc.). Ionogels have potential applications as solid electrolyte membranes in lithium batteries, fuel cells and DSSCs[63].

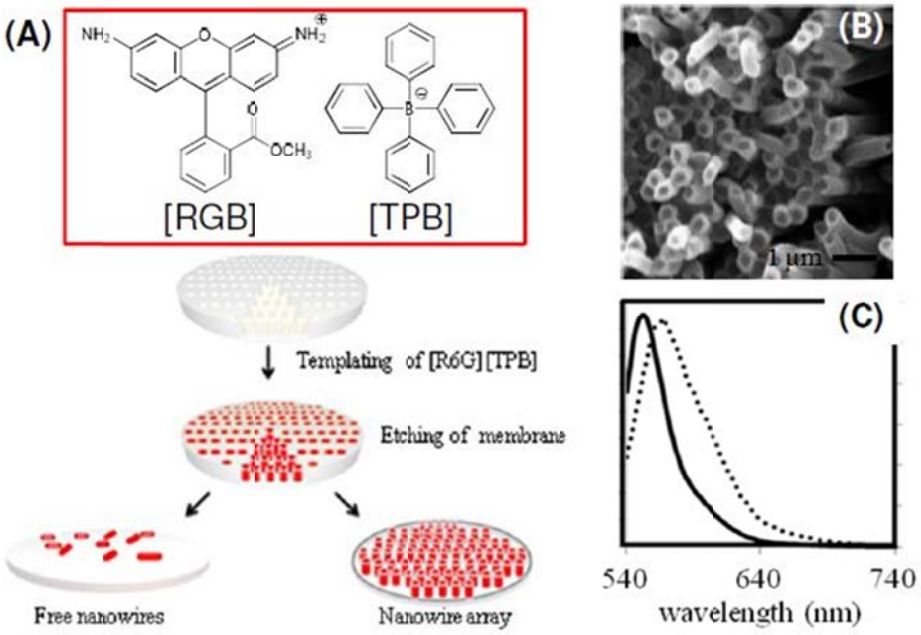

Figure 1.4 (A) Synthesis of 1D rhodamine 6G tetraphenylborate ([R6G][TPB]) nanoGUMBOS. AAM is wetted with a [R6G][TPB]-acetone solution, solvent is later evaporated. An alternative route involves putting solid GUMBOS on top of the AAM disc, and then heat to melt the GUMBOS. The template is then removed using a phosphoric acid solution. The resulting 1DnanoGUMBOS are rinsed and dried. (B) SEM micrograph of [R6G] [TPB] nanotube array. (C) Fluorescence spectra of [R6G][TPB] solution in ethanol (solid line) and nanowires (dotted line).[64]

Solidification of ILs inside templating nanoporous materials is one important step in the synthesis of some nano-GUMBOS. The ILs-based nano-GUMBOS were initially synthesized without using any hard template[48]. Nevertheless, in order to tune the magnetic and optical properties of the nano-GUMBOS, 1D-nano-materials[64] (*e.g.*, nano-rods, nano-tubes and nano-wires) based ILs were also prepared, by confining these organic salts inside hard templates with cylindrical nano-pores, *e.g.*, multi-walled carbon nanotubes, anodic alumina membrane and templated mesoporous silica. Figure 1.4 shows the synthesis of fluorescent organic salt through

anion exchange and the subsequent fabrication of 1D-nanostructure via a facile templating method. The 1D-nanoGUMBOS has the diameters between 20 to 500 nm and length of 1 to 20 μm.

1.5 Nucleation theory

In order to rationally design the IL-based nanomaterials describe in Section 1.4, we need a fundamental understanding of solidification of ILs inside nanopores. Solidification occurs by two processes, nucleation and growth. In the nucleation process, the molecules start to organize into a nucleus. The nucleus is not stable and can dissolve until it reaches the critical nucleus size. The crystal growth is the subsequent growth of nuclei that succeed in achieving the critical cluster size. Because nucleation is one important step in the solidification process, several theories of nucleation are shown in this section.

There are mainly two types of nucleation. Nucleation without preferential nucleation sites is homogeneous nucleation, which occurs spontaneously and randomly under supercooling of the medium. Compared to the homogenous nucleation, heterogeneous nucleation normally occurs on surfaces contacting the liquid or vapor. The nucleation sites are provided by suspended particles or minute bubbles. Homogeneous nucleation occurs with much more difficulty in the interior of a uniform substance than heterogeneous nucleation. For example, pure water freezes below -30 °C rather than at its freezing temperature of 0 °C[65]. The crystallization of liquid water can be facilitated by adding some nucleation "seeds" such as small ice particles or simply shaking.

1.5.1 Homogeneous nucleation

Though homogeneous nucleation is much rarer than heterogeneous nucleation, homogeneous nucleation is simpler and easier to understand. Classical Nucleation Theory (CNT)

is the most common theoretical model that can describe experimental data. In CNT, the change of free energy (Gibbs if this is at constant pressure) can be calculated through the following equation[66-67]:

$$\Delta G(r) = \frac{4\pi}{3} r^3 \left(\frac{\mu_s^0 - \mu_1^0}{V_M} \right) + 4\pi r^2 \sigma \qquad (1.5)$$

r: the radius of the particle

V_M: molar volume of the solid

μ_s^0: chemical potential of the solid phase corresponding to a flat surface

μ_{sl}^0: chemical potential of the liquid phase

σ: surface tension of the interface between the nucleus and its surroundings

In Figure 1.5, the free energy change is plotted as a function of particle radius. The free energy change $\Delta G(r)$ can be balanced by two 'competitive' factors: the volume free energy (the first term in the above equation) and the interfacial energy due to formation of solid (the second term in the above equation). The nucleation can be understood in 3 thermodynamic regimes: 1) nucleation from the free molecules or atoms to form a small nucleus. This is caused by the difference between the Gibbs free energy of liquid and solid (also called 'driving force' for the phase transformation). As the particles grow, $\Delta G(r)$ increases (mainly driven by the rapid increase in interfacial energy), implying that the particle growth or the continuous nucleation in this regime is not thermodynamically favorable. In this regime, most of the particles dissolve back to liquid phase. 2) Once some of the particles reach the critical nucleus size r^* and pass the barrier of ΔG^*, further growth of particles will lead to decrease in $\Delta G(r)$, a tendency favorable for the continuous crystallization, although $\Delta G(r)$ in this regime before reaching the critical nucleus size is still not thermodynamically favorable. The contribution of interfacial energy results in a kinetic barrier for the nucleation. 3) After passing r^*, $\Delta G(r)$ will become more

negative and the growth of nucleus will be highly favored and eventually lead to formation of bulk phase solid.

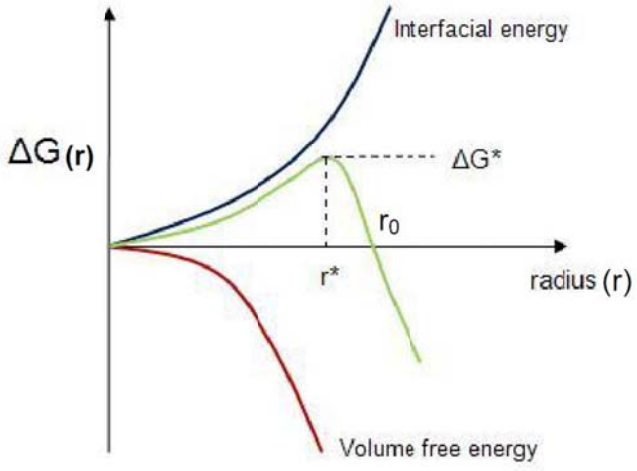

Figure 1.5 the total free energy change (green curve), the volume free energy (red curve) and interfacial energy (black curve) as a function of particle radius. ΔG^* is the free energy barrier and r^* is the critical nucleus size.[66]

The critical nucleus size can be calculated as follows[67]:

$$r^* = -\frac{2\sigma}{\Delta g} \tag{1.6}$$

$$\Delta g = \frac{\mu_s^0 - \mu_1^0}{V_M} = \frac{\Delta h(T_m - T)}{T_m} \tag{1.7}$$

Δg is the difference between free energies per unit volume of solid and liquid (driving force for nucleation, proportional to the undercooling comparing with the melting temperature).

The barrier of nucleation is[67]

$$\Delta G^* = \frac{16\pi\sigma^3}{3(\Delta g)^2} \tag{1.8}$$

The rate of nucleation can be predicted by[67]

$$R = N_S Z j exp\left(\frac{-\Delta G^*}{k_B T}\right) \tag{1.9}$$

Where

T is the absolute temperature and K_B is the Boltzmann constant

N_S is the number of nucleation sites

j is the rate at which molecules attach to the nucleus causing it to grow, which depends on the diffusion coefficient.

Z is the probability that a nucleus at the top of barrier will go to form the new phase, not dissolve, which is also called Zeldovich factor.

The nucleation rate depends on the temperature. When the temperature is a little below the melting point, the nucleation rate is suppressed because ΔG* is too high. Continue decreasing of the temperature can cause increasing of the nucleation rate because ΔG* decreases. The nucleation typically happens in this temperature range. But when the temperature is too low, the nucleation rate decreases due to the drop in the mobility of molecules.

CNT is based on the continuums thermodynamics treatment of clusters by imposing the capillary approximation, which means that small clusters are considered to have the same properties as the bulk. Therefore, using CNT requires a large representative ensemble and a well-defined surface. If the critical nucleus contains a few tens of molecules, the validity of the continuum thermodynamics is doubtful. There are the other theories to study the nucleation beyond CNT, such as Dillmann-Meier theory[68-70], density function theory and kinetic nucleation theory[71-72].

1.5.2 Heterogeneous nucleation

Understanding the heterogeneous nucleation is also very important since it occurs more often than homogeneous nucleation. Heterogeneous nucleation is typically much faster than homogenous nucleation. The extent of how a surface can facilitate the nucleation depends on the

contact angle of the nucleus with respect to the substrate. As the contact angle decreases, the free energy barrier decreases and hence results in faster nucleation. The critical nucleus size for a heterogeneous nucleation is usually the same as that for a homogeneous nucleation.

Freezing inside porous materials is naturally related to heterogeneous nucleation. Pore size, pore morphologies as well as nature of fluid-wall interaction have significant effect to the freezing in confinement[73]. There have been experimental reports that investigated the structure of the confined phases through NMR and x-ray diffraction techniques. Overloop and Gervan[74] studied the freezing of water in porous silica by NMR, finding that the first three molecular layers adjacent to the pore wall have a structure that is different from the crystal phase and from that of the free liquid. Morishige and co-workers[75-76] confirmed the existence of a disordered layer near the pore wall using x-ray diffraction for the water in siliceous MCM-41. Sliwinska-Bartkowiak et al[77] studied the melting/freezing transition for nitrobenzene confined in CPG of different pore size. They confirmed the existence of a contact layer with dynamics properties that were more liquid like than the inner layers.

The change of freezing temperature can be caused by the confinement. According to previous studies, if the fluid-wall interaction is weak relative to the fluid-fluid interaction, the confinement can cause a decrease in the melting/freezing temperature. On the contrary, the strong attraction between the confine fluid molecules and surface can result in an increase in the freezing temperature. Iiyama *et al*[78-79] indicated an increase in the freezing temperature due to confinement by X-ray diffraction studies of water in activated carbons. The experimental study of cyclohexane and octamethylcyclotetrasiloxane (OCTMS)[80] between parallel mica surfaces also provided evidence of an increase in freezing temperature in confined systems. Similarly, an increase of the freezing temperature has been reported for benzene in activated carbon[81].

However, Booth and Strange[82] found the melting of cyclohexane in porous silica was below the bulk melting point. Recently, Lupi *et al*[83] investigated the nucleation of ice on carbon surfaces and found that the flat graphitic surfaces can promote the heterogeneous nucleation of ice, while molecularly rough surfaces with the same hydrophobicity do not.

1.6 Classical molecular simulation methods

There has been intense interest in understanding the basic physical and chemical properties of ILs from molecular level. In particular, more and more researchers are using classical molecular simulation methods to complement experiments observations of ILs. Currently computer simulations can successfully predict the physical properties of ILs such as density, viscosity, electrochemical window, diffusion ability and capacitance in EDLCs. It requires a combination of several theoretical approaches in order to accurately predict its properties.

Monte Carlo (MC) simulations rely on statistical mechanics, but have not been extensively used to study systems of ILs. In contrast, MD simulation has been the popular choice when modeling ILs, mainly because of the existence of a number of widely available codes (Gromacs, NAMD, LAMMPS, etc.) that can be immediately used to study ILs. Another reason is that MD simulation can used to study the time dependent properties such as diffusion coefficient, relaxation time and rheological properties and thermodynamical properties of the system. Besides, MD simulation can model the "real" dynamics of a collection of atoms, molecular, particles, or other extended objects, which is one of the most commonly used methods for material simulations. It involves a numerical step by step solution of Newton's equation of motion under the influence of a force field. Through integrating numerically Newton's equations of motion the time dependent positions and velocities of each atom can be obtained, yielding a

trajectory. From the trajectory, the average value of properties can be determined. Therefore, once the position and velocity of each atom are known, the state of the system at any time in the future or the past can be predicted. Nowadays, most of the molecular simulations are in the nanosecond scale although time scales on the order of milliseconds have been reported. Molecular dynamics simulation is computationally expensive, but as high computational technology improves computation is becoming faster and cheaper.

In the MD simulation, we need to use appropriate force field (FF). Regarding the FFs for the ILs, there are three groups of options. One option is the non-polarizable FF of Lopes *et al*[84-88]., which includes parameters for a large number of cations and anions , and it has been validated against several experimental properties (volumetric behavior such as liquid density, crystalline structure) of the ILs. However, this FF has some shortcomings in reproducing some experimental properties (related to energetic characteristics such as heats of vaporization, diffusivities, viscosities and ionic conductivities) of the ILs. Another option is to use other non-polarizable FFs[89-95], in particular some that have been developed for several specific ILs, and thus can give good results for their densities, heat of vaporizations and transport properties. The main shortcoming of this second option is that most of the parameters of these FFs are IL-specific and might not be transferable to other ILs. A third option is to use the APPLE&P polarizable FF[96-99]. Recently[97-104] it has been argued that polarizability effects need to be included in force fields for them to be transferable to different ILs and to give accurate predictions of densities, heats of vaporization, dynamical properties and crystalline structure. The APPLE&P polarizable FF is applicable to a wide range of ILs. However, polarizable models are more complex and computationally more expensive, and therefore face important limitations in the system sizes and time scales that can be studied. In this study, only the first two types of FFs

are considered. The interactions between the ILs and the carbon atoms in the carbonaceous model materials will be modeled *via* Lennard-Jones interactions.

Simulations with these model materials allow us to elucidate the effect of (1) the interactions between the pore walls and the ILs, and (2) pore size, shape and surface roughness, on the molecular-level properties of the ILs.

1.7 Scope of this dissertation

This dissertation seeks to apply classical MD simulations to understand the structure, dynamics and crystallization of ILs. The organization of this dissertation is as follows: the second chapter describe the structure and dynamics of ILs 1-ethyl-3-methylimidazolium bis(trifuluoromethanesulfonyl)imide [$EMIM^+$][NTf_2^-], 1,3-dimethylimidazolium chloride [$dmim^+$][Cl^-] confined inside the ordered mesoporous carbon CMK-3 and CMK-5. In the third chapter, we investigated the homogeneous nucleation of crystals of the IL [$dmim^+$][Cl^-] from its supercooled liquid. In the fourth chapter, MD simulations similar to those described in chapter 3 were performed for the same IL but with a larger system size, in order to discuss finite-size effects. In chapter 5, the heterogeneous nucleation of IL [$dmim^+$][Cl^-] near a graphene disk was investigated and compared with homogeneous nucleation for the same IL [$dmim^+$][Cl^-]. Finally, Chapter 6 summarizes the results obtained from these projects.

Chapter 2 Molecular Modeling of Ionic Liquids in the Ordered Mesoporous Carbon CMK-5*

2.1 Introduction

Understanding the properties of ionic liquids (ILs) inside nanopores have attracted a lot of attention in the last few years, mostly because of the relevance of ILs as electrolytes in energy-related devices such as electrochemical double layer capacitors (EDLCs)[8, 105-113] and dye-sensitized solar cells (DSSCs).[114-119] Molecular simulations can contribute towards achieving a fundamental understanding of the properties of ILs inside nanoporous materials and complement experimental work in this area. A few recent review papers[120-123] (as well as references therein) provide an excellent overview of the progress in this field of research, which has literally exploded over the last few years. Most of the studies reviewed in these papers focused on electrified (charged) nanoporous electrodes, which is not surprising considering the relevance of these systems as electrolytes in energy storage devices. Nevertheless, a fundamental understanding of the properties of ILs inside *uncharged* nanoporous materials is particularly relevant to the development of novel nanomaterials based on ILs. For example, inserting ILs inside templating nanoporous materials (e.g., carbon nanotubes, templated mesoporous silicas, anodic alumina membranes) is one step in the synthesis of optically-active (fluorescent) and magnetic nanomaterials based on ILs.[46-47, 49, 64, 124-126] These nanomaterials (dubbed 'GUMBOS', for Group of Uniform Materials Based on Organic Salts) have the highly tunable properties of ILs and can be prepared *via* simple procedures, and thus have potential applications in optoelectronics, photovoltaics, separations, analytical chemistry and biomedicine. Furthermore,

* Contents of this chapter were published in the following article: He, X.; Monk, J.; Singh, R.; Hung, F. R. Molecular modeling of ionic liquids in the ordered mesoporous carbon CMK-5. *Molecular Simulation* **2015**. http://dx.doi.org/10.1080/08927022.2015.1089992

ILs confined inside sol-gels (ionogels) have potential applications as electrolyte membranes and in optics, catalysis and biocatalysis, drug delivery and sensing and biosensing.[63, 127-128]

Here we report classical molecular dynamics simulations of two ILs, [emim$^+$][NTf$_2^-$] and [dmim$^+$][Cl$^-$] (Figure 2.1), inside an uncharged model of the ordered mesoporous carbon CMK-5.[129-130] This material consists of hexagonally-packed nanopipes made of amorphous carbon, and thus the ILs can adsorb inside and outside the amorphous carbon nanopipes (ACNPs) (see Figure 2.3d). The ACNPs in CMK-5 have uniform diameters and exhibit thin carbon walls with corrugations and curvature, and thus the nanopores in CMK-5 are interconnected in a regular way. We compare our results to simulations of the same ILs in another ordered mesoporous carbon, CMK-3,[129, 131] of similar pore sizes. This material is very similar to CMK-5, but is made of hexagonally-packed amorphous carbon nanorods (ACNRs, see Figure 2.3b). Because of their uniform structure, the ordered mesoporous carbons CMK-3 and CMK-5 are well suited for fundamental studies aimed at understanding the effects of variables such as pore size, pore geometry, surface roughness and pore interconnectivity on the properties of confined ILs. In addition, the ordered mesoporous carbons CMK-3 and CMK-5 have been used as electrodes in EDLCs in previous experimental studies.[132-138] We also studied the properties of the same ILs inside an isolated ACNP (i.e., no IL adsorbed on the outer surface of the ACNP, see Figure 2.2d). We found significant differences in the densities and mobilities of ions in CMK-3, CMK-5 and in an isolated ACNP. Overall, our results indicate that the presence of IL in the *outer* surface of an uncharged carbon nanopipe can affect the dynamics and the density of an IL adsorbed *inside* the carbon nanopipe, and vice versa. The remainder of the paper is structured as follows. Section 2.2 introduces the computational methods used in these simulations. In section 2.3 we present

and discuss the structure and dynamics of the ILs inside our model materials, and in section 2.4 we summarize and discuss our findings.

2.2 Methods

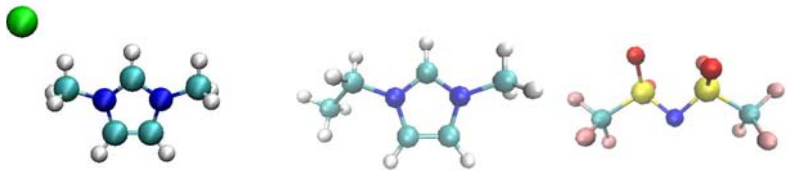

1,3-dimethylimidazolium chloride, [dmim$^+$][Cl$^-$]

1-ethyl-3-methylimidazolium bis(trifluoromethylsulfonyl)imide, [emim$^+$][NTf$_2^-$]

Figure 2.1 Scheme of the ILs considered in this study. Dark blue = N; light blue = C; white = H; green = Cl; yellow = S; red = O; pink = F.

We performed classical MD simulations of the ILs [dmim$^+$][Cl$^-$] and [emim$^+$][NTf$_2^-$] (Figure 2.1) confined inside a single amorphous carbon nanopipe (ACNP), and inside the model ordered mesoporous carbons CMK-3 and CMK-5. No electrical charges were present in any of our model carbon materials. We used the GROMACS 4.5.4 MD package[139] for our calculations. The IL [emim$^+$][NTf$_2^-$] was modeled using the force field (FF) of Kodderman *et al.*,[94] which can adequately reproduce experimental values of relevant physical properties such as density, heat of vaporization, shear viscosities, self-diffusion coefficients and NMR rotational correlation times.[94] For example, the bulk density of [emim$^+$[[NTf$_2^-$] is 1.477 g/cm^3 at 333 K, which is less than a 1% difference from the experimental density (1.4858 g/cm^3) at the same temperature.[140] The IL [dmim$^+$][Cl$^-$] was modeled using the FF of Lopes *et al.*[84, 87] Although this FF has well-known shortcomings in reproducing experimental values of properties such as heats of vaporization, diffusivities, viscosities and ionic conductivities,[98, 141-143] we decided to use this FF nevertheless because we used it in our previous study of [dmim$^+$][Cl$^-$] inside CMK-3 model materials.[41] Moreover, in that previous study we determined that the FF of Lopes *et al.* was able

to give reasonable values for most experimental properties of interest for this particular IL. For example, we calculated the self-diffusivity of [$dmim^+$][Cl^-] in the bulk and found values that were in good agreement with results from previous simulation studies.[143-144] Furthermore, the simulated density of [$dmim^+$][Cl^-] is 1.132 g/cm^3 at 425 K, which is less than a 1% difference from the experimental density (1.1254 g/cm^3) found by Fannin *et al*.[145]

The ACNP used to build the model CMK-5, as well as the amorphous carbon nanorod (ACNR) used in the model CMK-3 material considered here, was developed by Jain and co-workers.[146] The carbon nanorod and nanopipe were created using grand canonical Monte Carlo (GCMC) simulations to model the adsorption of carbon atoms into a cylindrical silica pore mimicking a SBA-15 material.[147-149] In these simulations, the interactions between the carbon atoms were modeled using the empirical REBO potential,[150] and the carbon-silica interactions were accounted for using the PN-TrAZ potential.[151] If the silica nanopore is completely filled with carbon, the simulation protocol yields an ACNR with a diameter of 2.8 nm and a length of 10.69 nm, which is then used to prepare the model CMK-3 materials used here and in our previous study.[41] If the silica pore is only partially filled with carbon,[146] the procedure yields an ACNP that exhibits inner and outer surfaces with roughness at atomic scales (Figure 2.2). The ACNP has an average external diameter of 2.8 nm, a length of 10.69 nm, and a varying inner diameter, as can be observed in the three cross-sections of this ACNP shown in Figure 2.2. The internal pore size distribution (PSD) of the ACNP was determined following procedures described in previous studies.[152-155] The PSD shown in Figure 2.2c indicates that the internal diameter of the ACNPs has an average value of approximately D = 1.5 nm and can reach values of up to 1.8 nm. The average wall thickness of the ACNP is equal to 0.45 nm. We estimated that the total accessible volume inside the ACNP is ~19 nm^3. This value was determined by dividing

the axial length of the ACNP (10.69 nm) into 40 slices of length z_Δ. After that, we determined the average pore diameter D_Δ for each slice, approximated the volume of each slice as a cylinder of $V_\Delta = \pi D_\Delta^2 z_\Delta / 4$, and added the volumes of the 40 slices. The ACNP was replicated and arranged into a periodic hexagonal pattern to form the model CMK-5 materials used here; similarly, replicas of the ACNR were arranged into a periodic hexagonal array to build our model CMK-3 materials.

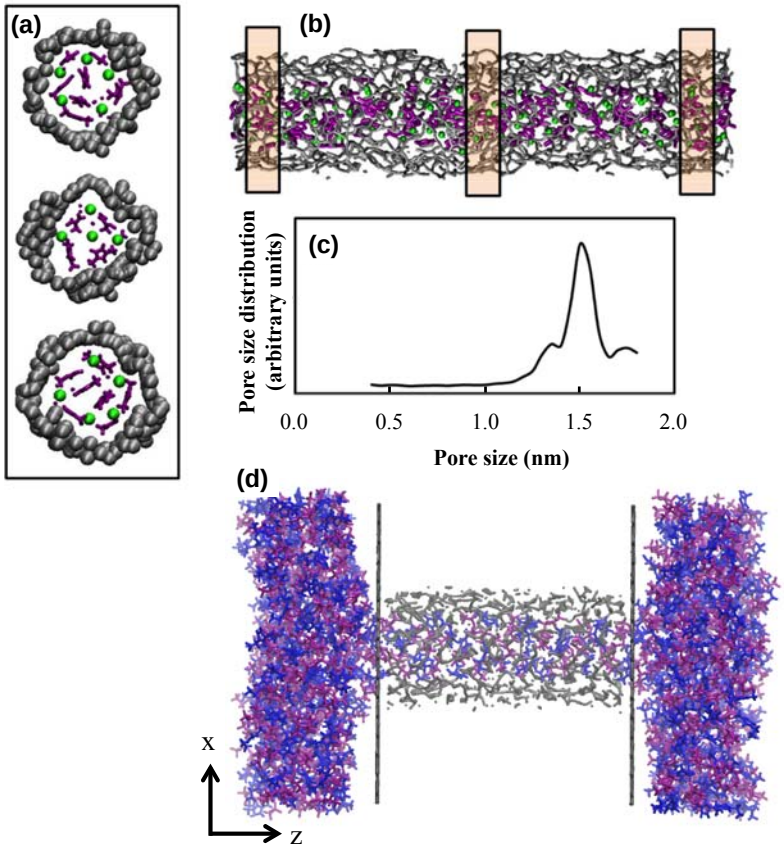

Figure 2.2 (a) Three cross-sections of amorphous carbon nanopipe (ACNP) filled with [dmim$^+$][Cl$^-$], showing the non-uniform inner diameter. Here cations and anions are colored purple and green. (b) Side view of an ACNP filled with [dmim$^+$][Cl$^-$]; the rectangles represent the location of the cross sections shown in (a). The total length of the ACNP here is 10.69 nm. (c) Internal pore size distribution (PSD) of the ACNP, showing its internal diameter. (d) Representative simulation snapshot of [emim$^+$][NTf$_2^-$] inside an isolated ACNP. Here, cations and anions are depicted in blue and purple; the total length of the ACNP is 5.5 nm; and the vertical grey lines represent carbon walls, which do not allow the IL to adsorb on the outer surface of the ACNP (the IL can only adsorb inside the ACNP).

Figure 2.3 shows the CMK-3 and CMK-5 model materials with a pore size H = 2.5 nm filled with the IL [emim$^+$][NTf$_2^-$]. CMK-5 model materials with a pore size H = 1.8 nm were considered for our simulations with the IL [dmim$^+$][Cl$^-$], in order to make direct comparisons with our previous study[41] for the same IL inside a model CMK-3 material of similar characteristics. The pore size of our CMK-3 and CMK-5 models was defined as the distance between the centers of two nearest amorphous carbon nanorods/nanopipes, minus their outer diameter (2.8 nm), and minus the Lennard-Jones size parameter of a carbon atom (0.34 nm). The typical setup we used here for our simulations is the same used in our recent study of ILs inside a coconut shell activated carbon model,[156] where our model porous carbons were placed in the center of an orthorhombic simulation box elongated in the z direction, in such a way that the model carbon materials are directly connected to two reservoirs of IL at both sides in the z direction (Figure 2.3), and the x and y dimensions of the orthorhombic simulation box matched the x and y dimensions of the materials. Periodic boundary conditions were applied in all three directions, and therefore the ILs confined in the model CMK-3 and CMK-5 materials were periodic in the x and y directions. A representative simulation box for our systems with [emim$^+$][NTf$_2^-$] and CMK-5 had dimensions L_x = 7.98 nm, L_y = 9.21 nm and L_z = 40.0 nm; a smaller simulation box (L_x = 7.98 nm, L_y = 4.61 nm and L_z = 40.0 nm) yielded satisfactory results for the same IL within CMK-3 materials. In both cases the pore size of our materials was H = 2.5 nm. In our simulations with [dmim$^+$][Cl$^-$] and CMK-5, our model material had a pore size H = 1.8 nm, and the length of our ACNRs and ACNPs was 10.69 nm; for our simulations with [emim$^+$][NTf$_2^-$], we used ACNRs and ACNPs with shorter lengths (5.5 nm) to reduce computational costs. For our simulations with a single ACNP, we used a simulation box of dimensions L_x = 5.0 nm, L_y = 5.0 nm, and L_z = 40.0 nm. The ACNP was placed in the center of

this simulation box, and was directly connected to two reservoirs of IL at both sides in the *z* direction; therefore the ACNP was surrounded by a big vacuum region in the radial direction (Figure 2.2d), which was large enough to avoid any interactions between the adsorbed ions and their nearest periodic image in the *x* and *y* directions.

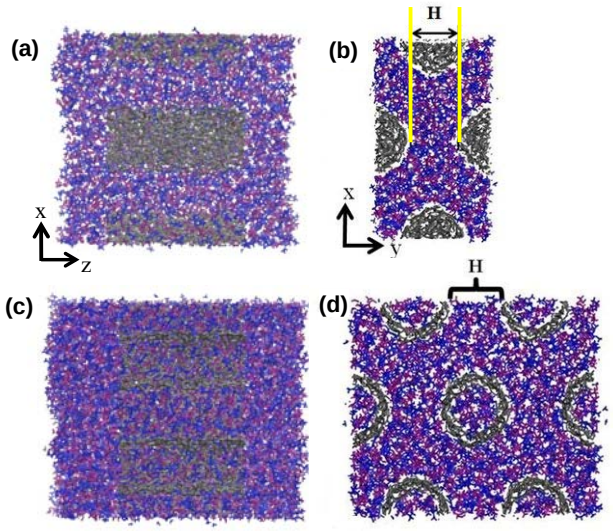

Figure 2.3 Representative simulation snapshots of [emim$^+$][NTf$_2^-$] inside a model CMK-3 material (a, b), and inside a model CMK-5 material (c, d) with a pore size H =2.5 nm. The cations and anions are depicted in blue and purple; carbon atoms are represented in dark grey.

MD simulations in the canonical ensemble at 333 K were conducted for [emim$^+$][NTf$_2^-$] inside a single ACNP and inside model CMK-3 and CMK-5 materials. Likewise, simulations at 425 K were performed for [dmim$^+$][Cl$^-$] inside a single ACNP and inside a model CMK-5 material; these results were compared with those obtained from our previous study of the same IL inside a model CMK-3 material.[41] The carbon atoms in our model materials were modeled as Lennard-Jones spheres with σ_c = 0.340 nm and ε_c/k_B = 28.0 K. Initially all the ions were placed in a lattice at both sides of the carbon materials in the *z* direction, with auxiliary walls closing the entrances to the pores. The carbon atoms in the system were kept fixed in space throughout our simulations. First, the system was subjected to an energy minimization procedure using a

standard steepest descent scheme. After that, the IL was melted at 600 K and subsequently annealed from 600 K to 333 K in three steps for 3 ns. Following this procedure, the auxiliary walls were removed and the ions can enter the carbon porous materials. Averages were accumulated over 20 ns, and over at least two independent simulation runs of the same system. To make sure that our systems were properly equilibrated, in addition to monitoring standard variables (e.g. energy), we also examined the mean square displacement (MSD) and ensured that the ILs have reached the diffusive regime (Figures 2.6). We also monitored the time correlation functions for the rotation of the cations (data not shown for brevity), and ensured that our simulations were long enough to decorrelate the reorientation of the cations with the only exception of those cations that were inside the very narrow carbon nanopipes. The rest of the simulation details and methods are exactly the same as those used in our previous studies.[41, 156-161]

2.3 Results and discussion

In Figures 2.4a and 2.4b we show density maps of [$emim^+$] in the CMK-5 and CMK-3 model materials with H = 2.5 nm, and in Figures 2.4c and 2.4d we show mass density profiles (in g/cm^3) of [$emim^+$] and [NTf_2^-] in the same model materials (in CMK-5, the IL can be adsorbed inside and outside the ACNPs). The mass density profiles shown in Figures 2.4c and 2.4d were determined along the direction indicated by the solid arrow in the density maps shown in Figure 2.4a and 2.4b. The results shown in Figure 2.4 are very similar to those obtained for [$dmim^+$][Cl^-] inside CMK-5 materials with H = 1.8 nm (Figure B1, Appendix) and inside CMK-3 materials of the same pore size (from our previous study[41]). Slight differences are observed in the density profiles of the ions outside of the ACNPs in CMK-5 and outside of the ACNRs in CMK-3 (Figure 2.4d). Peaks in the density profiles are observed in all cases, with the number of peaks

and their positions varying with pore size H and with size of the ions ([$emim^+$] and [NTf_2^-] are larger than [$dmim^+$] and [Cl^-]).

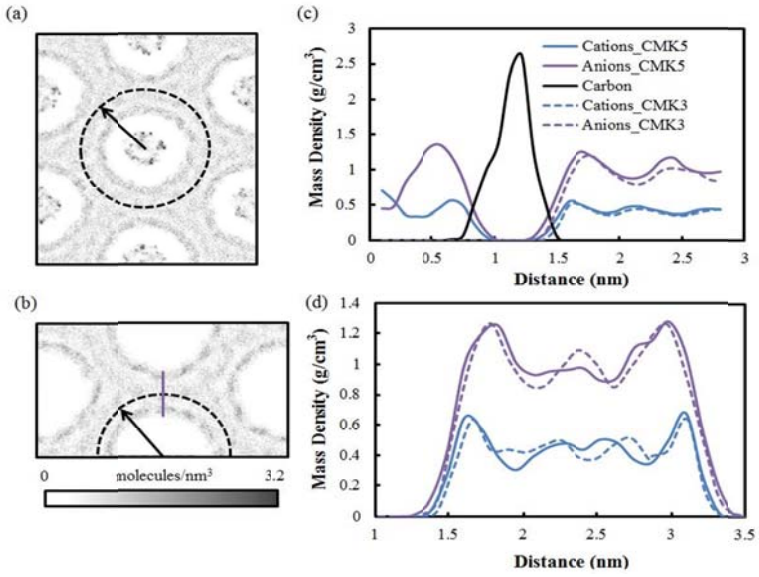

Figure 2.4 (a, b) Density map of [$emim^+$] cations inside our model CMK-5 (a) and CMK-3 (b) materials (H = 2.5 nm). Areas with higher density of cations are depicted in darker shades of grey. (c) Density profiles of [$emim^+$] and [NTf_2^-] inside and outside the carbon nanopipes of CMK-5 or the carbon nanorods of CMK-3, along the direction indicated by the solid arrow in the density maps shown in Figure 2.4a-b, and up to the distance indicated by the dashed circle in Figure 2.4a (i.e., half the distance between neighboring ACNPs or ACNRs). (d) Density profile of [$emim^+$] and [NTf_2^-] outside the ACNPs of CMK-5 and outside the ACNRs of CMK-3. Here the density profiles are measured from the outer surface of two neighboring ACNPs (or ACNRs), along the direction indicated by the solid arrow in the density maps shown in Figure 2.4a-b.

In Figure 2.5 we show representative simulation snapshots of [$emim^+$] and [NTf_2^-] inside the CMK-3 and CMK-5 model materials, where the atoms of each ion are colored according to their total mobilities over a time of 10 ns. These results qualitatively show that the ions near the amorphous carbon surfaces have lower mobility compared to that of the ions that are further away from the pore walls. In the CMK-3 systems (Figure 2.5a-b), the ions that are in the layers that are closer to the carbon walls have a consistent dark blue color, indicating that their dynamics are slow and relatively homogeneous. In contrast, the ions in the layers closer to the

outside surfaces of the ACNPs in CMK-5 have more mixed colors, indicating that the dynamics of the ions in these layers are more heterogeneous and faster as compared to those of their counterparts in CMK-3. Spatial heterogeneity in the dynamics is also noticeable for the ions that are further away from the carbon surfaces of CMK-3 and CMK-5. These snapshots also indicate that the ions inside the ACNPs of CMK-5 have the slowest dynamics, mainly because of the small value of the average internal diameter of the ANCPs (~1.5 nm), which subject the ions to a very large degree of confinement. Results for [dmim$^+$][Cl$^-$] inside CMK-3 and CMK-5 (Figure B2, Appendix) show trends that are qualitatively similar to those observed for [emim$^+$][NTf$_2^-$]; however, the dynamics of [dmim$^+$][Cl$^-$] inside the ACNPs of CMK-5 seem to be at least qualitatively similar to those of the same ions outside of the ACNPs. These trends can be explained by a combination of the following factors: (1) the ions in [dmim$^+$][Cl$^-$] are smaller than those in [emim$^+$][NTf$_2^-$], and thus the former are less confined when inside the ACNPs; (2) cation-anion interactions and ions-carbon interactions are different in these two ILs.

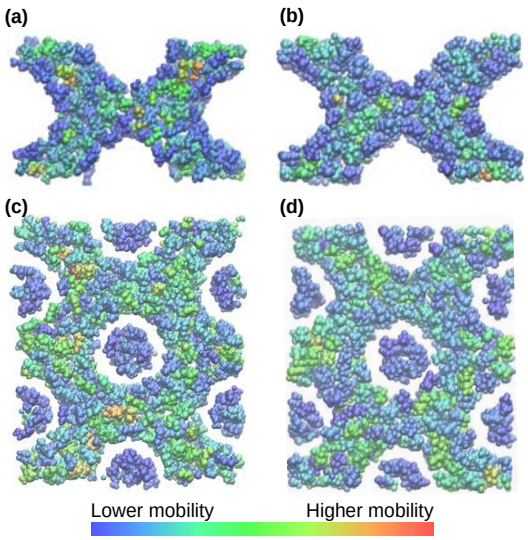

Figure 2.5 Representative simulation snapshots of [emim$^+$] (left) and [NTf$_2^-$] (right) inside our CMK-3 (top) and CMK-5 (bottom) model materials, H = 2.5 nm. The ions are colored according to their displacement over a time of 10 ns. The carbon atoms in our CMK-3 and CMK-5 model materials are not shown.

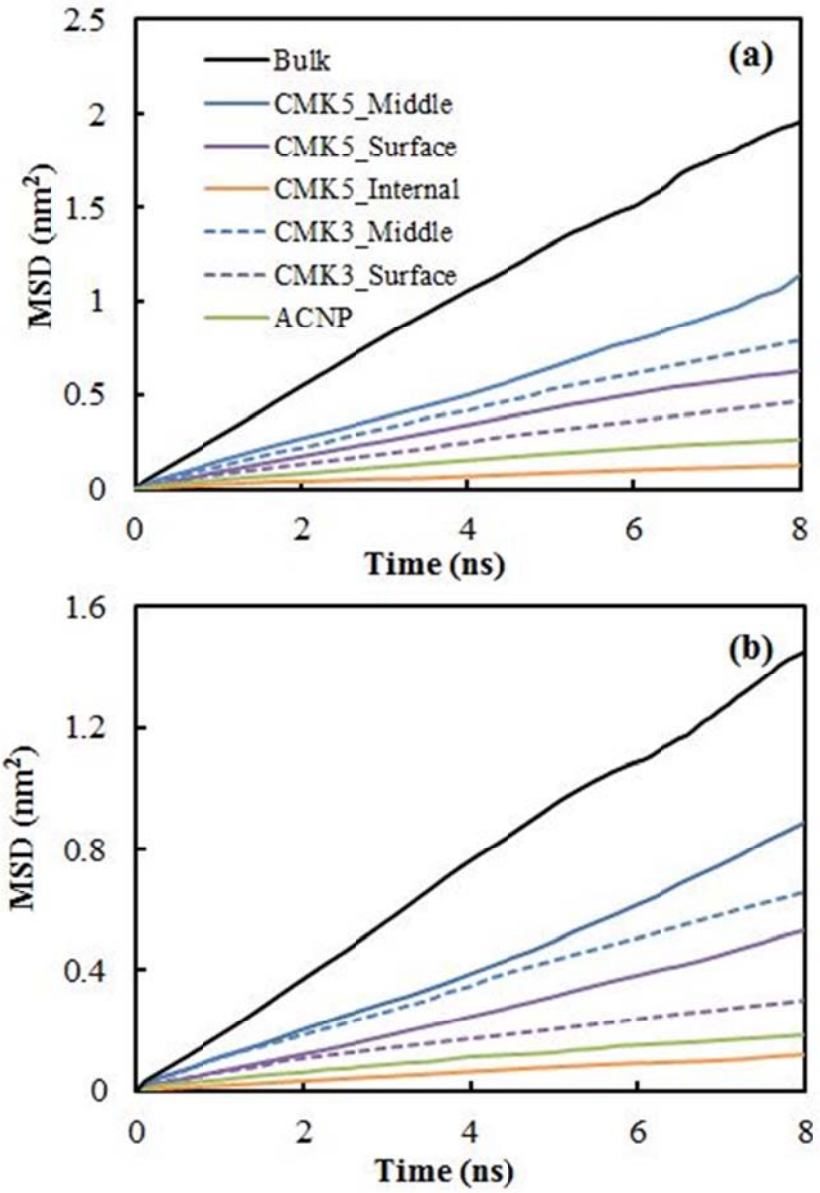

Figure 2.6 Axial component (*z*-direction) of the mean square displacement (MSD) of the (a) [$emim^+$] cations, and (b) [NTf_2^-] anions, in the model CMK-3 and CMK-5 materials and inside an isolated amorphous carbon nanopipe (ACNP). The different curves depicted represent the following: 'Bulk' = ions in a bulk system; 'CMK3_Surface' or 'CMK5_Surface' = ions that are outside of the ACNRs in CMK-3 or the ACNPs in CMK-5, and close to the external carbon walls of the ACNRs or ACNPs (i.e., located within the first peak of the density profiles of the ions in Figure 2.4c); 'CMK3_Middle' or 'CMK5_Middle' = ions that are outside of the ACNRs in CMK-3 or the ACNPs in CMK-5, and away from the external carbon walls of the ACNRs or ACNPs (i.e., located outside of the first peak of the density profiles of the ions in Figure 2.4c); 'CMK5_Internal' = ions inside the ACNPs of the CMK-5 material; 'ACNP' = ions inside an isolated ACNP.

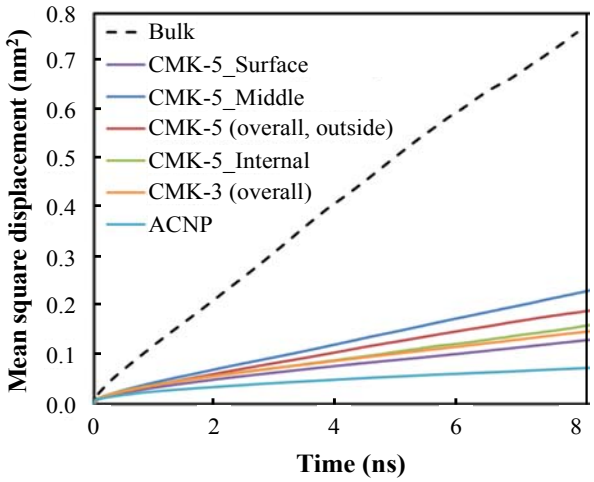

Figure 2.7 Axial component (*z*-direction) of the mean square displacement (MSD) of the cations in [$dmim^+$][Cl^-] in the model CMK-3 and CMK-5 materials and inside an isolated amorphous carbon nanopipe (ACNP). The different curves depicted represent the following: 'Bulk' = ions in a bulk system; 'CMK5_Surface' = ions that are outside of the ACNPs in CMK-5, and close to the external carbon walls of the ACNRs or ACNPs (i.e., located within the first peak of the density profiles of the ions in Figure 2.5c); 'CMK5_Middle' = ions that are outside of the ACNPs in CMK-5, and away from the external carbon walls of the ACNRs or ACNPs (i.e., located outside of the first peak of the density profiles of the ions in Figure 2.5c); 'CMK-5 (overall, outside)' = all the ions that are outside of the ACNPs in CMK-5; 'CMK5_Internal' = ions inside the ACNPs of the CMK-5 material; 'CMK-3 (overall)' = all the ions that are outside of the ACNRs in CMK-3; 'ACNP' = ions inside an isolated ACNP.

We further investigated the dynamics of [$emim^+$][NTf_2^-] and [$dmim^+$][Cl^-] inside our CMK-3 and CMK-5 model materials, as well as inside an isolated ACNP (Figure 2.2d), by monitoring the axial component of the mean squared displacements (MSDs) of the ions as a function of time; these results are depicted in Figures 2.6 (for [$emim^+$][NTf_2^-]) and 2.7 (for [$dmim^+$][Cl^-]). In these results we have split the ions into different layers based on their density profiles (Figure 2.4 for [$emim^+$][NTf_2^-], and Figure B1 in Appendix for [$dmim^+$][Cl^-]), in order to study the local dynamical behaviors of the ions. In Figures 2.6 and 2.7, the curve 'CMK5_Internal' represents the dynamics of the ions inside the ACNPs of the CMK-5 material;

the lines for ‘CMK3_Surface’ or ‘CMK5_Surface’ depict the axial MSDs of the ions that are closest to the external walls of the ACNRs in CMK-3 and the ACNPs in CMK-5, i.e., located within the first peak of the density profiles of the ions in Figures 2.4c and B1c in Appendix; and the lines labeled ‘CMK3_Middle’ or ‘CMK5_Middle’ represent the dynamics of the rest of the ions in these systems. The MSDs of the IL ions in a bulk system at the same temperature are also shown in Figures 2.6 and 2.7. As expected, all ions confined inside our model porous materials exhibit dynamics that are slower than those observed in a similar bulk system. In agreement with the results qualitatively shown in Figure 2.5a and 2.5b for [$emim^+$][NTf_2^-], the ions inside the ACNPs of CMK-5 exhibit the slowest dynamics (Figure 2.6); and the ions closer to the carbon surfaces in CMK-3 move slower than the ions that are further away from these surfaces. Similarly, the ions closer to the outer surface of the ACNPs of CMK-5 move slower than the ions that are further away from these surfaces.

Interestingly, the results shown in Figure 2.6 indicate that the ions in the surface layer and middle regions in CMK-5 exhibit dynamics that are slightly faster than those of their counterparts in the same layers/regions in CMK-3 (the surface-to-surface distances between ACNPs in CMK-5 and ACNRs in CMK-3 are exactly the same). This observation might be due to several reasons. Subtle differences in the density of the IL outside the CMK-5 nanopipes and the CMK-3 nanorods might be a possibility; although the density profiles of the IL outside the CMK-5 nanopipes and the CMK-3 nanorods (Figure 2.4) are qualitatively similar, the ions outside of the ACNPs in CMK-5 seem to be closer to the carbon surfaces than the ions in CMK-3. A second reason might be correlation effects between the IL that is inside the CMK-5 nanopipes and the IL that is adsorbed on the outer surface of the ACNPs. We raise this issue because in Figure 2.6 we also report results for the axial MSD of the ions inside an isolated

ACNP (i.e., no IL adsorbed outside the ACNP, Figure 2.2d). These results indicate that the ions of [$emim^+$][NTf_2^-] inside an isolated ACNP move slightly *faster* than the ions inside the ACNPs in CMK-5 (which have IL adsorbed at the outer surface of the ACNPs). However, this dynamical behavior seems to depend on the particular IL; in Figure 2.7 we show results similar to those presented in Figure 2.6a, but now for the cations of [$dmim^+$][Cl^-] inside CMK-3 and CMK-5 materials with a pore size of H = 1.8 nm (the average internal diameter of the ACNPs is ~1.5 nm, same as in our simulations with [$emim^+$][NTf_2^-]; results for the [Cl^-] anions follow the same trends as the [$dmim^+$] and are not shown for brevity). The results shown in Figure 2.7 indicate that [$dmim^+$] outside of the ACNPs in CMK-5 has slightly faster dynamics than the cations outside of the nanorods in a CMK-3 material of the same pore size, in analogy to what we observed for [$emim^+$] in Figure 2.6a. These results suggest that the presence of IL inside the ACNPs can accelerate the dynamics of the IL outside of the ACNPs in CMK-5, with respect to those observed for the same ILs in CMK-3 materials. The IL adsorbed outside of the ACNPs in CMK-5 experiences long-range electrostatic interactions with the ions inside the ACNPs, in addition to the interactions with the thin carbon walls of the ACNPs (average thickness = 0.45 nm); in contrast, the IL adsorbed in CMK-3 materials only interacts with the carbon atoms of the ACNRs. The results depicted in Figure 2.7 also indicate that [$dmim^+$] inside an isolated ACNP moves *slower* than the same cations inside the ACNPs in CMK-5; however, the opposite behavior was observed for [$emim^+$][NTf_2^-] (Figure 2.6a), namely the ions inside an isolated ACNP move slightly *faster* than the same ions inside the ACNPs in CMK-5 (i.e., with IL adsorbed in the outer surface of the ACNPs). Furthermore, results from Figure 2.7 indicate that the MSD of [$dmim^+$] inside the ACNPs in CMK-5 (average internal diameter D = 1.5 nm) is

slightly larger than the average MSD of all the cations in a CMK-3 material of pore size H = 1.8 nm.

Table 2.1 Diffusion coefficients for [$dmim^+$][Cl^-] and [$emim^+$][NTf_2^-] in the bulk and along the axial direction in our pore systems. Values inside parentheses represent the uncertainties in our calculations.

	D ($\times 10^{-7}$ cm^2/s)			
	[$dmim^+$]	[Cl^-]	[$emim^+$]	[NTf_2^-]
Bulk	2.45 (0.02)	1.86 (0.05)	12.30 (0.05)	9.01 (0.04)
CMK-3 (overall)	0.73 (0.03)	0.48 (0.06)	4.36 (0.03)	3.42 (0.02)
CMK-3 (surface)	-	-	2.85 (0.02)	1.75 (0.03)
CMK-3 (middle)	-	-	4.89 (0.03)	4.02 (0.02)
CMK-5 (outside, overall)	1.04 (0.13)	0.58 (0.05)	5.92 (0.04)	4.56 (0.04)
CMK-5 (outside, surface)	0.66 (0.13)	0.38 (0.03)	4.00 (0.04)	3.27 (0.03)
CMK-5 (outside, middle)	1.31 (0.02)	0.75 (0.13)	6.71 (0.06)	5.35 (0.06)
CMK-5 (inside)	0.82 (0.01)	0.58 (0.01)	0.76 (0.01)	0.72 (0.01)
Isolated ACNP	0.28 (0.02)	0.20 (0.02)	1.62 (0.02)	1.11 (0.02)

The results shown in Figures 2.6 and 2.7, and in Table 2.1 (self-diffusion coefficients in the z-direction, as calculated from the MSDs shown in Figures 2.6 and 2.7) indicate that the ions adsorbed outside of the ACNPs in CMK-5 have faster dynamics than the same ions adsorbed outside of ACNRs of the same external diameter in CMK-3 materials of the same pore size. Our results also show that the dynamics of an IL inside an ACNP can be significantly affected when IL is present outside of the ACNP in CMK-5 materials. These observations might be due to correlation effects between the IL inside and outside the ACNPs in CMK-5 (the average thickness of the carbon wall in the ACNPs is about 0.45 nm). Interactions between molecules located in neighboring pores can act in a cooperative way and are known to induce important

changes in the behavior of confined fluids. For example, molecular simulations[162] have shown that methane inside neighboring cylindrical pores in the zeolite $AlPO_4$-5 can undergo a gas-liquid phase transition; however, no phase transitions are observed when methane is inside an isolated cylindrical pore of the same material and size, because the pore diameter is smaller than twice the molecular diameter of methane and thus the system is very close to the one-dimensional limit.[163] Very recently, an order-disorder transition was also observed in molecular simulations of water inside a membrane with neighboring, narrow cylindrical pores arranged in a square lattice.[164] Kondrat *et al.*[165] and Péan *et al.*[166] indicate that ILs inside sub-nm pores can experience very fast dynamics during charging processes, due to a complex interplay between factors such as confinement in very narrow pores, ion crowding, screened interactions and changes in the structure of the double layer caused by the charging process. Kondrat *et al.*[165] also report that tuning the interactions of the ions with the pore walls (e.g., by using mixtures of ILs or by adding surfactants) to have 'ionophobic' pore surfaces can further accelerate the dynamics of the confined ions during the charging process. Our results indicate that the presence of IL in the *outer* surface of an *uncharged* ACNP (average thickness of the carbon wall = 0.45 nm) can affect the dynamics of an IL adsorbed *inside* the carbon nanopipe, and vice versa (as the dynamics of the ILs outside of the ACNPs in CMK-5 were found to be faster than those of the same ILs in CMK-3). Differences in the cation-anion interactions, as well as the ion-walls interactions might also cause differences in the dynamics, as $[dmim^+][Cl^-]$ inside an isolated ACNP moves *slower* than inside the ACNPs in CMK-5 (Figure 2.7 and Table 2.1), but $[emim^+][NTf_2^-]$ inside an isolated ACNP moves slightly *faster* than inside the ACNPs in CMK-5 (Figure 2.6 and Table 2.1).

To further explore the properties of the ions inside the ACNPs when the nanopipes have, or do not have, IL adsorbed in their outer surface, in Figure 2.8 we show radial and axial density profiles of [$emim^+$] and [NTf_2^-] inside an isolated ACNP (i.e., no IL adsorbed on its outer surface, Figure 2.2d), and inside the ACNPs in CMK-5 (i.e., IL present outside of the ACNPs, Figures. 2.3c and 2.3d). The radial density profiles for [$dmim^+$][Cl^-] inside an isolated ACNP are included in Figure B3 in Appendix; similar results for the same IL but now inside the ACNPs in CMK-5 are shown in Figure B3 in Appendix. The axial density profiles for the same IL inside an isolated ACNP and inside the ACNPs in CMK-5 are depicted in Figure 2.9. The peaks in the radial density profiles of the ions inside the ACNPs (Figure 2.8a, Figure B1 and Figure B2 in Appendix) are closer to the carbon surfaces when IL is adsorbed in the outer surfaces of the ACNPs in CMK-5, as compared to the case of an isolated ACNP (i.e., no IL outside of the ACNP). The mass density profiles of the ions inside the ACNP as a function of the axial distance, which are depicted in Figures. 2.8b and 2.9, show a slightly non-uniform distribution of the ions that might be caused by the uneven internal diameter of the ACNP (Figure 2.2). The average axial density of the ions inside the ACNPs is slightly larger in CMK-5 (when IL is adsorbed outside of the ACNPs) than inside an isolated ACNP. These results suggest that the presence of IL adsorbed in the outer surfaces of the ACNPs in CMK-5 induce changes in the density of the IL inside the ACNPs, which in turn affects the dynamics of the ions inside the ACNPs. Our previous studies[41, 157, 159, 161] indicate that variations in the amount of IL inside the nanopores can affect significantly the dynamics of the confined ions. Furthermore, the ions of [$dmim^+$][Cl^-] inside the ACNPs (both isolated and in CMK-5) seem to have average axial densities that are similar to those of the bulk IL (Figure 2.9). In contrast, the average axial densities of [$emim^+$] and [NTf_2^-] inside the ACNPs appear to be slightly lower than the densities of the same ions in the bulk-like reservoirs at both

sides of the porous materials (Figure 2.8b). These differences in the density of the ILs inside the ACNPs as compared to those of the bulk IL reflect the difference in the interactions between the carbon walls and [dmim$^+$][Cl$^-$] and [emim$^+$][NTf$_2^-$], which in turn also affect the dynamical behavior of these ILs inside our model materials (Figures 2.6 and 2.7). Differences in pore size might also play a role in these observations (H = 2.5 nm for [emim$^+$][NTf$_2^-$], whereas H = 1.8 nm for [dmim$^+$][Cl$^-$]).

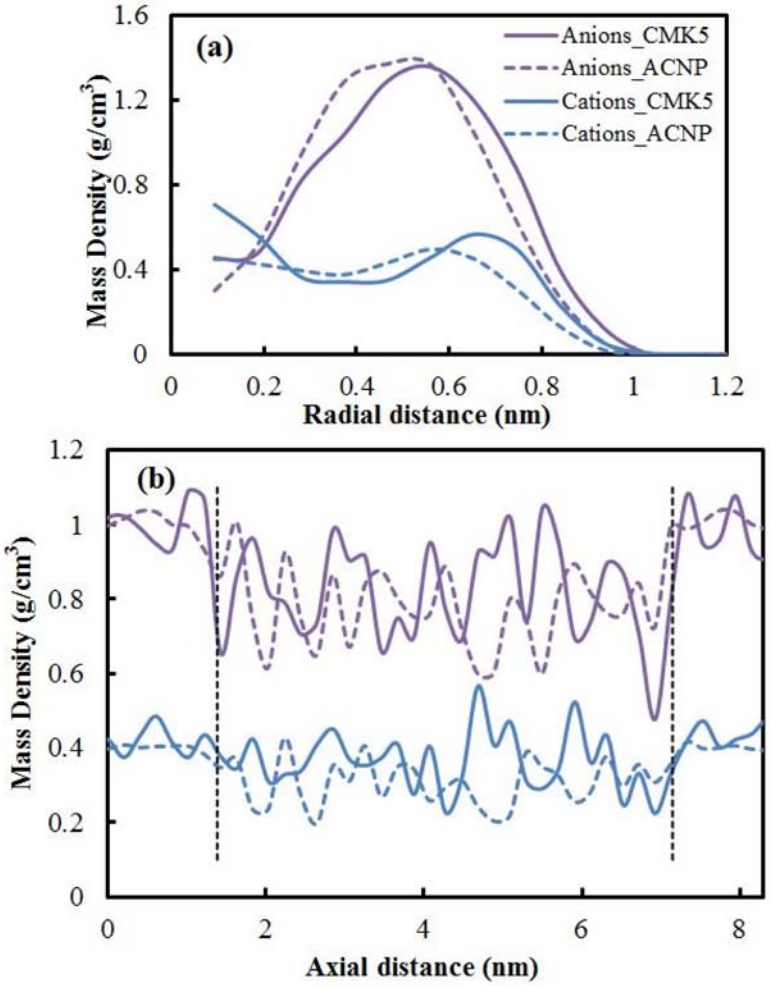

Figure 2.8 Mass density profiles for [emim$^+$][NTf$_2^-$] inside the ACNPs of CMK-5 and inside a single ACNP. (a) Radial density profiles. (b) Axial density profiles. The dashed lines indicate the approximate location of the edges of the ACNPs in our simulation boxes (see Figures 2.2d and 2.3c).

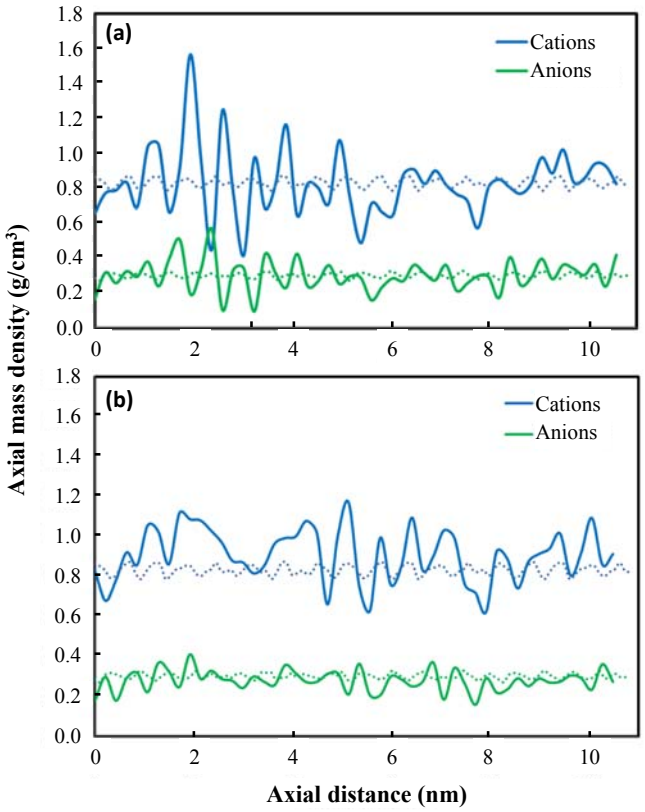

Figure 2.9 Mass density profiles in the axial direction for [dmim$^+$][Cl$^-$] inside (a) an isolated ACNP, and (b) the ACNPs in CMK-5. Dotted lines are cation and anion densities in a simulated bulk IL system at the same temperature.

2.4 Concluding remarks

Classical molecular dynamics (MD) simulations were conducted to study the structure and dynamics of the ionic liquids (ILs) [dmim$^+$][Cl$^-$] and [emim$^+$][NTf$_2^-$] confined inside a model CMK-5 material of pore sizes H = 1.8 nm and 2.5 nm respectively. This material is formed by nanopipes made of amorphous carbon, where the nanopipes are arranged in a hexagonal array; the amorphous carbon nanopipes (ACNPs) have an average diameter D = 1.5 nm and an average wall thickness of 0.45 nm. In CMK-5, the ILs can be adsorbed inside and outside the ACNPs (Figure 2.3d). Our findings were compared against similar results observed for the same ILs inside an isolated ACNP (i.e., no IL adsorbed on the outer surface of the ACNP) and inside a

model CMK-3 ordered mesoporous carbon of similar pore size. CMK-3 is very similar to CMK-5, but is made of hexagonally-packed amorphous carbon nanorods (ACNRs, see Figure 2.3b). No electrical charges were present in any of these carbon materials. Our results indicate that the presence of IL adsorbed in the outer surface of an uncharged carbon nanopipe can affect significantly the dynamics and the density of an IL adsorbed inside the carbon nanopipe, and vice versa. Both of the ILs examined here have faster dynamics when they are adsorbed outside of the ACNPs in CMK-5 (i.e., with IL inside of the ACNPs) than when they are in CMK-3 materials of the same pore size. Radial density profiles indicate that the ions prefer to remain closer to the carbon walls in CMK-5 than in CMK-3, possibly due to the presence of ions inside and outside the thin walls of the ACNPs (average wall thickness = 0.45 nm). The average axial density of both ILs inside the ACNPs is slightly larger in CMK-5 (when IL is adsorbed outside of the ACNPs) than inside an isolated ACNP. These results suggest that the presence of IL adsorbed in the outer surfaces of the ACNPs in CMK-5 induces changes in the density of the IL inside the ACNPs. The presence of IL adsorbed outside of the ACNPs also affects the dynamics of the IL inside the ACNPs; [$dmim^+$][Cl^-] inside an isolated ACNP has slower dynamics than when inside the ACNPs in CMK-5 (i.e., with IL adsorbed outside the ACNPs), but in contrast, [$emim^+$][NTf_2^-] inside an isolated ACNP moves faster than when inside the ACNPs in CMK-5. Furthermore, the average axial density of [$dmim^+$][Cl^-] inside the ACNPs (both isolated and in CMK-5) seems to be similar to that of the same IL in the bulk, whereas [$emim^+$][NTf_2^-] inside the ACNPs has an average axial density that is slightly lower than that of the bulk IL. These results strongly suggest that the interactions between the ions and the pore walls significantly influence the structure and dynamics of the ILs in these systems. Overall, our results suggest the presence of correlation effects between the IL inside and outside the ACNPs in CMK-5.

Interactions between molecules located in neighboring pores can act in a cooperative way and are known to induce important changes in the behavior of several nonpolar and polar fluids inside nanopores.[163-164] Correlation effects might play an important role in determining the macroscopic properties of the electrical double layer near charged surfaces;[25,26] these effects deserve further investigation in follow-up studies.

Chapter 3 Molecular Simulation of Homogeneous Nucleation of Crystals of an Ionic Liquid from the Melt[†]

3.1 Introduction

Ionic liquids (ILs) are defined as "organic salts with a melting temperature below the boiling point of water".[1] In most of current applications of ILs (e.g., solvents for synthesis, catalysis and separations, electrolytes, absorbents for CO_2 capture, etc.),[1-2, 14, 113, 119, 167-171] these organic salts are in liquid phase. However, in recent work Warner *et al.*[45-49, 64, 172-176] synthesized nanomaterials based on organic salts that are in solid phase at room temperature. These organic salts were termed 'GUMBOS' (Group of Uniform Materials Based on Organic Salts), as all of them have melting points that can be above and below 100 °C (and thus depart from the traditional definition of ILs). Fluorescent and magnetic GUMBOS-based nanomaterials were synthesized as part of these studies.[45-49, 64, 172-176] The simplicity of the synthesis procedures, combined with the versatility and highly-tunable properties of the organic salts (as many as 10^9 – 10^{18} ILs could be formed by varying the structure of the cations and anions[1]), suggest potential applications of these nanomaterials in fields as diverse as biomedicine, analytical chemistry, optoelectronics, photovoltaics and separations.[45-49, 64, 172-176] Further tunability of the magnetic and optical properties can be achieved by introducing shape anisotropy; the Warner group synthesized fluorescent 1D-nanomaterials (e.g., nanorods, nanotubes and nanowires) based on organic salts,[64] by introducing these compounds inside anodic alumina membranes and other hard templates, e.g., carbon nanotubes and mesoporous silicas. 1D-nanoGUMBOS with diameters between 20 to 500 nm and lengths of 1 to 20 μm were synthesized in that study.[64]

[†] Contents of this chapter were published in the following article: He, X.; Shen, Y.; Hung, F. R.; Santiso, E. E. Molecular simulation of homogeneous nucleation of crystals of an ionic liquid from the melt. *The Journal of Chemical Physics* **2015**, *143*, 124506. http://dx.doi.org/10.1063/1.4931654

Furthermore, ionogels, a new class of hybrid materials,[62-63, 127-128, 177] involve a solid-like network formed by immobilizing ILs within nanoporous solids (e.g., carbon nanotubes, porous silicas, organic gelators, polyethylene oxide, cellulose, etc.) Ionogels have potential applications as solid electrolyte membranes in lithium batteries, fuel cells and solar cells, and in optics, catalysis and biocatalysis, drug delivery and sensing and biosensing.[63] Therefore, a fundamental understanding of solidification of organic salts inside nanopores is crucial to rationally design these nanomaterials, as features such as the nanostructure of the IL can determine their macroscopic properties. Recent studies[178-183] also indicate that when pharmaceutically relevant molecules (e.g., acetaminophen, glycine) are confined inside narrow pores, they can crystallize into structures that are different from those observed in the bulk. These studies provide strong evidence that nanoconfinement can be used to control polymorphism.[178-183]

In addition to the practical interest described above, understanding the solidification as well as the nucleation and growth of crystals of organic salts in contact with surfaces and inside nanopores is also a topic of fundamental scientific interest. However, the nucleation and growth of crystals of ILs is still far from understood even for bulk systems, as most of the interest has focused on liquid phases of these compounds. As a starting point for our studies in this area, here our focus was on the study of the homogeneous nucleation of crystals of ILs from its supercooled liquid phase in the bulk, where temperature drives the nucleation process. Homogeneous nucleation is a rare event that first involves the system climbing a free energy barrier to form an activated, short-lived species, the critical nucleus; the second process involves the growth of this nucleus to form the crystal phase. Studying nucleation is extremely challenging.[184-191] The critical nucleus can appear anywhere in the system and typically involves a few molecules or ions, which makes its direct detection in experiments almost impossible. Molecular simulation

studies of nucleation are also challenging, mainly because the relevant time scales are orders of magnitude larger than those accessible to conventional molecular dynamics (MD) simulations. Simulations with rare event methods have provided insights on the homogeneous nucleation of systems of particles (colloidal, hard-sphere, Lennard-Jones, Yukawa and others),[67, 192-200] water,[201-209] and other systems (e.g., NaCl, silicon, benzene, n-octane, urea, copper, aluminum, etc.)[210-220] To the best of our knowledge, the homogeneous nucleation of ILs has not been studied in the past.

Here we studied the homogeneous nucleation of crystals of a typical IL, 1,3-dimethylimidazolium chloride, [dmim$^+$][Cl$^-$], from its supercooled liquid phase. This IL has a simple molecular structure and has been studied extensively in previous simulation reports.[41, 221-228] Here we followed the work of Ovchinnikov *et al.*[229] and used their same combination of methodologies: first the string method in collective variables (SMCV),[230] to have a string of replicas of the system relax in the direction of the negative gradient of the free energy; after convergence, the string should sketch a minimum free energy path (MFEP, or the region that has the highest probability for the transition to take place) connecting the supercooled liquid and the crystal phase of the IL. This converged string of states from the SMCV was then used as input to a series of MD simulations using Markovian milestoning with Voronoi tessellations.[231-233] This method yields the free energy along a 'reaction coordinate' parameterizing the transition, as well as the mean first passage times (MFPTs) between the relevant states involved. This combination of methods has been used in the past to study conformational transitions in biomolecules.[229-230, 232, 234-240] Central to our methods is the selection of a set of collective variables (order parameters, OPs) that are appropriate for describing the transition of interest. In prior studies involving biomolecules, the OPs were simply the Cartesian coordinates of the relevant atoms or groups of

atoms/particles. Studying crystal nucleation, however, requires OPs that allow one to measure local crystalline order in nm-sized regions, as well as distinguish between different crystal polymorphs and liquid phases. In this study we have combined the SMCV and Markovian milestoning with the OPs for molecular crystals recently developed by Santiso and Trout.[241] These OPs were successfully used to monitor the nucleation of α-glycine crystal in solution, the crystallization of benzene from the melt, and the polymorph transformation of terephthalic acid in bulk systems.[217, 241]

Our combination of methods and OPs allowed us to monitor the homogeneous nucleation of [$dmim^+$][Cl^-] and provided insights about the mechanism, the free energy barrier, the size of the critical nucleus and the rates involved in the nucleation process. In fact, these methods were also used recently[242] to study the homogeneous nucleation of benzene; the results were similar to those obtained for the same system using transition path sampling / aimless shooting.[217] However, for very complex systems such as ILs, which have slow dynamics, the transition paths might take a long time to commit to one of the stable states. Furthermore, sampling could be time consuming and challenging, as the trajectories might recross the top of the barrier multiple times.[217] The SMCV is a good alternative because it does not require generating trajectories that follow the transition path, or monitoring the time evolution of the system along such path; rather, the set of replicas of the system converge to the MFEP guided by the negative gradient of the free energy. Once this MFEP is mapped, Markovian milestoning with Voronoi tessellations is convenient to obtain the free energy and rates involved in nucleation because (1) it follows naturally from the SMCV, in the sense that the milestones are defined automatically by the OPs from the converged images in the MFEP, and (2) Voronoi milestoning is easy to implement if one builds from the restrained dynamics code that was used in the SMCV. Furthermore, our

combination of methods is not based on classical nucleation theory (CNT), and therefore makes no assumptions regarding its validity for our systems (in fact, independent calculations based on CNT were used to help in the interpretation of some of our results, see below).

The rest of the paper is structured as follows. In the next section, we provide details of our models, the construction of OPs for our systems and our main computational methods (SMCV and Markovian milestoning with Voronoi tessellations). Section 3.3 contains our main results and discussion: first we sketched a MFEP connecting the supercooled liquid and the crystal phase of the IL using the SMCV (§3.3.1), and then we used Markovian milestoning with Voronoi tessellations to determine the free energy involved in the homogeneous nucleation process (§3.3.2). Calculations based on classical nucleation theory are presented in §3.3.3 to discuss the physical significance of the configurations found along this minimum free energy path. Section 3.3.4 contains additional SMCV results obtained for a larger system (2268 ion pairs, as compared to the 1372 ion pairs used for the results shown in §3.3.1); these results support the analysis presented in §3.3.3. The MFPTs involved in the homogeneous nucleation process are presented in §3.3.5. As simulations using Markovian milestoning with Voronoi tessellations are computationally very expensive, we only present MFPT results for our system with 1372 ion pairs; we did not attempt to obtain similar results for our larger system. Finally, our main findings are summarized in section 3.4.

3.2 Models

The crystalline structure of the IL [dmim$^+$][Cl$^-$] was taken from the Cambridge Crystallographic Data Centre.[243] As reported by Arduengo *et al.*,[244] this IL has a monoclinic crystalline structure with space group $P2_1/n$. The all-atom nonpolarizable force field of Lopes, Pádua *et al.*[84-88] was used in our study to represent the IL [dmim$^+$][Cl$^-$], mainly because it can

satisfactorily reproduce the crystallographic parameters of this IL.[84] In our MD simulations of the liquid phase of this IL, it was found that the bulk density differs in less than 1% from the experimental value reported by Fannin *et al.*;[245] furthermore, our results for the radial distribution functions were in excellent agreement with those reported by Sha *et al.*[221] The experimental melting point of this IL was reported[245] to be 398.15 K; we performed a series of simulations to quickly estimate the simulated melting point of this IL using the void-induced melting method,[246] and obtained results in reasonable agreement with the experimental melting point (nevertheless, we note that a recent study[247] suggests that the void-induced melting method yielded inaccurate results for the melting point of another IL, [bmim$^+$][Cl$^-$]). We also performed short, 1-ns MD simulations of the crystal phase of [dmim$^+$][Cl$^-$], to corroborate that the chosen force field can yield crystallographic parameters for this IL that are compatible with previously reported simulation and experimental results. In particular, we obtained that the β angle of the monoclinic unit cell of this IL is $\beta = 108.2°$ at the conditions of interest for this study, $P = 1$ bar and $T = 340$ K (this temperature is about 58 K lower than the melting point of this IL). This result is in good agreement with previously reported values from simulations[84] ($\beta = 108.9°$) and experiments[244] ($\beta = 106.34°$), both obtained at $T = 203$ K.

Most of our systems contained 1372 ion pairs, which can form a monoclinic crystal of characteristic dimensions 6.5 nm × 5.3 nm × 7.5 nm. However, we also performed SMCV simulations using a larger system containing 2268 ion pairs (characteristic dimensions 8.3 nm × 5.3 nm × 9.7 nm; see §3.4). All MD simulations were performed using a modified version of the NAMD software[248] that included implementations of the OPs, the SMCV and Markovian milestoning with Voronoi tessellations in C++ libraries. All the simulations were performed in the *NPT* ensemble with $P = 1$ bar and $T = 340$ K. A time step of 0.5 fs was used in our

simulations, and a Langevin thermostat with a damping coefficient of 25 ps^{-1} was employed to maintain the temperature at 340 K. The Nosé-Hoover Langevin piston with a damping time of 50 fs was used to control the pressure in our simulations. The cutoff of Lennard-Jones interactions was set at 10 Å. The long range electrostatics were handled by particle mesh Ewald (PME)[249] with a cutoff of 12 Å. The hydrogen bond lengths were constrained with the LINCS algorithm[250]. Periodic boundary conditions were applied in all directions.

3.3 Methods

3.3.1 Order parameters (OPs)

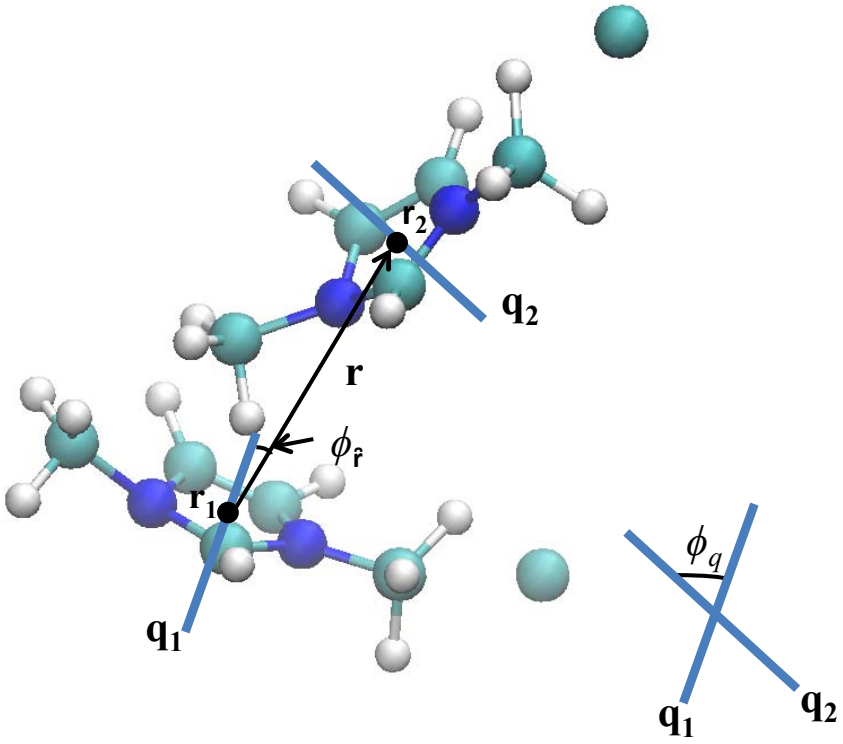

Figure 3.1 Two [$dmim^+$][Cl^-] ion pairs showing variables relevant for the construction of order parameters (OPs) used in this study, which are based on the [$dmim^+$] cations. The vector **r** joins the center of mass of the two cations. The vector normal to the plane of the imidazolium ring gives the absolute orientation **q** of each of the cations. The bond orientation $\phi_{\hat{\mathbf{r}}}$ is given by the angle formed by the vectors **r** and $\mathbf{q}_1$, and the relative orientation ϕ_q is given by the angles between the vectors $\mathbf{q}_1$ and $\mathbf{q}_2$.

The OPs for molecular crystals of Santiso and Trout[241] are extracted from a generalized pair distribution function, which gives the probability that a molecule with a particular internal configuration, has a neighboring molecule (1) with a given internal configuration, (2) is a given center of mass (COM) distance away from the first molecule, and (3) has a given orientation with respect to the first molecule. All OPs used in this study were built based on the [dmim$^+$] cations; no particular OPs were defined for the anions. In Figure 3.1 two ion pairs are shown, where the vector **r** joins the COMs of the two cations. The absolute orientation of each cation is given by the vectors $\mathbf{q}_1$ and $\mathbf{q}_2$, which are normal to the imidazolium ring of each cation. The bond orientation, $\phi_{\hat{\mathbf{r}}}$, is given by the angle formed by the vectors **r** and $\mathbf{q}_1$, and can be described by the projection of the bond vector **r** onto the orientation axis $\mathbf{q}_1$ of the first cation. Finally, the relative orientation, ϕ_q, is given by the angles between the vectors $\mathbf{q}_1$ and $\mathbf{q}_2$. From here we can define local OPs for the COM distances **r**, bond orientation $\phi_{\hat{\mathbf{r}}}$, and relative orientation ϕ_q, following Santiso and Trout;[241] these local OPs are defined per cation and per peak in the pair distribution function. In order to reduce the number of variables, one can sum over peaks in the pair distribution function (to define per-cation OPs) and then average over the cations present in a given subcell of the simulation box. According to the procedure of Santiso and Trout,[241] the bond orientation OPs were defined as follows:

$$\varphi_{\alpha,i}^{bo} = \frac{1}{\sqrt{2\pi}\sigma_\alpha}\frac{1}{2\pi I_0 \eta_{\hat{\mathbf{r}}}^{\alpha}}\sum_{j\neq i}\exp\left[-\frac{\left(r_{ij}-r_\alpha\right)^2}{2\sigma_\alpha^2}\right]\exp\left\{\eta_{\hat{\mathbf{r}}}^{\alpha}\cos\left[2\left(\phi_{\hat{\mathbf{r}}}-\phi_{\hat{\mathbf{r}}}^{\alpha}\right)\right]\right\} \qquad (3.1)$$

where the index α runs over all the unique values of distances, bond orientations, and relative orientations found in the peaks in the pair distribution function of the reference structure of the crystal of the IL; the indexes *i* and *j* denote the *i*-th and *j*-th cations; σ_α is the standard

deviation of bond orientations; I_0 is the modified Bessel function of the second kind and order 0; $\eta_{\hat{\mathbf{r}}}^{\alpha}$ is the concentration parameter corresponding to the α-th peak in bond orientation; r_{ij} is the center of mass distance between cations i and j; r_α is the mean center-of-mass distance corresponding to the α–peak; $\phi_{\hat{\mathbf{r}}}^{\alpha}$ is the bond orientation between two cations in the α-th peak. Equation (1) can be averaged over cations in a given subcell of the simulation box. For example, our typical simulation box (1372 ion pairs) was divided into 5 × 5 × 5 subcells, giving a total of 125 bond orientation OPs for our system. Similar OPs can be defined for the distance and relative orientations.[241]

Table 3.1 Peaks in the pair distribution function for the reference structure of [dmim$^+$][Cl$^-$].

r(Å)	$\varphi_{\hat{r}}$(°)	φ_q(°)
4.84	*49.97*	0.25
5.71	29.59	64.39
5.71	75.33	64.39

Table 3.2 Average peak locations and concentrations parameters for the IL [dmim$^+$][Cl$^-$] crystal at 340 K.

r(Å)	$1/\sigma^2$ (Å^{-1})	$\varphi_{\hat{r}}$(°)	$\eta_{\hat{r}}$	φ_q(°)	η_q
4.92	*23.80*	51.76	11.21	14.10	12.39
5.66	32.79	34.20	4.33	61.97	5.62
5.67	33.99	72.61	9.61	62.75	6.57

In order to estimate values for the average peak locations and concentration parameters for a [dmim$^+$][Cl$^-$] crystal at 340 K, we again followed the procedure of Santiso and Trout,[241] and defined a reference structure by assembling 1372 ion pairs into the crystalline structure reported

by Arduengo *et al.*[244] (however we used β = 108.2°, as determined from the preliminary simulations described in §2.1). This initial structure was then relaxed by performing an MD simulation using the chosen force field at 340 K and 1 bar for 2 ns. Afterwards, the system was annealed to 0 K in the *NVT* ensemble, and finally minimized the energy of the annealed structure. The final crystalline structure was used as the reference structure for our calculations. Table 3.1 shows the peaks in the pair distribution function for the reference structure of the IL, with a cutoff of 5.8 Å for the distances between the COMs. After obtaining the reference structure, we need to obtain the parameters appearing in the probability distribution of Equation (1). Following again the study of Santiso and Trout,[241] the maximum likelihood estimators of the parameters were obtained from the last 1 ns of the *NPT* simulation described above. The average peak locations and concentration parameters for a [$dmim^+$][Cl^-] crystal at 340 K are shown in Table 3.2. These results have slight variations with respect to the reference structure (T = 0 K) shown in Table 3.1, mainly due to thermal effects; the large values of the concentration parameters indicate the distributions are strongly localized around those means.

After obtaining the maximum likelihood estimators, the different types of OPs can be calculated. In Figure 3.2, we plot the distance, bond orientation and relative orientation OPs for the liquid and crystal phases of the IL at 340 K. These distributions were obtained by considering short (0.4 ns) MD simulations in the *NPT* ensemble of liquid-like and crystal-like systems. The results shown in Figure 3.2 indicate that the liquid and solid phases exhibit significantly different values of OPs (even though the peaks of the liquid and crystal phases overlap slightly in the case of the distance OPs), and therefore any of the OPs can serve as a good metric to detect crystalline order in nm-sized regions. We chose the bond orientation OPs for the calculations described

below; however, we also monitored the distance OPs and the relative orientation OPs during all our simulations.

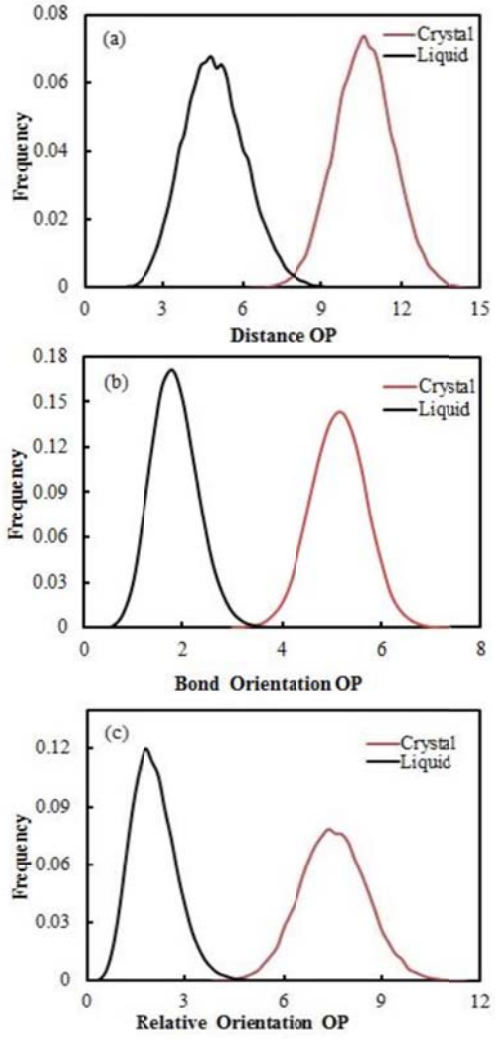

Figure 3.2 The distributions of (a) distance (b) bond orientation (c) relative orientation OPs for liquid and solid IL. These distributions were obtained from the analysis of 400 liquid-like configurations and 400 crystal-like configurations of the IL.

3.3.2 String method in collective variables (SMCV)

The SMCV, as proposed by Maragliano, Vanden-Eijnden and coworkers,[229-232, 235, 251] was developed to determine MFEPs in a given set of collective variables. Here it was used to sketch a MFEP connecting a supercooled liquid phase of [$dmim^+$][Cl^-] with its

thermodynamically stable crystal phase in the bulk, during the homogeneous nucleation process. In this method, first a chain of states (string) connecting the subcooled liquid phase with a crystal phase of the IL is built. In our system, this initial string (consisting of 30 replicas) is obtained by collecting a number of intermediate states observed when melting a crystal phase of the IL in an MD simulation at 900 K. This initial string therefore is a collection of 30 images of the system exhibiting significantly different values of the OPs; each image in this string has 125 OPs characterizing its local structure (for our typical systems containing 1372 ion pairs). These OPs also parameterize the 'reaction coordinate' during the homogeneous nucleation of the crystal phase from its supercooled liquid phase. Here we stress that in our study the OPs represent the collective variables, and the string is a curve in the space of the 125 OPs. A 'metric tensor' (eqn. 6 in ref. [230]) was used to account for the relation between the bond orientation OPs and the Cartesian coordinates of the atoms in our systems; such a metric tensor was routinely computed in our simulations as part of our implementation of the SMCV in NAMD.

An extended Hamiltonian for each replica is built by adding a set of harmonic springs that keep the OPs of each replica close to their 'target value'. Short MD simulations (0.2 ns) in the *NPT* ensemble using this extended Hamiltonian are then run for each replica, in order to calculate the mean force (i.e., the negative gradient of the free energy with respect to the OPs) needed to keep each replica close to the target value of the collective variables. Here we highlight that the mean force computed this way is an approximation of the true constraint force, whose quality depends on the strength of the coupling constant. This group of calculations represents one step in the SMCV simulations. Afterwards, the replicas in the string evolve guided by the mean force. Each image is evolved independently of the other images. The replicas in the string are then reparameterized to prevent the images from clustering near the stable states.

This procedure involves two steps: first, we used b-splines to fit a continuous curve through the replicas after each SMCV step; and second, we used this curve to interpolate between images so that the replicas are kept at approximately constant separation in OP space (measured in terms of the arclength, which is the distance along the path in the multi-dimensional OP space). The steps described above are then repeated until the potential of mean force (PMF, the line integral of the restraint force along the path in the multi-dimensional OP space) converge within the desired level of precision. In our system, we used the Fréchet distance[252-253] between the PMF profiles to monitor the convergence of the string. The Fréchet distance is a measure of the similarity between curves that takes into account the location and ordering of the points along the curves. In our case, convergence was assumed after the Fréchet distance (in arbitrary units) between PMF profiles obtained from successive SMCV steps reaches a value < 0.10. It is also important to note that the two minima of the free energy (i.e., the crystal phase and the disordered phase at the two extremes of the string) are also free to evolve by steepest descent in the free energy, and therefore they will evolve to the nearest free energy minimum in OP space. Additional details about the SMCV are provided elsewhere.[229-230]

3.3.3 Markovian milestoning with Voronoi tessellations

A more accurate estimate of the free energy profile can be obtained by using the converged string from the SMCV as input to another series of simulations using Markovian milestoning with Voronoi tessellations,[229, 231-233] which can also yield information about the rates involved in the transition studied. In this method first we take the converged string of states from the SMCV, define a partition in OP space and associate a cell in OP space to each replica (see black dots in Fig. 5, where the MFEP from the SMCV was projected onto the first two principal components of OP space for visualization purposes). The cells form a tessellation in the OP

space. MD simulations of up to 15 ns were then performed for each replica within their cells, where the images are restricted to remain within their cells (see different colors in Fig. 5). We do emphasize here that we did not use the hard-wall reflection rule described in the original papers of Vanden-Eijnden and Venturoli;[231, 233] rather, we used planar half-pseudoharmonic restraining potentials [i.e., soft wall restraints, eqn. (1) and Fig. 1 in ref. [232]] to keep the images within their cells, while preserving proper ergodic sampling within each of the Voronoi cells. The soft wall restraining potentials serve this function regardless of the ensemble (in our case NPT), and facilitate implementation of the Markovian milestoning procedure in NAMD. The restraining potential is equal to zero in the interior of the cell, and acts as a penalty function if the trajectory leaves its cell. Maragliano *et al*.[232] showed that using these soft walls to run a restrained MD simulation yields an equilibrium distribution inside each cell that is equal to the one obtained from an unbiased MD simulation. In turn, this fact ensures that the fluxes entering and leaving each cell are correct (i.e., the soft wall restraints do not influence the frequency of escape attempts from each cell). Therefore, a restrained MD simulation where the trajectory is forced to remain within its own cell should be equal to the equivalent sections of an unbiased MD trajectory that is passing through the same cell.[232]

In these MD simulations we monitor the number of collisions each replica makes with the boundaries with the neighboring cells. When the system reaches steady state, the following equations can be used to calculate π_n, the probability of finding the system in cell B_n at equilibrium:[229, 231-233]

$$\sum_{\substack{n=1 \\ n\neq m}}^{N} \pi_n \frac{N_{n,m}}{t_n} = \sum_{\substack{n=1 \\ n\neq m}}^{N} \pi_m \frac{N_{m,n}}{t_n} \tag{3.2}$$

$$\sum_{n=1}^{N} \pi_n = 1 \tag{3.3}$$

where $N_{n,m}$ is the number of collisions the replica in cell B_n makes with the boundary of cell B_m during the simulation time t_n. From the probabilities π_n, the free energy F_n along a coordinate parameterizing the transition (in our case the replica number n) can be calculated as follows:[229, 231-233]

$$F_n = -k_B T \ln \pi_n \tag{3.4}$$

As explained by Ovchinnikov *et al.*,[229] the free energy F_n as computed from this procedure (Figure 3.6) is not the same as the free energy as a function of the OPs (in our case, the PMF computed from the SMCV, Figure 3.3). The free energy F_n is one-dimensional, is a function of the reaction coordinate, and it maps the transition tube into a single curve, as argued by Ovchinnikov *et al*.[229] In contrast, the PMF is an n-dimensional function (where n is equal to the number of OPs, i.e., 125 in the case of our system with 1372 ion pairs). As in the SMCV the replicas are restricted to evolve guided by the mean force (i.e., the negative gradient of the free energy with respect to the OPs), we are effectively restraining 125 degrees of freedom. In comparison, in the Markovian milestoning procedure we just constrain each replica to be within its own cell, and therefore less entropy is removed from the system as compared to what happens in the SMCV. Based on this observation, we argue that the free energy F_n as obtained from the Markovian milestoning procedure is more accurate than the PMF to account for the free energy involved in the homogeneous nucleation process.

The Markovian milestoning procedure also allows one to estimate $k_{a,b}$, the rate of instantaneous transition from milestone a to milestone b:[229, 231-233]

$$k_{a,\,b} = \frac{\sum_{n=0}^{N} \pi_n N_{a,\,b}^{n} / t_n}{\sum_{n=0}^{N} \pi_n t_a^{n} / t_n} \tag{3.5}$$

where $N_{a,b}^{n}$ is the total number of transitions from milestone a to milestone b during the simulation confined to cell B_n, and t_a^{n} is total time during which a was the most recent milestone visited by the system. The MFPTs are important dynamical quantities that can be computed through the rate matrix by solving the following system of equations:[229, 231-233]

$$\sum_{b \neq b^*} k_{a,\,b} t_{b,\,b^*} = -1 \quad , \quad a \neq b^* \tag{3.6}$$

where $t_{b,b*}$ is the MFPT to milestone b^* from other milestones in the system (where $b \neq b^*$). For our particular system, the components of the rate matrix varied between 10^{-8} and 10^{-2}, which made it very close to being a singular matrix. This conditioning problem was overcome by using the arbitrary precision floating-point library implemented in the Sage software[254] to solve Eqn. (3.6). Additional details about this method can be found elsewhere.[229, 231-233]

3.4 Results and discussion

3.4.1 Using the SMCV to sketch the MFEP between supercooled liquid and crystal phases of [dmim$^+$][Cl$^-$] at 340 K and 1 bar

As explained above, we first used the SMCV[230] for our system with 1372 ion pairs to have a string of replicas of this system relax in the direction of the negative gradient of the free energy in the multidimensional OP space. After convergence, the string of states maps a MFEP connecting the supercooled liquid and the crystal phase of the IL during the homogeneous nucleation process. The MFEP results are shown in Figure 3.3 for the last three steps of the SMCV. As indicated above, in Figure 3.3 the PMF is the line integral of the restraint force along

the path; and the arclength (of the bond orientation OPs, in this case) represents the distance along the path, where we kept the same distance in OP space between replicas. Keep in mind that the MFEP is the maximum likelihood path, along which the PMF is calculated. The string converges after 28 SMCV steps (Figure 3.3). The convergence of the SMCV was also ascertained by monitoring the Frechét distance (see Figure C1, Appendix) between the PMF curves obtained in successive SMCV steps. Because the initial string of states is obtained by melting a crystal phase of the IL at very high temperature, large changes in the PMF profile were observed during the initial SMCV steps (Figure C1, Appendix). The results shown in Figure 3.3 indicate a difference of about 55 kcal/mol in PMF between the crystal phase and the supercooled liquid phase at about 58 K of supercooling, with a PMF barrier of about 126 kcal/mol between the supercooled liquid and the state at the top of the PMF profile.

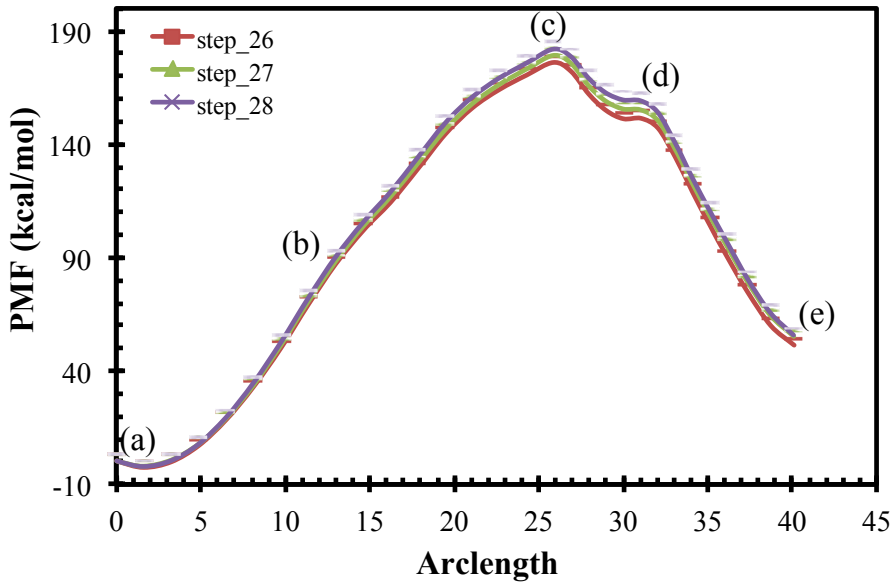

Figure 3.3 The potential of mean force (PMF) associated with the minimum free energy path (MFEP) for homogeneous nucleation of a crystal phase of [dmim$^+$][Cl$^-$] from its supercooled liquid phase at 340 K and 1 bar. These systems contain 1372 ion pairs. The left and right sides of the curve correspond to crystal and liquid states. Simulation snapshots of states labeled here are shown in Figure 3.4.

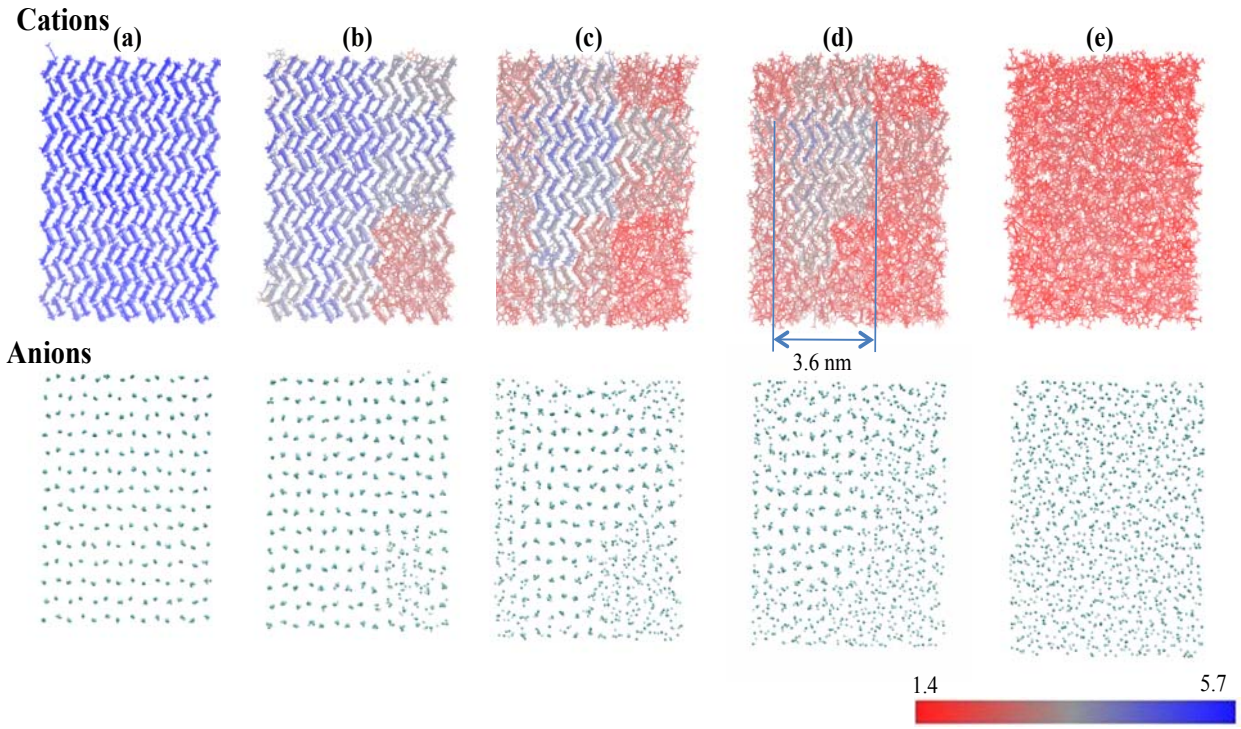

Figure 3.4 Side views (y-*z*) of representative simulation snapshots of the states labeled along the MFEP mapped in Fig. 3. These systems contain 1372 ion pairs. The cations (top row) are colored according to the value of their bond OPs. Additional side views (*x*-*y* and *x*-*z*) of the same states are shown in Figure C2 and C3 (Appendix)

In Figure 3.4 we show side views (*y*-*z*) of representative simulation snapshots of several relevant states along the MFEP mapped in Figure 3.3. The cations are colored according to the value of their bond orientational OPs, where those colored in blue have a highly ordered local structure (crystal-like) and those in red have low values of the OPs (liquid-like). Additional side views (*x*-*y* and *x*-*z*) of the same states are shown in Figure C2 and Figure C3 (Appendix). A supercooled liquid phase is depicted in Figures 3.4e (as well as Figure C2e and Figure C3e, Appendix). As we move from the right to the left along the MFEP in Figure 3.3, the cations rearrange to form a small patch where the cations and anions have crystal-like order (Figure 3.4d, Figure C2d and Figure C3d, Appendix). This state is located in the shoulder of the PMF shown in Figure 3.3. The ordered region of cations and anions grows slightly and the cations inside it

become more organized (as indicated by an increase in their OPs), and the system reaches the maximum of the PMF (Figure 3.4c, Figure C2c and Figure C3c, Appendix). If we arbitrarily define as crystalline those cations having OP > 3.5 (Figure 3.2b), we estimate that the critical nucleus has an average size of 3.6 nm at 58 K of supercooling; this size fluctuates between 3.2 and 4.0 nm, as determined from simulations using the SMCV as well as Markovian milestoning (see next sections). Moving further downhill along the MFEP (Figure 3.3), the ordered regions grow (Figure 3.4b, Figure C2b and Figure C3b, Appendix) until the system reaches the thermodynamically stable crystal phase (Figure 3.4a, Figure C2a and Figure C3a, Appendix). The anions follow the same qualitative behavior as the cations (bottom row of Figure 3.4, Figure C2 and Figure C3, Appendix).

3.4.2 Using Markovian milestoning with Voronoi tessellations to obtain the free energy involved in the homogeneous nucleation process

For this procedure, we took each of the replicas from the converged string from the SMCV for our system with 1372 ion pairs (Figure 3.3), and we associated a cell to each replica in the full OP space. A Voronoi tessellation is thus formed in the OP space, where the edges of the tessellation are identified as milestones. Here we had to interpolate additional replicas (to yield a total of 55) in order to ensure collection of statistically relevant results to numerically solve Equations (3.2)-(3.6). For visualization purposes, we used principal component analysis to project the initial configurations of these 55 replicas onto their first two principal components in OP space; these initial states are shown as black dots in Figure 3.5. These two principal components contain over 98% of the overall variance of the 125 OPs in our system, where the largest principal component (PC1 in Figure 3.5) accounts for about 95% and the second one (PC2 in Figure 3.5) contains about 3% of the overall variance. MD simulations are then performed for each of the 55 replicas, where each of them is restricted to remain within their

cells in the OP space. In Figure 3.5 we show values of the two principal components of the OPs from a few relevant configurations observed along the trajectories restricted in the Voronoi cells. The results shown in this figure indicate that replicas mainly remain within their own cells, although sometimes they visit neighboring cells for a brief period before returning to their original cells. This is a consequence of the soft restraining potentials used to confine each MD trajectories to remain within its own cell.[232] Here we emphasize that those states where replicas visit neighboring cells were not taken into account when collecting statistics. As shown by Ovchinnikov *et al*.,[229] our combination of methods yield correct results as long as the isocommitor surfaces are flat within the transition tube; this assumption is not rigorously correct in the regions of high curvature in the MFEP. Correlated re-crossings through the dividing surfaces between cells also become an issue in these high curvature regions. We attempted to minimize these issues by properly distributing the images along the MFEP, in particular by avoiding having a large density of images in regions of the MFEP that have high curvature (Figure 3.5). This way we also try to ensure that replicas only visit the cells of their nearest neighbors, if they manage to escape their original cells (replicas visiting cells of non-nearest neighbors can affect the accuracy of the MFPT calculations, see §3.3.5). At the same time, a proper distribution of images along the MFEP allows us to have good sampling of the transition probabilities [Eqns. (3.2)-(3.6)]. Another observation is that the initial replicas from the SMCV simulations (black dots in Figure 3.5) lie approximately in the center of the transition tube obtained by the simulation trajectory of each replica (approximately depicted by the different colors in Figure 3.5). In direct relation to this observation, the results shown in Figure 3.5 suggest that the region near the shoulder of the PMF and the free energy curves (Figures 3.3 and 3.6) has a transition tube that is narrower than the one observed near the peak of these two curves.

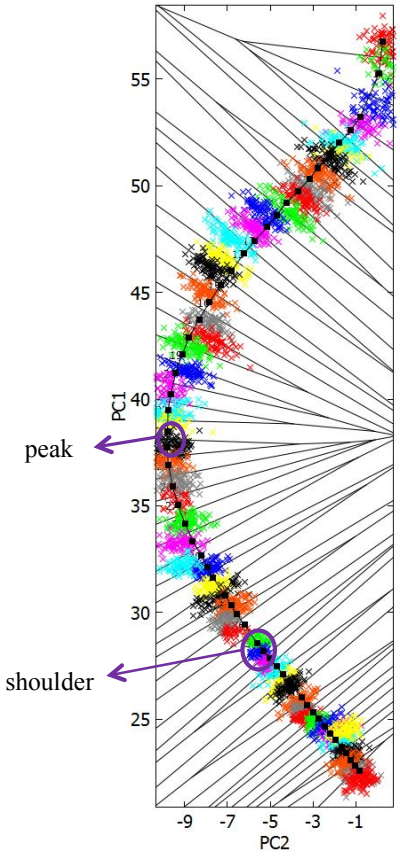

Figure 3.5 Voronoi tessellation of the MFEP in the first two principal components PC1 and PC2 in OP space. The black dots represent the initial configurations used in the Markovian milestoning simulations; these 55 initial configurations were obtained from the SMCV simulations as well as by interpolating additional replicas (see text). The different colors show a few snapshots of the OPs, as obtained from the simulations using Markovian milestoning with Voronoi tessellations. The regions corresponding to the peak and shoulder of the PMF and free energy curves (Figures. 3.3 and 3.6) are labled.

In our simulations using Markovian milestoning with Voronoi tessellations, for each replica we monitored the number of collisions made with the boundaries of neighboring cells, as well as the total number of transitions between different milestones. This data was then used together with Equations (3.2)-(3.6) to determine the free energy along a coordinate parameterizing the transition, as well as the MFPTs. In Figure 3.6 we show the free energy associated with the homogeneous nucleation of a crystal phase of [$dmim^+$][Cl^-] from its supercooled liquid at 340 K, as a function of the Voronoi cell number. In analogy to the PMF

from the SMCV shown in Figure 3.3, the free energy profile of Figure 3.6 also exhibits a shoulder between the supercooled liquid phase and the top of the free energy barrier. The free energy difference between the supercooled liquid and the configuration at the maximum of the curve is about 70 kcal/mol, and the difference in free energy between the crystal and liquid [dmim$^+$][Cl$^-$] is about 40 kcal/mol. These free energy differences are comparable to those determined for water[204] and urea[218] in recent simulation studies.

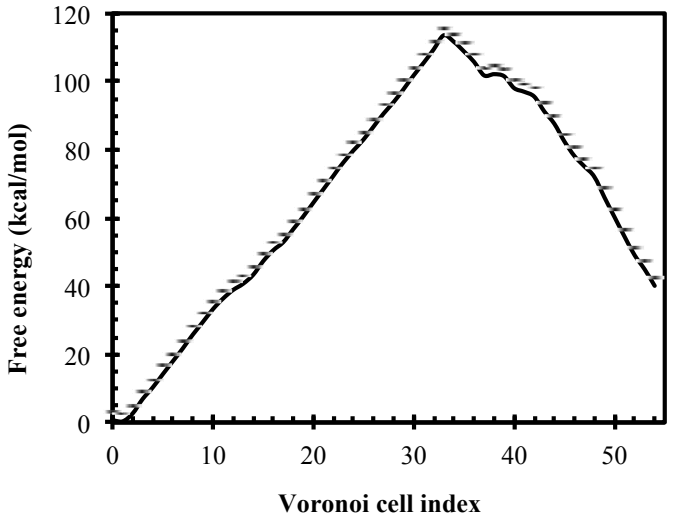

Figure 3.6 Free energy associated with the homogeneous nucleation of a crystal of [dmim$^+$][Cl$^-$] from its supercooled liquid phase at 340 K and 1 bar, as obtained from the simulations using Markovian milestoning with Voronoi tessellations. The left and right sides of the curve correspond to crystal and liquid states. These systems contain 1372 ion pairs.

As discussed by Ovchinnikov *et al.*,[229] it is important to emphasize that the PMF computed from the SMCV (Figure 3.3) is not the same as the free energy F_n computed from the procedure of Markovian milestoning with Voronoi tessellations (Figure 3.6). The converged string from the SMCV is used as input for the Markovian milestoning process, where less entropy is removed from the system by constraining each replica to be within its own cell (as compared to what happens in the SMCV, where the replicas are restricted to evolve in the

direction of the negative gradient of free energy in order parameter space; in consequence, in the SMCV we are effectively restraining 125 degrees of freedom, which removes more entropy). Furthermore, the MFEP determined from the SMCV corresponds to just a single pathway in the reactive flux tube, whereas the milestoning calculations integrates over many pathways, which captures more of the entropy in the path space. Therefore, a smaller free energy barrier is observed in F_n (Figure 3.6) than in the PMF (Figure 3.3). F_n is thus a more accurate representation of the free energy involved in the homogeneous nucleation process. Snapshots of configurations obtained from the Markovian milestoning simulation procedure look very similar to those obtained with the SMCV, which are depicted in Figures 3.4, C2 (Appendix) and C3 (Appendix).

3.4.3 Physical significance of the states in the PMF and free energy curves

We now discuss the physical significance of the configurations located at the shoulder (Figures 3.4d, C2d and C3d in Appendix) and overall maximum (Figures 3.4c, C2c and C3c in Appendix) of the PMF and free energy curves depicted in Figures 3.3 and 3.6. In particular, simulations of the homogeneous nucleation of benzene[242] using the same methods as in here lead to PMF and free energy curves that do not exhibit the shoulder observed here in Figures 3.3 and 3.6. Is this shoulder system-specific? If so, what physics cause this shoulder to appear in the free energy profiles associated with homogeneous nucleation? Furthermore, the ordered regions in Figures 3.4c, C2c and C3c in Appendix (configuration at the top of the free energy barrier) seem to percolate through the simulation box. This last observation is important, as one needs to be very wary of finite-size effects and periodic boundary conditions when studying nucleation using molecular simulation.[184, 255-257] One ambiguous issue here is the threshold value of OP when distinguishing between ‘ordered’ and ‘disordered’ regions. In our analysis we arbitrarily defined

as crystalline those cations with OP > 3.5, c.f. Figure 3.2b; however, if this threshold value is chosen to be slightly larger, e.g., OP = 4.0, it could be argued that the ordered regions in Figures 3.4c, C2c and C3c (Appendix) do not percolate throughout the simulation box (those snapshots have small regions where the cations and anions are in the ambiguous zone of what could be considered 'ordered' or 'disordered'). The brute-force way to overcome this issue is to perform simulations using larger systems, until it can be said unambiguously that the configuration at the top of the PMF and free energy curves have ordered regions that do not percolate through the simulation box. However, we do not know a priori how much we would need to increase our system size, and the computational costs could be beyond our current capabilities. We also note that our system with 1372 ion pairs is already much larger than those considered in previous studies of solid phases of ILs (up to 320 ion pairs, see, e.g.,[84, 247, 258]).

In order to understand the possible physical significance of the stationary states we found, and to illustrate the impact of finite size effects, we carried out calculations based on classical nucleation theory (CNT) in a model system. Based on those calculations, we argue that the configuration located at the shoulder of the PMF and free energy curves (Figures 3.4d, C2d and C3d in Appendix) is more representative of the bulk critical nucleus formed during homogeneous nucleation, rather than the configuration located at the top of the PMF and free energy curves (Figures 3.4c, C2c and C3c in Appendix). For our CNT calculations we considered a model system of finite total volume $V_t = 0.005$ (in arbitrary units). This total system size is not much larger than the volume of the critical nucleus for our particular CNT model system, which is likely the situation we have in our simulations with periodic boundary conditions. We then computed the free energy of a crystal nucleating within a liquid phase (blue curve in Figure 3.7), as well as the free energy of a liquid nucleating within a solid phase (red

curve in Figure 3.7). Here we assumed that the nuclei have spherical shape. These free energies are plotted in Figure 3.7 as a function of the total volume of liquid present in the system; therefore, the left and right sides of the *x*-axis in Figure 3.7 represent the pure solid and liquid phases, respectively. Our system is at a temperature below the melting point, and thus only the blue curve in Figure 3.7 goes through a maximum. The corresponding free energies as functions of the radii of the solid/liquid child phase are shown in Figures C4a and C4b in Appendix.

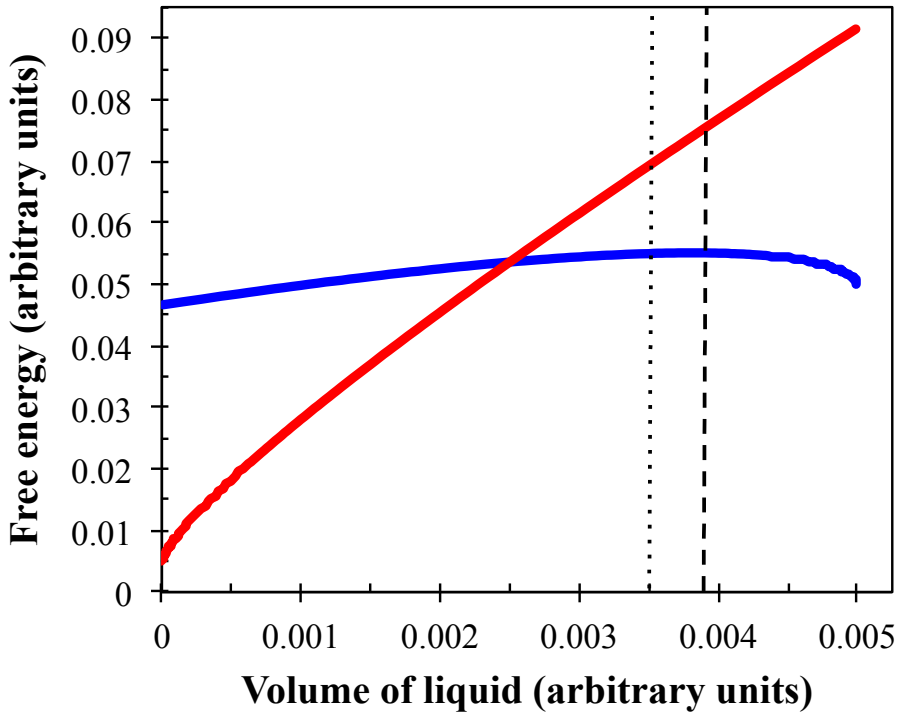

Figure 3.7 Classical nucleation theory (CNT) calculation of the free energy of a crystal nucleating within a liquid phase (blue curve), and of a liquid nucleating within a solid phase (red curve). The model system has a finite total volume V_t = 0.005 (in arbitrary units). The free energies are plotted as a function of the total volume of liquid present in the system; therefore, the left and right sides of the *x*-axis in this figure represent the pure solid and liquid phases, respectively. The model system is at a temperature below its melting point, and its total volume V_t is not much larger than the volume of the critical nucleus for our particular model system, which is the situation we have in our simulations with periodic boundary conditions. The dashed line indicates the approximate location of the maximum in the blue curve, and the dotted line indicates the approximate point at which the crystal nucleus is large enough to touch its periodic images, and thus the system jumps from the blue curve (crystal nucleating within a liquid phase) to the red curve (liquid nucleating within a solid phase).

As in our simulations we are nucleating the solid within the liquid phase under supercooled conditions, we start at the right side of the *x*-axis in Figure 3.7 following the blue curve and moving left, eventually reaching the maximum in the blue curve (dashed line in Figure 3.7). As the crystal grows and the volume of liquid in such a system continues to decrease, the system will reach a point where the crystal becomes large enough so that its dimensions are comparable to the shortest of the *x*, *y* or *z* lengths of the system, and therefore the crystal nucleus can "touch" its periodic images in that particular direction (here we note that we did not truncate the nucleus when it reaches one of the cell boundaries). Further crystal growths beyond this point in such a finite-size system will lead to a situation where the curvature of the solid-liquid interface will change sign, and we then have a liquid nucleus within a solid phase; in this situation, the system will transition from the blue curve in Figure 3.7 to the red curve. We therefore argue that the configurations shown in Figures 3.4c, C2c and C3c in Appendix (as the ordered regions seem to percolate through the simulation box) are more representative of a liquid nucleus inside a crystal phase (i.e., after the system moves from the blue curve to the red curve in Figure 3.7). Based on this argument, we indicate that the configuration located at the shoulder of the PMF and free energy curves (Figure 3.4d, Figures C2d and C3d in Appendix) are more representative of the critical nucleus formed during homogeneous nucleation (i.e., the maximum in the blue curve in Figures 3.3 and C4a in Appendix). The point at which the system jumps between the blue and red curves in Figure 3.7 depends on two main parameters: (1) the actual values of the free energies and surface tensions in our CNT model (those values were chosen so that the curves shown in Figure 3.7 qualitatively resemble the PMF and free energy curves shown in Figures 3.3 and 3.6); and (2) the total volume and specific dimensions of our model system. If our CNT model system is chosen to be approximately cubic, the jump between the

blue and red curves in Figure 3.7 will happen farther to the left (i.e., at smaller values of volume of liquid). However, if the system is elongated rather than cubic, the jump will take place at larger values of volume of liquid, because the crystal nucleus does not need to grow too much in one of the directions before it is able to touch its periodic images. Our [$dmim^+$][Cl^-] system with 1372 ion pairs forms a monoclinic crystal with characteristic dimensions of about 6.5 nm × 5.3 nm × 7.5 nm. Using a box with the same shape, with the parameters chosen for the CNT model, the jump would happen at a liquid volume of about 0.0035 (dotted line in Figure 3.7), which is just slightly to the left of the maximum of the blue curve.

This simple model suggests that, for this particular system, as we move from right to left in Figure 3.7 we would first see a maximum in the blue curve (i.e., the crystal forming a critical nucleus in the supercooled liquid phase). The system continues to follow the blue curve and goes through a few states where the free energy only has a slight variation (see also the few states immediately at the left of the shoulder in Figures 3.3 and 3.6), but then the free energy increases sharply as the crystal nucleus is able to touch its periodic images (and now we have a liquid nucleus within a solid phase; this point lays in the red curve). As the volume of liquid keeps diminishing, the free energy decreases continuously until the whole system crystalizes. We argue that in a bigger simulation box the shoulder would not be present, as in this case the crystal nucleus can grow bigger before it can touch its periodic images. In such a situation, the maximum in the blue curve in Figure 3.7 would be closer to the point where the two curves intersect (and therefore a much smaller change in free energy between the blue and red curves would occur in this case). This situation is probably representative of what was observed for the homogeneous nucleation of benzene,[242] where the simulation box was more similar to a cube than the one used for [$dmim^+$][Cl^-] (in addition the molecular interactions and properties such as

the surface tension are significantly different). Under this argument, the maximum in the blue curve (which would correspond to the configuration depicted in Figures. 3.4d, C2d and C3d in Appendix, located at the shoulder of the PMF and free energy curves of Figures. 3.3 and 3.6) is more representative of the critical nucleus formed during homogeneous nucleation, rather than the configuration located at the top of the free energy barrier (that depicted in Figures 3.4c, C2c and C3c in Appendix).

From the free energy curve of Figure 3.6, the free energy differences between the supercooled liquid and the configurations at the shoulder and at the peak of this curve are about 60 and 70 kcal/mol respectively; based on our interpretation, the first of these two quantities is a more accurate estimate of the free energy barrier for homogeneous nucleation of crystals of $[dmim^+][Cl^-]$ at 1 bar and 340 K (a supercooling of about 58 K).

3.4.4 Comparing the PMF results with that for a larger system

In order to test whether the interpretation of the results described in the section above is correct, we ran SMCV simulations for a larger system containing 2268 ion pairs in Chapter 4 (forming a monoclinic crystal with characteristic dimensions 8.3 nm × 5.3 nm × 9.7 nm). The PMF results for such a system are presented in Figure 3.8, and are directly compared against those previously shown in Figure 3.3 (obtained for the system with 1372 ion pairs, which forms a crystal of dimensions 6.5 nm × 5.3 nm × 7.5 nm). The total number of OPs changes as we vary the size of our systems, and thus the arclength varies between the two systems considered (remember the arclength represents the distance along the path, if we keep the same distance in OP space between replicas). Therefore, the results shown in Figure 3.8 are renormalized using a parameter α, equal to the ratio of the arclength to the maximum arclength found for the systems with 2268 and 1372 ion pairs.

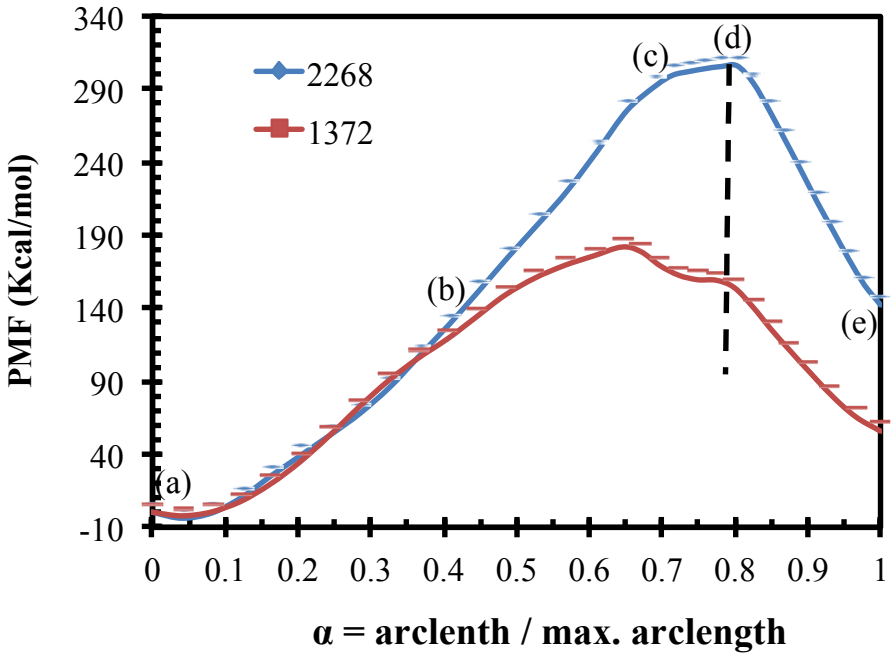

Figure 3.8 Comparison of SMCV results for the PMF associated with the MFEP for homogeneous nucleation of a crystal phase of [dmim$^+$][Cl$^-$] from its supercooled liquid phase at 340 K and 1 bar. The blue and red curves correspond to results obtained for systems containing 2268 and 1372 ion pairs. The results are renormalized using a parameter α, equal to the ratio of the arclength to the maximum arclength found for each system. The dashed line is used to emphasize that the location of the PMF peak in the larger system is approximately the same as the location of the shoulder in the smaller system. Simulation snapshots of states labeled in the blue curve are depicted in Figures 4.4, 4.5 and 4.6 in Chapter 4.

We first note that important differences are observed in the PMF curves for both systems. The PMF difference between the configuration at the peak and that in the liquid state is about 164 kcal/mol for the system with 2268 ion pairs; this PMF difference is about 126 kcal/mol for the smaller system. This discrepancy is due to accumulation of integration error as we change the system size (recall the PMF is the line integral of the restraint force along the path in the multidimensional OP space). Interestingly, the PMF curve for the larger system does not exhibit the shoulder observed in the curve for the smaller system. Furthermore, the location of the PMF

peak in the larger system is approximately the same as the location of the shoulder in the smaller system (dashed line in Figure 3.8). Side views of representative simulation snapshots of several relevant states along the MFEP obtained for the system with 2268 ion pairs are shown in Figures 4.4, 4.5 and 4.6 (Chapter 4). The critical nucleus size observed for the larger system (Figures 4.4d, 4.5d and 4.6d in Chapter 4) is very similar to the crystallite dimensions noted for the configuration at the shoulder of the PMF and free energy results of the system with 1372 ion pairs (Figures 3.4d, C2d and C3d in Appendix). Overall, our SMCV results for the system with 2268 ion pairs strongly support our interpretation and analysis (§4.3.3) of the results obtained for our system with 1372 ion pairs, i.e., that the configuration located at the shoulder of the PMF and free energy curves for such a system (depicted in Figures 3.4d, C2d and C3d in Appendix) is representative of the critical nucleus formed during the homogeneous nucleation process.

3.4.5 Using Markovian milestoning with Voronoi tessellations to compute mean first passage times (MFPTs) involved in the homogeneous nucleation process

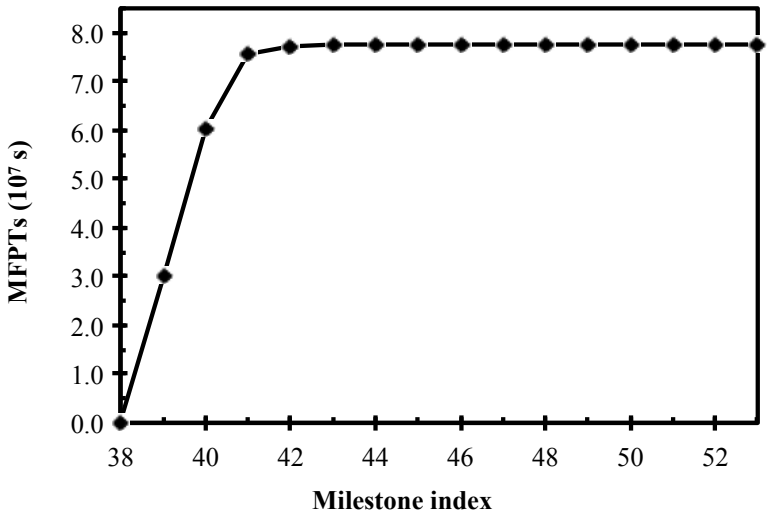

Figure 3.9 Mean first passage times (MFPTs) from the milestone $B_{i+1} \cap B_i$ for i = 53, 52, … 40 to the milestones at the shoulder of the free energy curve, $B_{39} \cap B_{38}$. These systems contain 1372 ion pairs.

The MFPTs involved in the homogeneous nucleation process were estimated using Markovian milestoning with Voronoi tessellations. To compute the MFPTs involved in the homogeneous nucleation process, we set the configurations to the left of the shoulder of the free energy (Figure 3.6) as the target configurations. The results and discussion presented in §3.4.3 and §3.4.4 give us confidence that the rate calculated using the shoulder configuration as the target milestone is physically meaningful for our system with 1372 ion pairs. We then estimated the time needed for each of the replicas to reach this state (defined as those configurations in Voronoi cells 38 and 39). The MFPTs from Voronoi cell (milestone) $B_{i+1} \cap B_i$ (where i = 53, 52, … 39) to the milestone $B_{39} \cap B_{38}$ are shown in Figure 3.9. Here the rate matrix can be determined from all statistical data gathered during these simulations (i.e., considering all fluxes between adjacent and nonadjacent images), or by considering only fluxes between adjacent milestones (for a detailed discussion, see Appendix B in the study of Ovchinnikov *et al.*[229]) The results shown in Figure 3.9 were determined by considering only fluxes between adjacent cells (fluxes between non-adjacent cells represent about 10% of the total number of fluxes). We repeated our calculations considering all fluxes, and found that the maximum difference in MFPTs is only of about 6%; these results suggest that the contribution of non-adjacent isocommittor surfaces[229] to the kinetics of the nucleation process can be ignored. The MFPTs presented in Figure 3.9 show that the MFPTs to the configurations at the shoulder of the free energy curve of Figure 3.9 are approximately constant for milestones $B_{i+1} \cap B_i$ with i = 53, 52, …, 41. The results shown in Figure 3.9 can give information about the nucleation rate (i.e., the process where the critical nucleus is formed within a supercooled liquid phase). Nucleation rates are typically reported with units of [cm^{-3} s^{-1}];[204, 210] however, in Figure 3.9, the MFPTs have

units of [s]. Therefore, we took the data reported in Figure 3.9, multiplied it by the volume of our simulation box and took the inverse of all the resulting data. After doing those calculations, a simulated nucleation rate of 5.0×10^{10} [cm^{-3} s^{-1}] was obtained for our system, which is at a supercooling of 58 K. To the best of our knowledge, no experimental data has been reported for the homogeneous nucleation rate of crystals of [$dmim^+$][Cl^-]. However, our computed nucleation rate is in reasonable agreement with experimental and simulation rates for homogeneous nucleation of ice at a supercooling of about 40 K, which are on the order of 10^{10} [cm^{-3} s^{-1}].[204, 259-260]

3.5 Conclusions

Molecular simulation and calculations based on classical nucleation theory (CNT) were used to study the homogeneous nucleation of crystals of a typical ionic liquid (IL), [$dmim^+$][Cl^-], from its supercooled liquid phase in the bulk (P = 1 bar, T = 340 K; a supercooling of 58 K). Our simulations provided insights about the free energy barrier, the size of the critical nucleus and the rate of nucleation. The string method in collective variables (SMCV)[229-230] was first used to make a string of replicas of the IL relax in the direction of the negative gradient of the free energy, in order to sketch a minimum free energy path (MFEP) connecting the supercooled liquid and the monoclinic crystal phase. The converged string of states from the SMCV was then used as input to a series of MD simulations using Markovian milestoning with Voronoi tessellations.[229, 231-233] This method yields the free energy and the mean first passage times (MFPTs) involved in the homogeneous nucleation process. These methods were combined with the order parameters (OPs) for molecular crystals developed by Santiso and Trout,[241] which allowed us to measure local order in nm-sized regions and distinguish between crystal-like and amorphous (liquid-like) groups of ions. Our molecular simulation results were rationalized using

CNT-based calculations, which helped us in discussing the physical significance of the configurations located along the MFEP determined for the homogeneous nucleation process; SMCV simulations using a larger system corroborate our interpretations. Our results indicate that, at a supercooling of 58 K, the subcooled liquid has to overcome a free energy barrier of 60 kcal/mol before it reaches the thermodynamically stable crystal phase. We find that during the homogeneous nucleation process, the system forms a critical nucleus with a size of about 3.6 nm. A simulated homogeneous nucleation rate of 5.0×10^{10} [cm^{-3} s^{-1}] was obtained for our system at 58 K of supercooling, which is in reasonable agreement with experimental and simulation rates for homogeneous nucleation of ice at a supercooling of 40 K.[204, 259-260] This study represents our first step in a series of studies aimed at understanding the nucleation and growth of crystals of organic salts near surfaces and inside nanopores.

Chapter 4 Homogeneous Nucleation of [dmim$^+$][Cl$^-$] from its Supercooled Liquid Phase: A Molecular Simulation study[‡]

4.1 Introduction

Room-temperature ionic liquids (ILs) have attracted significant attention as designer solvents, electrolytes, and other applications mostly involving liquid phases of the ILs. Very recently, Warner *et al*.[45-49, 64, 173] developed IL-based nanomaterials (dubbed GUMBOS, for Group of Uniform Materials Based on Organic Salts) where these compounds are in the solid state. These IL-based materials hold enormous promise, as they have the highly tunable properties of ILs[1-2] and can be prepared *via* simple procedures,[45-49, 64, 173] possibly impacting fields as diverse as optoelectronics, photovoltaics, separations, analytical chemistry and biomedicine. 1D-nanomaterials such as nanorods and nanowires were also synthesized[64] by introducing the ILs inside hard templates with cylindrical nanopores, e.g., multi-walled carbon nanotubes and anodic alumina membranes; shape anisotropy can lead to further variations in interesting properties of these nanomaterials (fluorescence, magnetic). On the other hand, ILs are also immobilized in nanoporous solids (carbon nanotubes, silica, cellulose, polymers, etc.) during the synthesis of ionogels.[63] These hybrid materials have potential applications in lithium batteries, fuel cells and solar cells, and in catalysis and biocatalysis, drug delivery and optical sensing devices.[63] A rational design of IL-based nanomaterials and ionogels requires a fundamental understanding of the solidification, as well as the nucleation and growth of crystals of ILs in contact with surfaces and inside nanopores.

[‡] Contents of this chapter were published in the following article: He, X.; Shen, Y.; Hung, F. R.; Santiso, E. E. Homogeneous nucleation of [dmim$^+$][Cl$^-$] from its supercooled liquid phase: A molecular simulation study. *Molecular modeling and simulation: Applications and perspectives* (Proceedings of the FOMMS 2015 Conference) **2015** (submitted)

As a starting point for our studies in this area, here we focus on modeling the homogeneous nucleation of a simple IL, 1,3-dimethylimidazolium chloride, [$dmim^+$][Cl^-], from its supercooled liquid phase in the bulk. This IL has been extensively studied in previous simulation reports.[26, 41, 224-228, 261-262] However, nucleation is an extremely challenging problem.[184-191] The initial stage of nucleation typically involve a few molecules or atoms, which makes it difficult to design experiments to study nucleation at the molecular level. Molecular dynamics (MD) simulations of nucleation are also very challenging, as nucleation is a rare event. Previous studies of homogeneous nucleation of systems of particles (hard-sphere, Lennard-Jones, etc.),[67, 192-200] water,[201-209] and other substances (e.g., NaCl, silicon, benzene, n-octane, urea, copper, aluminum, etc.)[210-220, 263] using rare event methods have provided important insights on these phenomena in those systems. However, these methods might have limitations when studying the nucleation of ILs, which can have very slow dynamics and therefore the transition paths might take a prohibitively long time to commit to any of the stable states. Here we have combined the string method in collective variables (SMCV)[264] with Markovian Milestoning with Voronoi tessellations,[232, 265-266] to study the homogeneous nucleation of [$dmim^+$][Cl^-]. This combination of methods has been used before to study conformational changes in biomolecules,[232, 237, 264, 267] In the SMCV, a string of replicas connecting the liquid with the crystal phase evolves guided by the negative gradient of the free energy with respect to some collective variables (or order parameters, OPs, characterizing the transition), until they converge into a minimum free energy path (MFEP). This path represents the region where the transition has the maximum probability to take place. This converged string is then used as input to our second method, Markovian milestoning with Voronoi tessellations, which yields the free energy along the path, as well as the mean first passage times (MFPTs) in the transition studied. In

association with these methods we have used the OPs for molecular crystals recently developed by Santiso and Trout.[268] These OPs can distinguish between different crystal polymorphs and liquid phases, and detect crystal ordering in nm-size regions.

We note here that we have used the same methods and OPs in previous studies of the homogeneous nucleation of benzene[242] and the same IL studied here, [dmim$^+$][Cl$^-$].[269] In the latter report we used a system consisting of 1372 ion pairs, and interpreted our results using calculations based on classical nucleation theory, which also helped us address possible finite-size effects in this system. Our interpretations were corroborated by SMCV results obtained using a larger system containing 2268 ion pairs. [269] Here in this paper we present a complete account and discussion of our results obtained for this larger system, using both the SMCV and Markovian milestoning with Voronoi tessellations, which completes the work we have presented before.[269] The rest of the paper is structured as follows. In the next section, we provide details of our systems and methods (OPs used, SMCV and Markovian milestoning with Voronoi tessellations). Section 4.3 contains our main results and discussion, and our main findings are summarized in section 4.4.

4.2 Simulation details

4.2.1 Models

The monoclinic crystal structure of [dmim$^+$][Cl$^-$] was obtained from the Cambridge Crystallographic Data Centre.[243-244] The classical non-polarizable force field developed by Lopes *et al*.[84-88] was used to model the IL, mainly because it can reproduce the experimental crystal structure of [dmim$^+$][Cl$^-$].[84] Furthermore, the density of the liquid phase and the melting point as determined from simulations using this model were found to be in good agreement with

experimental values.[145] Our system contained 2268 ion pairs, which can form a monoclinic crystal of characteristic dimensions 8.3 nm × 5.3 nm × 9.7 nm. All MD simulations were performed using a modified version of the NAMD software[248] that included implementations of the OPs, the SMCV and Markovian milestoning with Voronoi tessellations (see below) in C++ libraries. All the simulations were performed in the *NPT* ensemble with P = 1 bar and T = 340 K (a supercooling of 58 K). A Langevin thermostat with a damping coefficient of 25 ps^{-1} was used to control the temperature, and the Nosé-Hoover Langevin piston with a damping time of 50 fs was used as the barostat. Periodic boundary conditions were applied in all directions. Lennard-Jones and electrostatic interactions were cutoff at 10 Å and 12 Å; particle mesh Ewald (PME)[249] was used to handle the latter type of interactions. Hydrogen bond lengths were constrained with the LINCS algorithm, and a time step of 0.5 fs was used in our simulation runs.[250] Additional details of our model systems can be found elsewhere. [269]

4.2.2 Order parameters (OPs)

The OPs developed by Santiso and Trout[268] are extracted from a generalized pair distribution function. All OPs used in this study were based on [$dmim^+$]; no particular OPs were defined for [Cl^-]. In Figure 4.1 two ion pairs are shown, where the absolute orientation of each cation is given by the vectors $\mathbf{q}_1$ and $\mathbf{q}_2$, which are normal to the imidazolium ring of each cation. The distance OP provides quantification for the various center of mass (COM) distances between the cations. The bond orientation OP measures the orientation of bonds joining the center-of-mass of the cations, while the relative orientation OP measures the orientation of one cation with respect to another one.[268-269] All the OPs are defined per cation and per peak in the pair distribution function, which leads to an extremely large number of OPs. To reduce the total number of OPs, we first sum over peaks in the pair distribution function, and then calculate local

averages over the cations present in a given subcell of the simulation box. In our system, the simulation box was divided into 6 × 5 × 6 subcells, giving a total of 180 OPs of each type (distance, bond orientation and relative orientation). In Figure 4.2 we present the number frequency of distance, bond orientation and relative orientation OPs for the liquid and crystal phases of [dmim$^+$][Cl$^-$] at 340 K. The frequency is averaged over 400 configurations (as obtained from short, 0.4 ns MD simulation of the liquid and solid phases in the *NPT* ensemble). These results indicate that any of the OPs can serve as a good metric to distinguish between crystal and liquid phases, even in nm-sized regions. Here we chose to work with the bond orientation OPs, although we also monitored the distance and the relative orientation OPs.

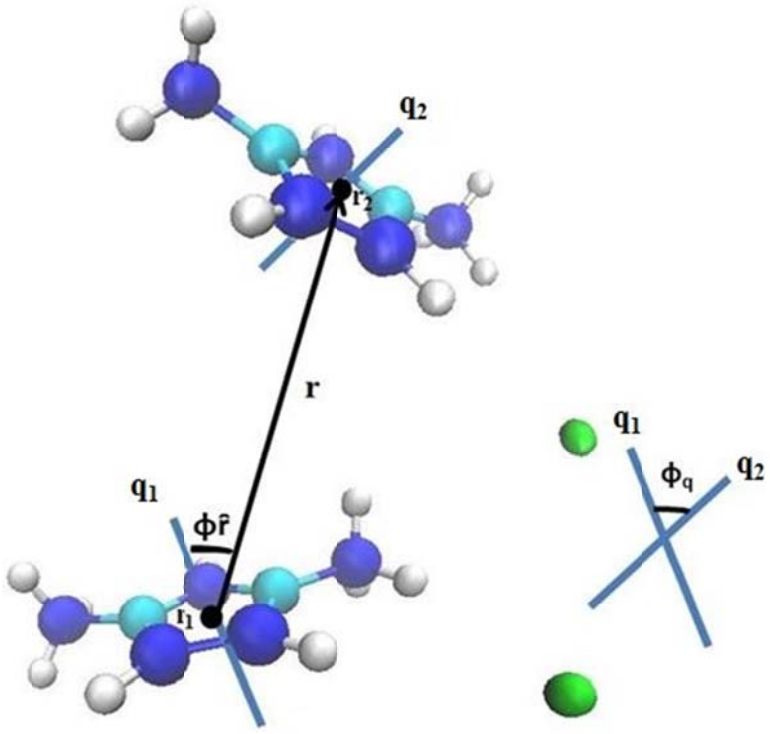

Figure 4.1 Variables used in the construction of OPs. The vector normal to the plane of the imidazolium ring of [dmim$^+$] gives the absolute orientation of each of the two cations. The distance OP is based on **r**, which joins the center of mass (COM) of the two cations. The angle formed by the vectors **r** and $\mathbf{q_1}$ is used for the bond orientation $\phi_{\hat{\mathbf{r}}}$, whereas the angle formed by the vectors $\mathbf{q}_1$ and $\mathbf{q}_2$ is used for the relative orientation ϕ_q.

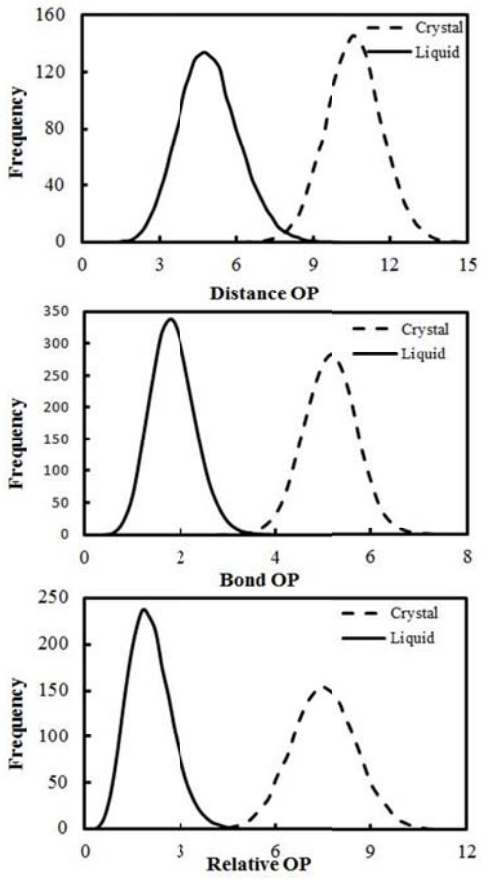

Figure 4.2 The number frequency of distance, bond orientation and relative orientation OPs for liquid and solid IL, as obtained from 400 liquid-like and 400 crystal-like configurations of the IL.

4.2.3 String method in collective variables (SMCV)

The SMCV[264, 267] was used to sketch a MFEP for the homogeneous nucleation of [dmim$^+$][Cl$^-$] from its supercooled liquid. An initial string consisting of 32 replicas was prepared by collecting a number of intermediate states from the simulated melting of a crystal of the IL at 800 K. Each replica in this string contains 180 OPs that characterize its local structure. An extended Hamiltonian is then established for each replica, by including a set of harmonic springs that keep each replica's OPs close to their 'target' values. Using this extended Hamiltonian, we then run short (0.2 ns) MD simulations in the *NPT* ensemble for each image, in order to determine the mean force required to maintain each image close to the target OP values (here the

mean force is the negative gradient of the free energy with respect to the OPs). The string replicas then evolve guided by the mean force. The string can also be reparametrized by interpolating more images, and by redistributing the replicas to prevent them from clustering near the stable states. The steps described above are repeated until the potential mean force (PMF) converges; here the PMF is the line integral of the restraint force along the path in the multi-dimensional OP space. Additional details about the SMCV and its implementation are presented elsewhere.[217, 264, 267, 269]

4.2.4 Markovian milestoning with Voronoi tessellations

The MFEP computed from the SMCV is an *n*-dimensional function (where *n* is equal to the 180 OPs), determined by effectively restraining 180 degrees of freedom as the replicas in the SMCV evolve following the negative gradient of the free energy with respect to the OPs. The MFEP thus only represents a single pathway in the transition tube. However, this tube can be mapped into a single free energy curve as a function of a reaction coordinate, by using the converged string from the SMCV as input to simulations using Markovian milestoning with Voronoi tessellations.[232, 265-267] This procedure can also yield information about the rate of nucleation. In this method, we associate a cell in OP space to each replica from the converged SMCV string, forming a tessellation in the OP space. By construction,[232, 267] the edges of the tessellations are approximate isocommittor surfaces, and thus are used as milestones in our procedure. We then perform MD simulations where each replica is forced to remain within its own cell by using soft walls (planar half-pseudoharmonic restraints).[232] In these simulations we monitor the number of collisions each trajectory does with the milestones (edges of the Voronoi tessellation). At steady state, if $N_{n,m}$ represents the number of collisions that the MD trajectory in

cell B_n experiences with the boundary of cell B_m during the simulation time t_n, the rate of escape from tessellation cell B_n to cell B_m can be estimated as:

$$v_{n,m} = \frac{N_{n,m}}{t_n} \tag{4.1}$$

The probability π_n of finding the system in cell B_n can then be calculated from the following equations:

$$\sum_{\substack{n=1 \\ n \neq m}}^{N} \pi_n v_{n,m} = \sum_{\substack{n=1 \\ n \neq m}}^{N} \pi_m v_{m,n} \tag{4.2}$$

$$\sum_{n=1}^{N} \pi_n = 1 \tag{4.3}$$

The free energy curve F_n can be calculated as a function of cell n as follows:

$$F_n = -k_B T \ln \pi_n \tag{4.4}$$

In turn, the MFPTs can be also computed from the Voronoi milestoning procedure using the following equations:

$$\sum_{b \neq b^*} k_{a,\,b} t_{b,\,b^*} = -1 \quad , \quad a \neq b^* \tag{4.5}$$

$$k_{a,\,b} = \frac{\sum_{n=0}^{N} \pi_n N_{a,\,b}^n / t_n}{\sum_{n=0}^{N} \pi_n t_a^n / t_n} \tag{4.6}$$

Where $t_{b,b*}$ is the MFPT to milestone b^* from other milestones in the system (where $b \neq b^*$). $k_{a,b}$ is the rate of instantaneous transition from milestone a to milestone b; $N_{a,b}{}^n$ is the total number of transitions from milestone a to milestone b during the simulation confined to cell B_n, and $t_a{}^n$ is

total time during which *a* was the most recent milestone visited by the system. We used the arbitrary precision floating-point library implemented in the Sage software[254] to solve the equations above, as the values of $k_{a,b}$ could have variations of up to 6 orders of magnitude. Additional details of these simulations are provided elsewhere.[232, 242, 267, 269]

4.3 Results and discussion

4.3.1 Determination of the Minimum free energy path (MFEP) from the SMCV

The converged PMF (see §4.2.3) as determined from our simulations with the SMCV is presented in Figure 4.3; here the arclength (of the bond orientation OPs, in this case) represents the distance along the multidimensional nucleation path. A difference of about 141 kcal/mol is observed between the crystal phase and the supercooled liquid phase at about 58 K of supercooling, with a PMF barrier of about 163 kcal/mol between the supercooled liquid and the state at the top of the PMF profile.

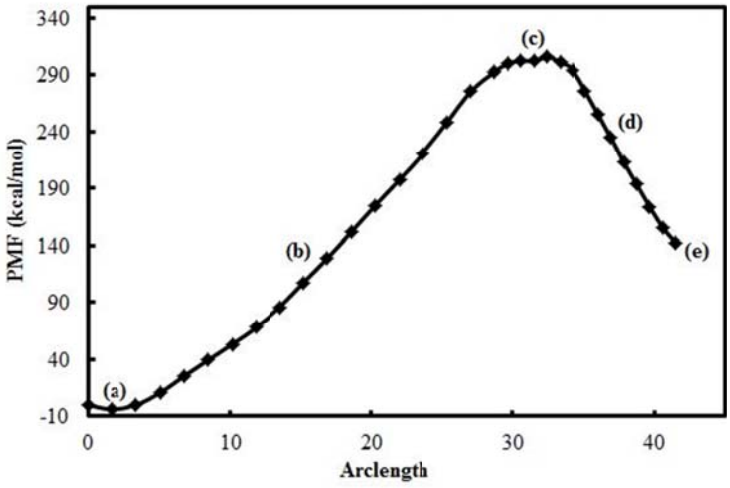

Figure 4.3 The PMF associated with the MFEP for homogeneous nucleation of a crystal phase of [dmim$^+$][Cl$^-$] from its supercooled liquid phase at 340 K and 1 bar. The left and right sides of the curve correspond to crystal and liquid states. Simulation snapshots of states labeled here are shown in Figure 4.4.

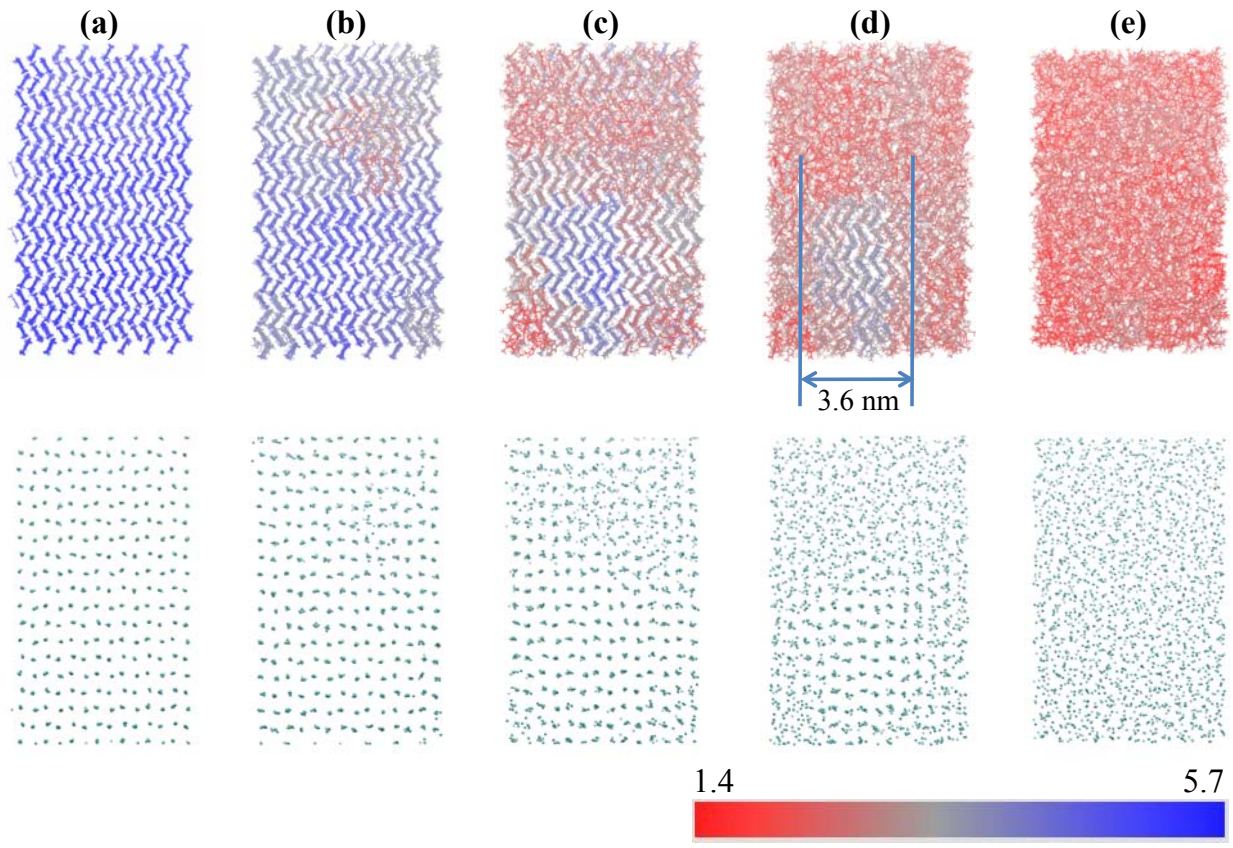

Figure 4.4 *y*-*z* side views of simulation snapshots of states labeled along the MFEP shown in Figure 4.3. The cations (top row) are color-coded according to the value of their bond orientation OPs (red = crystal-like, blue = liquid-like). The anions are shown on bottom row and are not color-coded.

In Figure 4.4 we show *y*-*z* side views of representative simulation snapshots of several relevant states along the MFEP mapped in Figure 4.3 (*x*-*y* views are shown in Figure 4.5 and *x*-*z* views are shown in Figure 4.6). As we move left from the supercooled liquid (state e) at the right of the PMF curve shown in Figure 4.3, the cations and anions start to rearrange (state d) until we reach the top of the barrier (state c), where the ions form a critical nucleus exhibiting crystal-like order. If we arbitrarily define the cations with OPs > 3.5 (Figure 4.2) as crystalline, we estimate that the critical nucleus has a size of ~3.6 nm at this degree of supercooling. However, from our SMCV and Voronoi milestoning simulations (see below) we observed that the size of this

nucleus fluctuates between 3.0 and 4.0 nm. Moving further left (and now downhill) along the MFEP mapped in Figure 4.3, the crystal-like region grows (state b) until the system crystallizes completely (state a).

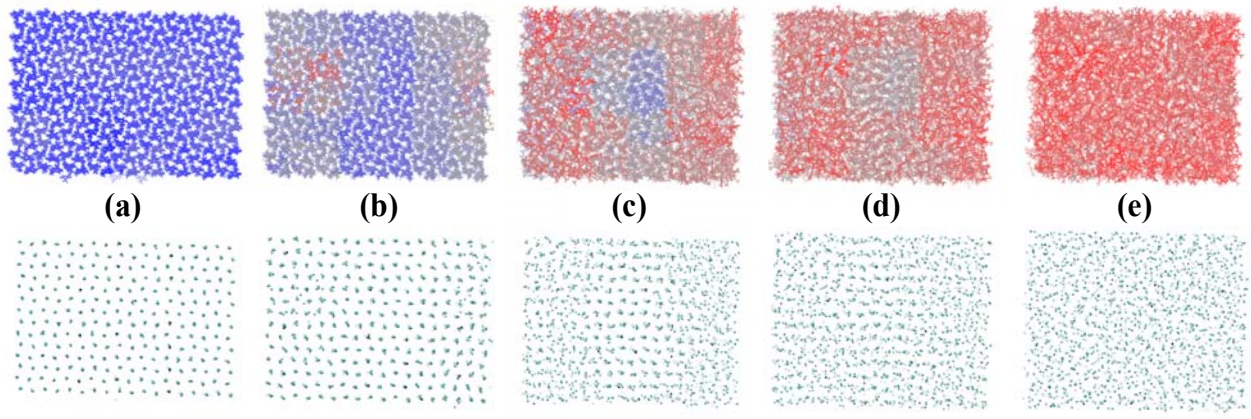

Figure 4.5 Side views (*x*-*y*) of representative simulation snapshots of relevant states along the MFEP shown in Figure 4.3. Cations are color-coded using the same criteria as in Figure 4.4.

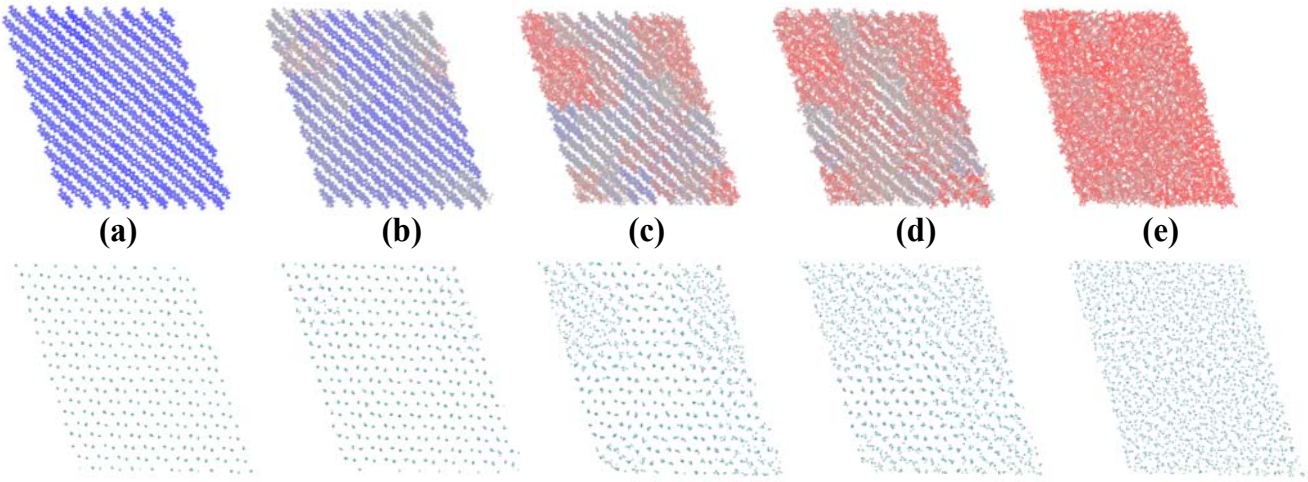

Figure 4.6 Side views (*x*-*z*) of representative simulation snapshots of relevant states along the MFEP shown in Figure 4.3. Cations are color-coded using the same criteria as in Figure 4.4.

4.3.2 Free energy and mean first passage times (MFPTs) from Markovian milestoning with Voronoi tessellations

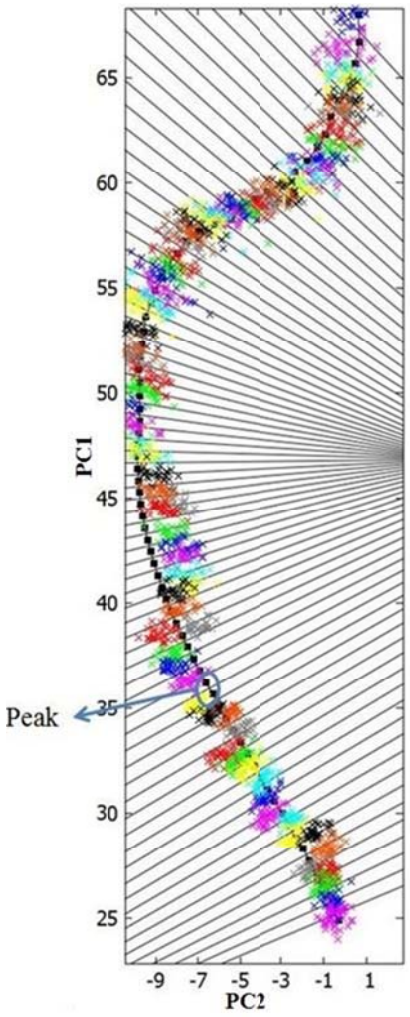

Figure 4.7 Voronoi tessellation of the MFEP as projected onto the first two principal components PC1 and PC2 in OP space. The black dots represent the initial configurations (converged SMCV string plus interpolation of additional replicas) used in the Markovian milestoning simulations. Projections of representative configurations obtained from the milestoning procedure are also shown using different colors. The region corresponding to the peak of the PMF and free energy curves (Figures 4.3 and 4.8) is labeled.

The 32 replicas from the converged SMCV string were used as the starting point for our series of simulations with Markovian milestoning. Here we had to interpolate additional replicas (to reach a total of 74) as to ensure collection of enough statistics for the numerical solution of equations (4.1-4.6). As direct analysis of the data is difficult due to the 180-dimensionality of the

OP space, we used principal component analysis to determine the subspace of the OP space that contains most of the variance along the solidification path. In Figure 4.7 we show the projections onto the first two principal components of the initial configurations (converged SMCV string, black dots), as well as some representative configurations (different colors) observed throughout our Markovian milestoning simulations. The results shown in Figure 4.7 suggest that the images mainly remain within their own cells, although they occasionally wander into neighboring cells for a brief period; this is a consequence of using soft walls[232] to maintain each MD trajectory within its own cell. One important challenge is to properly distribute the images along the MFEP, in order to accumulate good statistics for the numerical solution of equations (4.1-4.6). At the same time, we strived to not place too many images in MFEP regions with high curvature; this way, replicas mostly visit adjacent cells when they leave their own cells, and we avoid transitions between non-adjacent cells as much as possible (as discussed before,[267] replicas visiting cells of non-adjacent neighbors can affect the accuracy in the calculations of the free energy and the MFPTs).

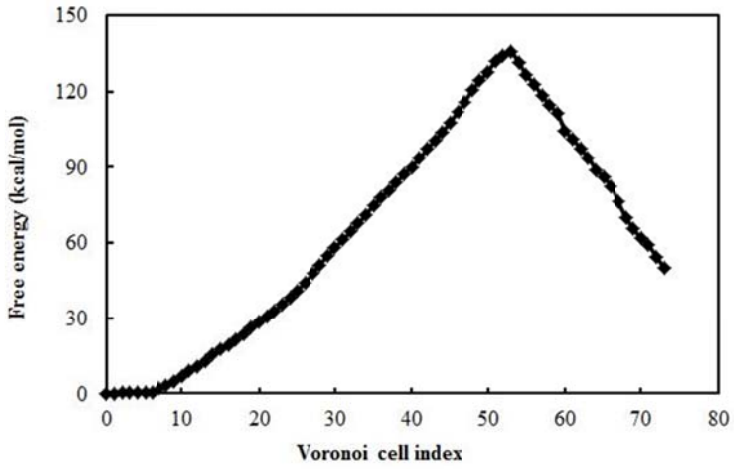

Figure 4.8 Free energy involved in the homogeneous nucleation of [dmim$^+$][Cl$^-$] from its supercooled liquid phase at 340 K and 1 bar, as obtained from the milestoning procedure. The left and right sides of the curve correspond to crystal and liquid states.

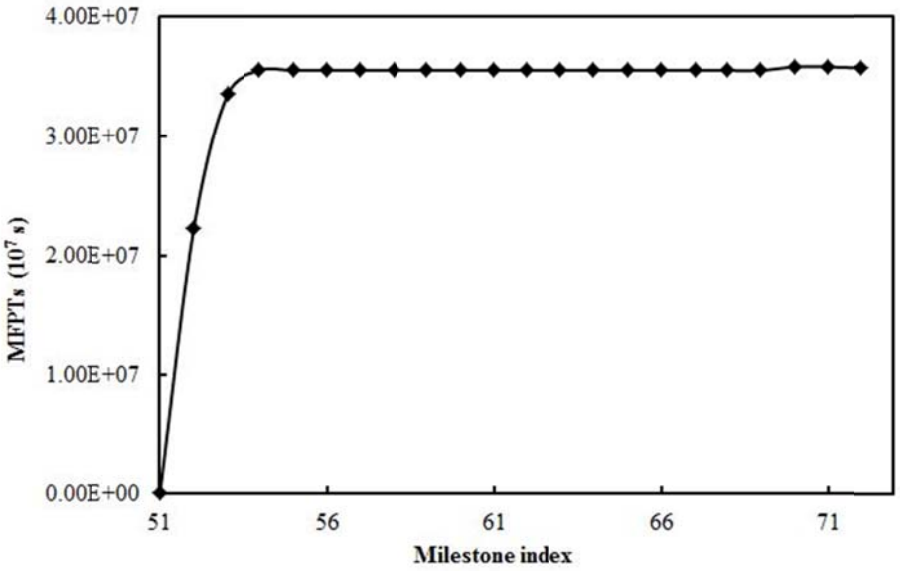

Figure 4.9 Mean first passage times (MFPTs) from the milestone $B_{i+1} \cap B_i$ for i = 72, 71, … 52 to the milestones at the shoulder of the free energy curve, $B_{52} \cap B_{51}$.

In Figure 4.8 we show the free energy along the MFEP as a function of the Voronoi cell number, as determined from the Voronoi milestoning simulations. These results indicate that the difference in free energy between the crystal and liquid phases of [$dmim^+$][Cl^-] at 58 K of supercooling is about 50 kcal/mol, and the free energy barrier between the liquid and the configuration at the top of the curve is about 85 kcal/mol. These free energy differences are comparable to those determined for water[204] and urea[218] in recent simulation studies of homogeneous nucleation. The free energy curve (Figure 4.8) and the PMF curve (Figure 4.3) are qualitatively similar (the snapshots of configurations obtained from the Markovian milestoning simulation procedure look very similar to those obtained from the SMCV and shown in Figures 4.4, 4.5, 4.6); however the differences in free energies between relevant states are smaller than the corresponding differences in PMF. This observation is expected, as in the SMCV more entropy is removed as we are effectively restraining 180 degrees of freedom (replicas evolve guided by the negative gradient of free energy in order parameter space). In contrast, in the

Markovian milestoning simulations less entropy is removed from the system, as by construction a trajectory restrained to remain in its Voronoi cell is equal to the equivalent sections of a conventional (unbiased) MD trajectory that is passing through the same cell.[232]

In Figure 4.9 we show the MFPTs to reach the configuration at the peak of the free energy curve (Figure 4.8). Here we only considered fluxes between adjacent cells (fluxes between non-adjacent cells represent about 13% of the total number of fluxes in our milestoning simulations). If we consider all fluxes (i.e. between nearest and non-nearest neighboring images), we determined that the difference in MFPTs with respect to those shown in Figure 4.9 is only of about 8%. These results suggest that the contribution of non-adjacent isocommittor surfaces to the kinetics of the nucleation process can be ignored (for a detailed discussion, see Appendix B in the study of Ovchinnikov *et al.*[267]) The results shown in Figure 4.9 suggest that the MFPTs to the configurations at the peak of the free energy curve of Figure 4.8 are approximately constant for milestones $B_{i+1} \cap B_i$ with i = 72, 71, …, 53. From the data shown in Figure 4.9, we calculated a simulated nucleation rate of 6.6×10^{10} [cm^{-3} s^{-1}] for our system, which is at a supercooling of 58 K. Unfortunately no experimental data is available for our system; however, our computed rate is in reasonable agreement with experimental and simulation values for the homogeneous nucleation of ice, which are on the order of 10^{10} [cm^{-3} s^{-1}][204, 259-260] at a supercooling of about 40 K.

4.4 Conclusions

The homogeneous nucleation of the IL [$dmim^+$][Cl^-] from its bulk supercooled liquid phase (58 K of supercooling) was studied using molecular simulation. The SMCV[264, 267] combined with OPs[268] for molecular crystals was used to have a string of replicas map a MFEP connecting the supercooled liquid with the monoclinic crystal phase. The converged SMCV

string was then used to initiate simulations using Markovian milestoning with Voronoi tessellations.[232, 267] These methods yield information about the free energy barrier, the size of the critical nucleus and the rate of nucleation. Our results indicate that the supercooled IL at 340 K has to overcome a free energy barrier of ~85 kcal/mol to form a critical nucleus of size ~3.4 nm. A simulated homogeneous nucleation rate of 6.6×10^{10} [cm^{-3} s^{-1}] was determined from our calculations. The values of the free energy barrier and the rate of nucleation are in reasonable agreement with experimental and simulation values obtained for the homogeneous nucleation of water and urea. Current work in our group is focused on the study of nucleation of ILs near surfaces and inside pores.

Chapter 5 Molecular Simulation of Heterogeneous Nucleation of an Ionic Liquid near a Graphitic Surface

5.1 Introduction

Ionic liquids (ILs) are organic salts having low melting temperatures, by convention below 100 °C[1, 270]. Due to their unique properties such as negligible vapor pressure, non-volatility and thermal stability at high temperatures, ILs can be used as "green" solvents to replace volatile organic solvents[271-274]. Because of their high ionic conductivity and wide electrochemical potential window, ILs can be used as electrolyte in lithium batteries, electric double layer capacitors, dye-sensitized solar cells and fuel cells[13-14, 113, 119, 274-276]. However, many organic salts have melting points above 25 °C, and thus are solid at room temperature[270]. Warner *et al* [45-49, 64, 172-176]recently synthesized solid-phase ionic organic materials, which are termed GUMBOS (Group of Uniform Materials Based on Organic Salts). These organic salts are essentially frozen ILs, having melting points between 25 °C and 250 °C. The properties of GUMBOS (melting point, solubility, hydrophobicity, polarity thermal stability, toxicity and viscosity) are highly tunable. For example, GUMBOS can be extremely hydrophobic or hydrophilic by variation in the constituent ions. Another advantage is that the preparation of GUMBOS is quite simple, sometimes requiring only requiring only a single-step ion-exchange reaction[45]. Warner *et al*[45-49, 64, 172-176] have demonstrated that GUMBOS have remarkable utility in a wide range of wide range of fields, such as biomedicine, analytical chemistry, optoelectronics, photovoltaics and separations.

The magnetic and optical properties of GUMBOS can be tuned by introducing shape anisotropy. 1D fluorescent nano-GUMBOS (nanowires and nanotubes) have been fabricated by confining the organic salts in porous templates such as track-etched polycarbonate or anodic

aluminum oxide membranes with cylindrical pores[64]. The structure of the nano-GMUBOS is limited by the size, shape and composition of the templating materials. Furthermore, ionogels are presented as a new class of hybrid materials involving ILs[62-63, 127-128, 177]. Here the properties of ILs are hybridized with another component, which can be organic (*e.g.* molecular weight gelator, biopolymer), inorganic (e.g. carbon nanotubes, silica) or hybrid organic–inorganic (*e.g.* polymer and inorganic fillers). Ionogels can enlarge the applications of ILs, which range from solid electrolytes to drug delivery to catalysis[63]. Therefore, in order to rationally design these nanomaterials, it is necessary to fundamentally understand the solidification of organic salts inside nanomaterials.

In addition to the practical interest described above, a fundamental understanding of nucleation that results from finite-size effects, varying dimensionality and surface forces is of scientific interest. Molecules confined within narrow pores, with pore width of a few molecular diameters, can exhibit a nucleation process and solid phases that are different from those observed in the bulk[73, 277]. New phenomena include formation of new phases, layering, shift in phase transition temperatures, etc. One of the challenges is to understand the physical mechanism of solidification in confinement. Various experimental techniques have been used to characterize the melting temperature and the solid structure of molecules confined inside nanomaterials[73, 277]. However, it is complicated to gain a complete picture of solidification from experiments alone. Some experimental issues include difficulties in distinguishing between fluid, amorphous and partially crystalline phases inside the pores; limitations in resolution due to factors such as very small amounts of material inside the nanopores; presence of long-lived metastable states, and difficulties in distinguishing these from thermodynamically stable states.

These difficulties are not present or can be overcome in computer simulations at the molecular and atomic level.

Solidification involves first the formation of an activated, short-lived species termed the critical nucleus; afterwards, this nucleus grows to form the crystal phase. Nucleation is an extremely challenging problem[184-191, 278-279], mainly because nucleation only involves a few molecules[280] (making experimental studies difficult) and involves timescales beyond those accessible through conventional molecular dynamics (MD) simulations. Rare events methods such as transition path sampling[217, 281-285], umbrella sampling[286-289], forward flux sampling[290-295], string method[296-298] have been used to study nucleation of different systems. In our previous simulation, MD simulations were used to study the homogeneous nucleation of the IL 1,3-dimethylimidazolium chloride, [dmim$^+$][Cl$^-$], from its supercooled liquid phase[298]. In that study we used the string method in collective variables (SMCV) [230] and Markovian milestoning with Voronoi milestoning[231-233] to study the nucleation process. Suitable order parameters (OPs)[217, 268] were selected as collective variables for the SMCV and Markovian milestoning procedures, which can measure local crystalline order in nm-sized regions, as well as distinguish between different crystal polymorphs and liquid phases. From these methods, we can get insights about the mechanism, the free energy barrier, the size of critical nucleus and the rates involved in the nucleation process of IL [dmim$^+$][Cl$^-$]. In this paper, we have used the above simulation methods to study the heterogeneous nucleation of IL [dmim$^+$][Cl$^-$] near a carbon surface (a graphene layer). This work is a further step in a series of studies aimed at understanding the nucleation and nucleation and growth of crystal of organic salts near surfaces and inside nanoporous materials.

The rest of paper is structured as follows. In the next section, we provide details of our models and computational methods (SMCV and Markovian milestoning with Voronoi

tessellations), as well as the main aspects related to the construction of our OPs. Our main results and discussion are shown in section 5.3. Firstly, a minimum free energy path (MFEP) connecting the supercooled liquid and the crystal phase of IL is obtained using the SMCV. Then, Markovian milestoning with Voronoi tessellations is used to calculate the free energy and rate of nucleation process. The results of heterogeneous nucleation in this study are compared with the homogeneous nucleation with the same box size and at the same temperature. In section 5.4, we summarize our main findings.

5.2 Computational details

5.2.1 Systems

We start with the crystalline structure of the IL [dmim$^+$][Cl$^-$] from the Cambridge Structural Database[243], corresponding to the experimental study of Arduengo[244]. The IL has a monoclinic crystalline structure with space group $P2_1/n$. The force field of the IL was all-atom nonpolarizable force field developed by Lopes, Pádua *et al*[84-88]. This force field can satisfactorily reproduce experimental values of density (differs in less than 1% from the experimental values reported by Fannin *et al*[245]), crystalline lattice parameters and melting point.

We investigated the heterogeneous nucleation of IL [dmim$^+$][Cl$^-$] near a graphene disk, and made direct comparisons with our results for homogeneous nucleation at the same degree of supercooling. Our system contains 2268 ion pairs in contact with the disk-like graphene layer, which has a diameter of 3 nm and was built using VMD[299]. Since this graphene disk can be placed near multiple facets of the crystalline IL, and it would be extremely time consuming to perform a detailed study of heterogeneous nucleation in each of these scenarios, we just studied the situation where the graphene disk is placed on the [-1,0,1] plane of the crystal IL. We simply placed the carbon disk on different planes of the crystalline IL, and rotate the graphene disk to

different angles on that plane, and determined the total energy of the system in each of these scenarios. Our results suggest that placing the carbon disk on plane [-1,0,1] leads to the configuration with the smallest total energy. Starting with the perfect crystal IL with its plane [-1,0,1] in contact with the graphene surface, we run a MD simulation in the *NPT* ensemble at 340 K for 2 ns to obtain the crystal structure at this temperature. The different views of the final configuration are shown in Figure 5.1. The snapshots suggest that some of the ions near the carbon disk adopt configurations that are different from the bulk crystal structure.

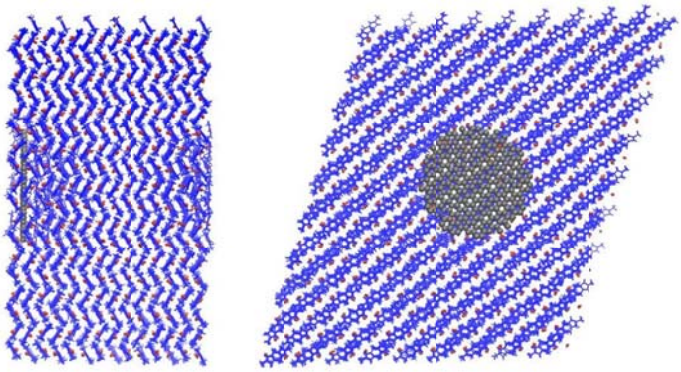

Figure 5.1 Representation simulation snapshot of the IL [$dmim^+$][Cl^-] in contact with graphitic surface with a diameter 3 nm (gray). Left: y-z view; Right: x-z view. Cations, anions are depicted correspondingly in blue and red.

All MD simulations were performed using a modified version of the NAMD software[248], in which the OPs, the SMCV and Markovian milestoning with Voronoi tessellations are implemented in C++ libraries. Constant pressure and temperature (*NPT*) with P =1 bar and T=340 K (58 K lower than the melting point) were performed for all MD simulations. A Langevin thermostat with a damping coefficient of 25 ps^{-1} was used to control the temperature, and the Nosé-Hoover Langevin piston with a damping time of 50 fs was employed to control the pressure at 1 bar. A time step of 0.5 fs was used in our simulations. The cutoff of Lennard-Jones interactions was set at 10 Å. The hydrogen bond lengths were constrained with the LINCS

algorithm[250]. Periodic boundary conditions were applied in all directions, and long range electrostatics were handled by particle mesh Ewald (PME)[249] with a cutoff of 12 Å.

5.2.2 Order parameters (OPs)

Selection of a set of OPs that are appropriate for describing nucleation is an essential aspect of our study. Here we used the OPs developed by Santiso and Trout[268] to distinguish the liquid from the solid state and from the intermediate states. The OPs are obtained by building a model for the generalized pair distribution function, and have been used successfully to study the formation of α-glycine crystals in solution, the crystallization of benzene from the melt, the polymorph transformation of terephthalic acid and crystalline order of aspirin molecules[217, 241, 300]. There are three types of OPs (a) distance OPs, which are sensitive to ordering in center-of-mass distances; (b) bond orientation OPs, which measure the orientation of a "bond" joining the center-of-mass molecules; and (c) relative orientation OPs, which measure the orientation of one molecule with respect to the second molecule. In our system, all OPs were built based on the cations [$dmim^+$]; no particular OPs were defined for the anions. In Figure 5.2, we plot the number distribution of these three types of OPs for our systems in contact with a graphene disk. The number distribution was obtained by averaging over 400 frames of MD simulations of both solid and liquid cations in contact with the carbon disk. This MD simulation is run in the NPT ensemble at 340 K for 2 ns. From Figure 5.2, it is clear that for all three types of OPs, the liquid and solid states have peaks at different values, indicating any of these OPs can serve as a good metric to detect crystalline order in nm-sized region. Comparing the distribution of OPs with that obtained previously for the bulk system (same system size) at the same temperature (Fig. 4.2), we found the OPs overlap more in the system with the graphene disk than in the bulk system. This observation is caused mainly by the IL molecules near the carbon disk, which can have a

structure different from that of the bulk crystal (Figure 5.1), which in turn can cause a reduction in the value of the OPs. Additional details are presented in our previous study[298].

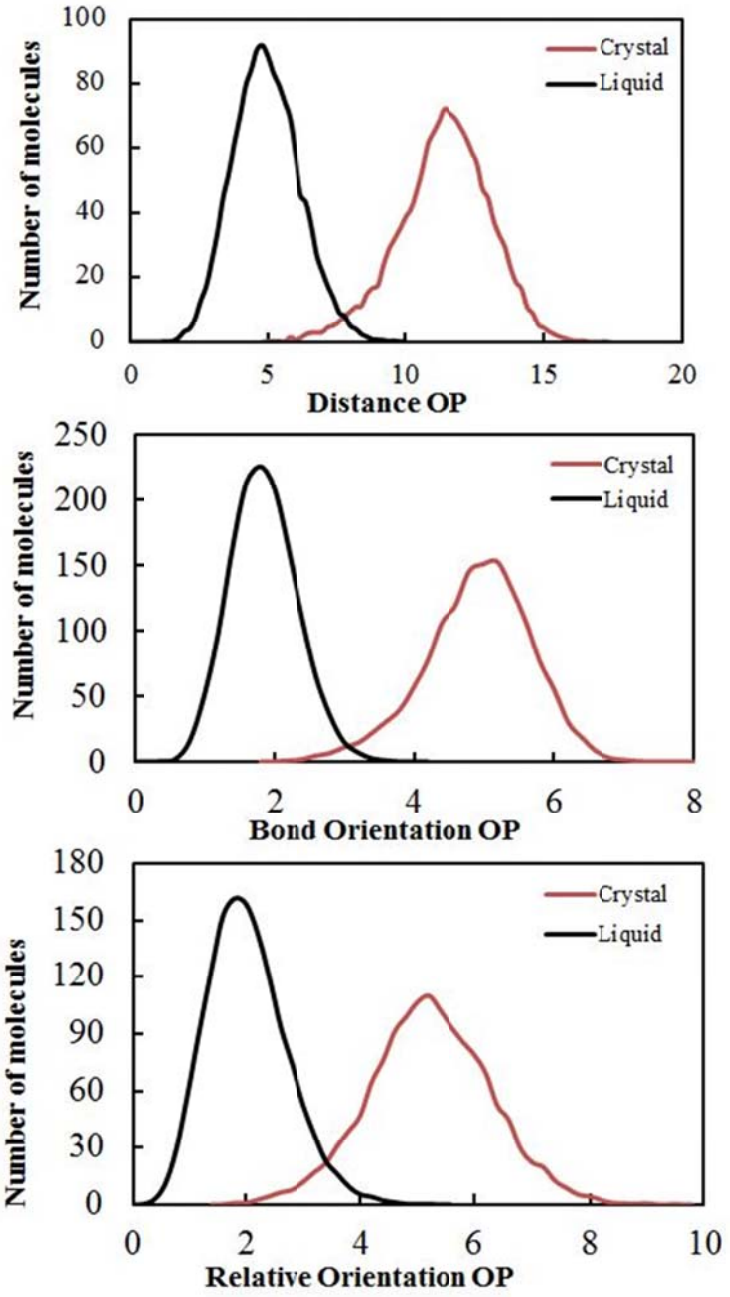

Figure 5.2 OPs for liquid and solid IL near carbon surface. The numbers of molecules of cations are plotted as a function of three types of OPs: distance order (top), bond orientation (middle) and relative orientation (bottom). These plots are averaged over 400 frames of solid and liquid IL near carbon surface.

5.2.3 String method in collective variables

In the study of activated events by MD simulation the minimum free energy path (MFEP) plays an important role, representing the reaction path of maximum likelihood in a given set of collective variables. In the SMCV, the string connecting two stable basins is discretized into a collection of representative "images". The images are allowed to "relax" in the direction of the negative gradient of the free energy. The final converged string corresponds to a MFEP between two endpoints state. The SMCV[230] involves several steps:

a) Generate an initial string connecting the crystal and liquid basins. The OPs described in the last section corresponding to each image is calculated. In our system, we obtained the initial string by collecting a number of intermediate states (31 replicas) on the trajectory of melting the crystalline system (Figure 5.1) at 800 K.
b) Evolution step. Each image is moved along the string in the direction of the component of $-M\big(\theta_n(t)\big)\nabla G(\theta_n(t))$ perpendicular to the string. The target OPs for the next step are estimated through this equation.

$$\theta_n(t+\Delta t) = \theta_n(t) - \Delta t\, M\big(\theta_n(t)\big)\nabla G\big(\theta_n(t)\big) \tag{5.1}$$

Where $\theta_n(t)$ denotes the OPs of the n-th image for the current step, Δt indicates the string time step, $M\big(\theta_n(t)\big)$ is the metric tensor and $\nabla G(\theta_n(t))$ is the negative gradient of the free energy with respect to the OPs (also called mean force). $\theta_n(t+\Delta t)$ indicates the target OPs of the n-th image for the next step. The evaluation of the term $M\big(\theta_n(t)\big)$ and $\nabla G(\theta_n(t))$ is performed from MD simulations for each replica, using an extended Hamiltonian coupled with harmonic potentials (which keep the OPs of each replica close to their target value).

$$\nabla G\big(\theta_n(t)\big) \approx -\langle[\theta_n(r) - \theta_n(t)] \cdot k \cdot [\theta_n(r) - \theta_n(t)]\rangle = \langle G_{rest}\big(\theta_n(t)\big)\rangle \tag{5.2}$$

$$M\big(\theta_n(t)\big) = \langle \nabla_r \theta_n(r) \otimes \nabla_r \theta_n(r) \rangle \tag{5.3}$$

Where $\theta_n(r)$ is the OPs of n-th image with a configuration r, k denotes the force constant matrix, $G_{rest}(\theta_n(t))$ is the force from harmonic restraining potential, $\langle\ \rangle$ indicates an ensemble average over the restrained simulation, and $\otimes$ denotes the outer (Kronecker) product.

In our system, short MD simulations (0.2 ns) in the *NPT* ensemble using this extended Hamiltonian are then run for each image. We choose the force constant k large enough so each image $\theta_n(r)$ remains close to its target OPs $\theta_n(t)$. After each step, the restraint force along the path in the multi-dimensional OP space is integrated to get the potential of mean force (PMF).

c) Parameterization step. The images in the string are then reparameterized to ensure the neighboring images are kept at approximately constant arc-length distance in OP space. This procedure is to prevent the images from eventually collapsing onto the free energy minima. The interpolating is done using b-splines[301], which makes the interpolating curve smooth and greatly improves convergence.

d) The steps described in steps b and c are repeated until the string converges. There are two ways to monitor the convergence. One is by the Fréchet distance[252-253] between the PMF profiles. The other way is by comparing the OPs of $\theta_n(t + \Delta t)$ and $\theta_n(t)$; convergence is reached when these OPs are very close and do not change appreciably between successive iterations. Convergence was assumed when the Fréchet distance between two successive PMF profiles reaches a value <0.10

In the SMCV, each image is evolved independently and has no communication with the other images, which makes the method trivially parallelizable. Another advantage is two endpoints of the string can evolve freely towards minima of the free energy. Therefore, we don't

need to know the location of the minima at the beginning of the simulation. Additional details can be found elsewhere[230, 298].

5.2.4 Markovian milestoning in Voronoi tessellations

Nucleation processes can have relevant time scales spanning many orders of magnitude, making it inaccessible by brute-force MD simulations. In Markovian milestoning, the MD trajectory of nucleation (e.g., approximately mapped from SMCV simulations) is split up into much shorter sub-trajectories between a set of hypersurfaces, also called milestones. Each sub-trajectory is restricted using half-well restraining potentials[232] (soft wall restraints) to keep it inside its Voronoi cell. The restraining potential is equal to zero in the interior of the cells, and acts as a penalty function towards the cell boundary when the trajectory crosses the milestones. Therefore, the equilibrium distribution inside the cell is the same as that of an unbiased simulation. The dynamics of the system is reduced to that of a discrete state continuous-time Markovian chain in the state space of the milestones indices. From these sub-trajectories, we can estimate the actual free energy profile along the nucleation path and the nucleation rate. This procedure involves two steps:

a) Redistribute the images. The converged string from the SMCV is the input for the Markovian milestoning with Voronoi tessellations. Before doing this, we should carefully distribute the images on the string. High image density in regions of higher curvature can cause the trajectories collide with boundaries that correspond to their non-adjacent cells, which affects accuracy of the results[267]. Low image density can cause the computation to be unable to collect enough statistically relevant data. Therefore, in order to enable sufficient collisions with their neighboring cells, the images in regions where the free energy gradient is larger should have

higher density. In our system, the 31 images on the converged string are redistributed to 75 images by interpolating additional replicas.

b) Definition of the milestones. We take the redistributed images on the string, define a partition in OP space and associate a Voronoi cell in OP space to each image. The milestones are defined as the edges of the Voronoi tessellations in OPs space.

c) Sampling. Each image on the string is associated with a Voronoi cell. MD simulations are then run for each replica, where the OPs of each image are confined to remain within its own Voronoi cells by soft wall restraints. The dynamical properties of the replicas are unperturbed when they are in the interior of their own cells. When a given trajectory crosses over its milestones, the soft wall restraint potential will bring it back to its Voronoi cell.

From the trajectory in each Voronoi cell, we record these quantities[80,82-84].

t_n : the simulation time in cell B_n

$N_{n,m}$: the number of collisions the replica in cell B_n makes with the boundary of cell B_m during the simulation time t_n.

$N_{a,b}^{n}$: the total number of transitions from milestone a to milestone b during the simulation confined to cell B_n

t_a^n : total time during which a was the most recent milestone visited by the system.

From these statistical data, we can calculate the rate $k_{n,m}$ of escape from cell B_n to cell B_m.

$$k_{n,m} = \frac{N_{n,m}}{t_n} \tag{5.4}$$

At statistical steady state, the net probability flux in and out of each Voronoi cell should be zero. Therefore, the equilibrium probability π_n can be estimated through the following equations:

$$\sum_{\substack{n=1 \\ n\neq m}}^{N} \pi_n \, k_{n,m} = \sum_{\substack{n=1 \\ n\neq m}}^{N} \pi_m \, k_{m.n} \tag{5.5}$$

$$\sum_{n=1}^{N} \pi_n = 1 \tag{5.6}$$

From the probabilities π_n, we can compute the free energy F_n for the nucleation process.

$$F_n = -k_B T \ln \pi_n \tag{5.7}$$

$k_{a,b}$, the rate of escape from Voronoi cell B_a to cell B_b conditional on the system being in B_a, can be calculated from equations 5.8-5.10. $N_{a,b}$ and R_a denote the average properties extracted from simulations confined to the Voronoi cell B_a, weighted by the equilibrium probability π_a of finding the system in cell B_a.

$$k_{a,b} = \frac{N_{a,b}}{R_a} \tag{5.8}$$

$$N_{a,b} = \sum_{n=0}^{N} \pi_n \, N_{a,b}^{n} / t_n \tag{5.9}$$

$$R_a = \sum_{n=0}^{N} \pi_n \, t_a^n / t_n \tag{5.10}$$

The rate $k_{a,b}$ for every Voronoi cell defines a rate matrix, which represents the complete dynamics of the Markovian process. The rate matrix can be used to compute many important quantities. For example, the mean first passage time (MFPTs) $t_{b,b*}$ from any milestone to a given

milestone b^* can be computed by solving the linear system of equations (5.11). In our system, we use the milestone adjacent to the Voronoi cell corresponding to the peak of free energy profile as the reference milestone b^*. In particular, the rate matrix for our system is ill conditioned because the rate matrix varies over at least 6 orders of magnitude. This problem is overcome by using the arbitrary precision floating-point library implemented in the Sage software[254] to solve the system of equations. Additional details can be found elsewhere[231-233, 298].

$$\sum_{b \neq b^*} k_{a,b} t_{b,b^*} = -1, \quad a \neq b^* \tag{5.11}$$

5.3 Result and discussion

5.3.1 Description of MFEP from SMCV

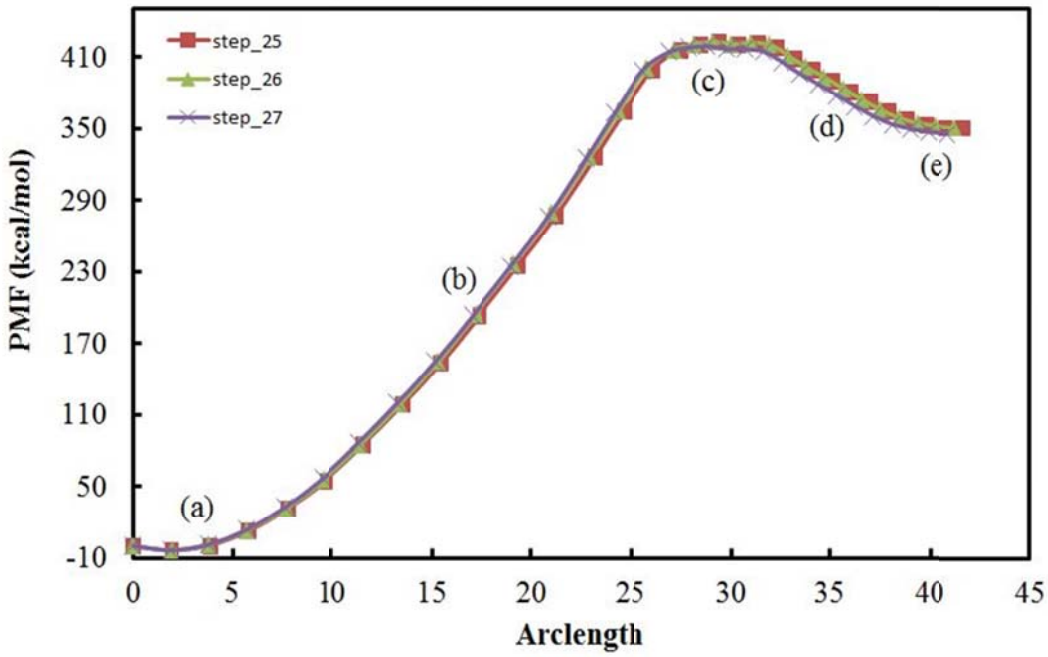

Figure 5.3 The PMF associated with the MFEP for heterogeneous nucleation of IL $[dmim^+][Cl^-]$ from its supercooled liquid phase at 340 K and 1 bar. The left and right sides of the curve correspond to crystal and liquid states. Simulation snapshots of states labeled here are shown in Figure 5.4.

In Figure 5.3, we show the PMF as a function of the arc-length for the last three steps of the SMCV, for [dmim$^+$][Cl$^-$] nucleating near a graphene disk. Here the PMF is the line integral of the restraint force along the string and the arc-length represent the distance between bond orientation OPs. The PMF profiles almost do not change over the last three steps of the SMCV, suggesting that the string has converged. Figure 5.3 indicates that the difference between the crystal phase and the super-cooled liquid phase is about 346 kcal/mol at a superstation of 58 K; the PMF barrier between the supercooled liquid and the state at the top of the PMF profile is about 54 kcal/mol. For homogeneous nucleation of the same IL, same system size and same supercooling temperature, we obtained a difference of about 141 kcal/mol between the crystal and the liquid, and a PMF barrier of about 163 kcal/mol. The PMF barrier is about three times smaller when the IL is in contact with a graphene disk.

As explained in section 5.2.3, the converged string from SMCV illustrates the MFEP connecting the liquid and solid state. In Figure 5.4, several snapshots of the relevant states along the MFEP are shown. The cations are colored based on the value of their bond orientation OPs in the cell containing the molecules, where those colored in red have lower bond orientation OPs (liquid-like) and those colored in blue have higher bond orientation OPs (crystal-like). The super-cooled liquid is depicted in Figure 5.4e. The liquid phase is metastable and in order to transitionto another phase it needs to pass over a free energy barrier. In homogenous nucleation, the transformation is usually induced by the supersaturation temperature. In heterogeneous nucleation, the transition can be induced by the presence of solid material that has nucleation-inducing properties. As we move from left to right along the PMF in Figure 5.3, first the cations rearrange to form a small size of nucleus with ordered structure (Figure 5.4d). This nucleus is not stable and very easy to dissolve back to liquid rather than grow. Then the ordered region of

cations and anions grows slightly and become more organized (Figure 5.4c), which corresponds to the peak of PMF profile in Figure 5.3. From Figure 5.4c to 5.4a, the critical nucleus grows and the PMF decreases until the system reaches the thermodynamically stable crystal. If we arbitrarily define the cations with OPs > 3.5 (Figure 5.2) as crystalline, we estimate that the critical nucleus has a size of ~3.0 nm at this degree of super-cooling. This size is smaller than the one observed in the critical nucleus upon homogeneous nucleation (~3.6 nm).

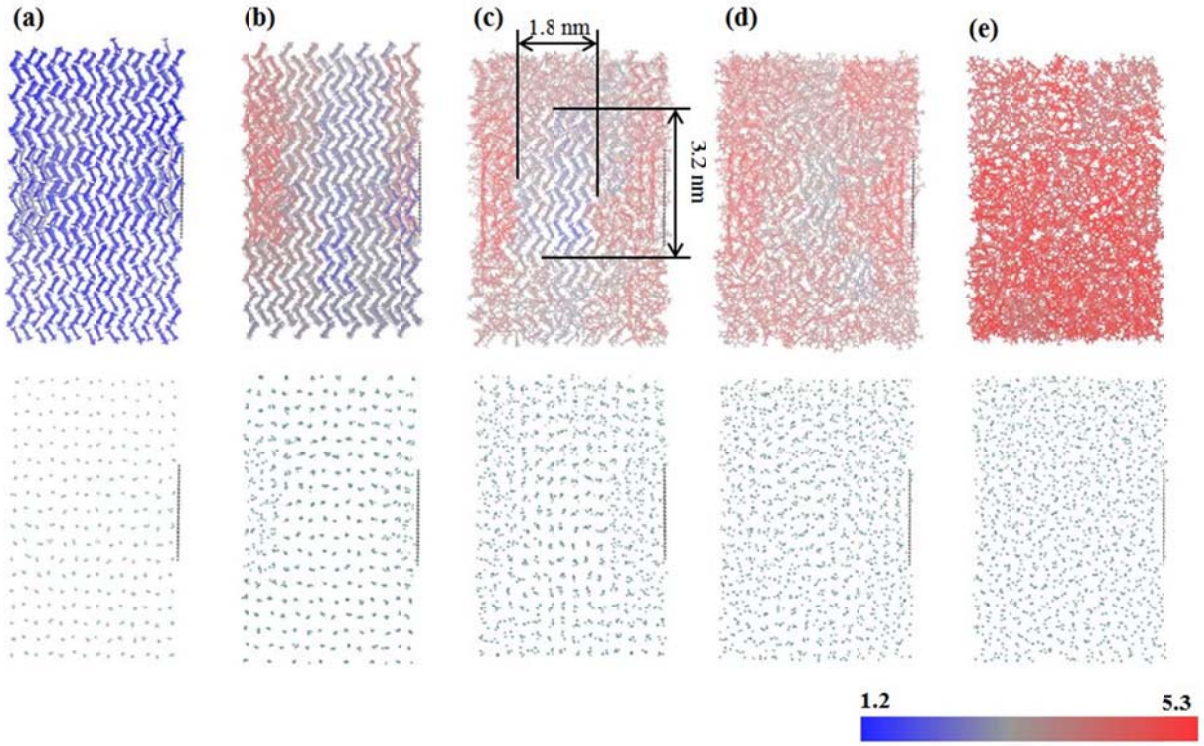

Figure 5.4 *y-z* side views of simulation snapshots of states labeled along the MFEP shown in Figure 3. The cations (top row) are color-coded according to the value of their bond orientation OPs (red = crystal-like, blue = liquid-like). The anions are shown on bottom row and are not color-coded. The carbon disk can be observed at the right side in each snapshot.

As the presence of the graphene disk seems to induce changes in the structure of the ions close to it, we focus our attention on those ions within a 'cylinder' capped by the carbon surface

(see Figure 5.5). The cations are colored using the same scheme as in Figure 5.4. Three significant results can be gleaned from this figure.

a) The critical nucleus forms near the graphite surface, with a few pre-melted or disordered layers of ions between the nucleus and the carbon disk (Figure 5.4c). We want to highlight that the critical nucleus forms near the graphene surface; it is not in direct contact with the carbon disk, but it is not far away from the surface either. This observation suggests the graphene surface can facilitate the formations of the critical nucleus.

b) Layers of disordered cations near the graphene surface are observed in all snapshots, including the crystal (Fig. 5.5a) and liquid (Fig. 5.5e) phases. Notice that the two endpoints of the string can evolve freely to the nearest minimum of free energy during the SMCV simulations. So, the two endpoints on the converged string are not affected by the initial string. In Figure 5.6, we present the number density profiles for the liquid and solid IL along the dashed line in Figure 5.5 (in the direction perpendicular to the graphitic surface). The density profiles shown in Figure 5.6 exhibit significant layer effects for both states, with local maxima near the surface. Comparing the density profiles, the crystal IL exhibit more pronounced layering effects than the liquid IL since crystal IL has ordered structure. Layering effects for the liquid IL have been previously reported for ILs in confinement[23, 29, 41, 302]. Overloop and Gervan[74] studied the freezing of water in porous silica, and they suggest that the confined solid phase, up to three molecular layers adjacent to the pore wall, has a structure that is different from the bulk crystal phase and from that of the free liquid.

c) The cations near the graphitic surface have the orientation with their imidazolium rings lie parallel to the graphitic surface. In Figure 5.7, we present snapshots of the cations in the cylinder near the graphene surface. The cations are now colored according to their value of $\cos(\Theta)$,

where Θ is the angle formed between a vector normal to the imidazolium ring and the vector normal to the graphitic surface. From Figure 5.7, we can observe that the cations in the two layers adjacent to the graphitic surface (Figure 5.6) have orientations that are different from that of the cations far away from the graphitic surface, both in the crystal phase and in the liquid phase. The cations near the carbon surface tend to align with their imidazolium rings parallel to the graphene disk. For the crystal phase, the cations far away from the graphitic surface have their imidazolium rings tilted with respect to the graphitic surface, with the angle Θ between 0° and 44°. In the liquid phase, the cations far away from the graphitic surface are disordered and do not have any orientation preference.

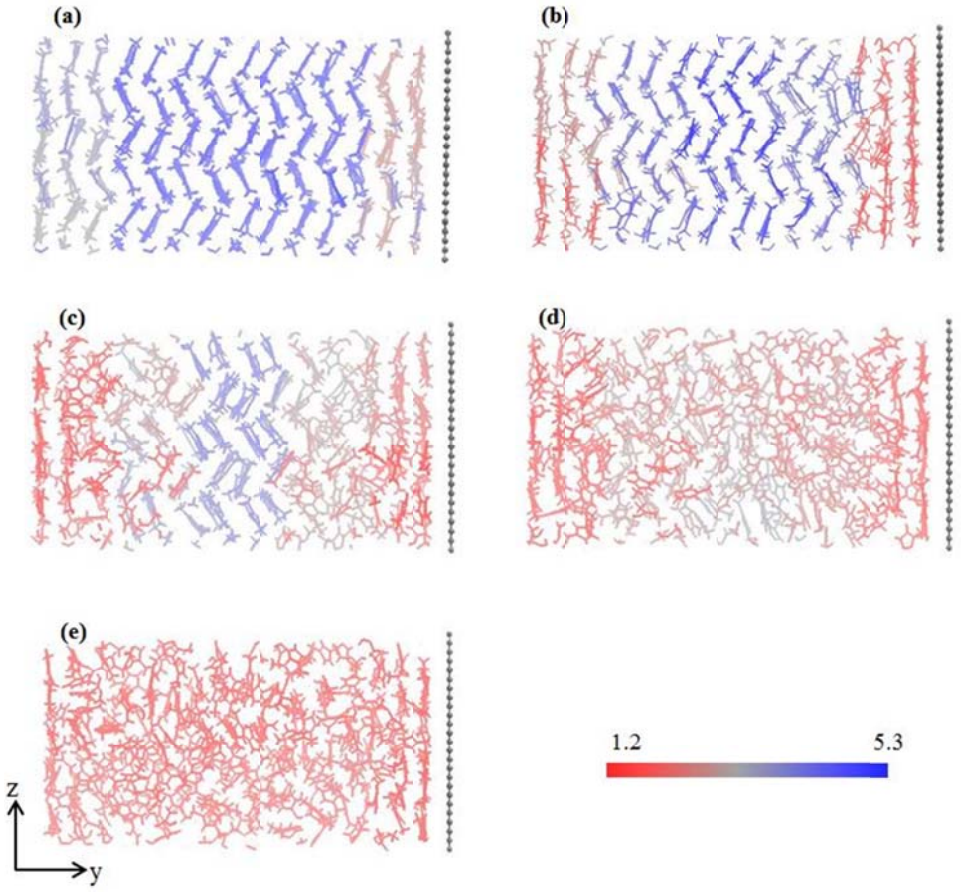

Figure 5.5 *y*-*z* side views of molecules in a cylinder. On the right of the cylinder it is the carbon disk. The cations (top row) are color-coded according to the value of their bond orientation OPs (red = crystal-like, blue = liquid-like).

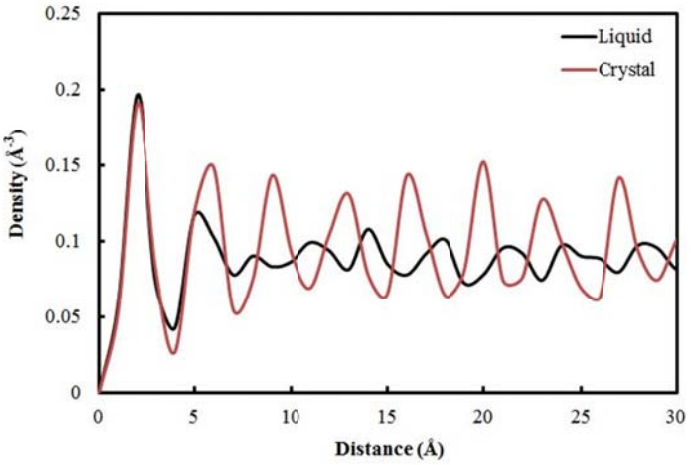

Figure 5.6 Number density profile for the IL in the cylinder along the dashed line in Figure 5.5.

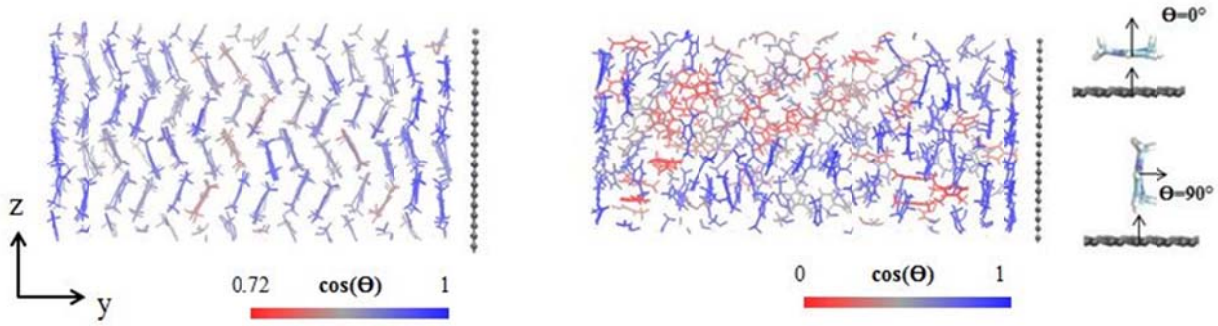

Figure 5.7 Snapshots of cations in the cylinder near the graphitic surface. Left: crystal; Right: liquid. The cations are colored according to the value of cos(Θ), where Θ represent the angle formed between a direction vector normal to the imidazolium ring and the vector normal to the graphitic surface.

5.3.2 Free energy path and nucleation rate from Markovian milestoning with Voronoi tessellations

In our simulations using Markovian milestoning with Voronoi tessellations, the MFEP as mapped from the SMCV runs (31 replicas) was expanded to a total of 75 images by interpolating additional replicas. A Voronoi cell was associated to each image, where the edges of the Voronoi cells are identified as milestones. In order to visualize the OPs for each image, we used principal component analysis (PCA) to reduce the dimensions of the OPs from 180 to 2.

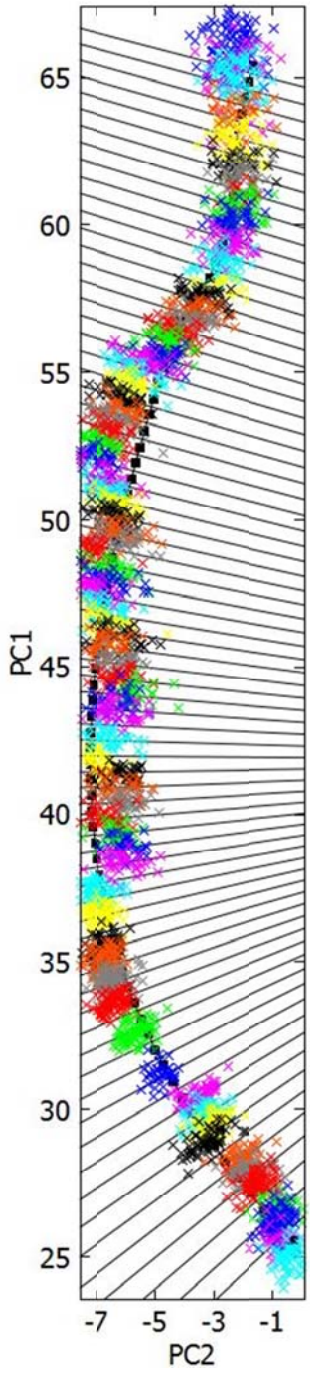

Figure 5.8 Voronoi tessellation of the MFEP in the first two principal components PC1 and PC2 in OP space. The black dots represent the initial configurations used in the Markovian milestoning simulations; these 75 initial configurations were obtained from the SMCV simulations as well as by interpolating additional replicas. The different colors show a few snapshots of the OPs, as obtained from the simulations using Markovian milestoning with Voronoi tessellations. $N_{a,b}{}^{n}$

In Figure 5.8, we show the projections of MFEP onto the space of the first two principal components corresponding to the largest variance along the entire path. The first two principal components contain over 98% of the variance. Specifically, the first component PC1 contains over 96% of the overall variance of the OPs. The second principal component (PC2) contains over 2% of the overall variance. MD simulations are performed for each image, in which soft wall restraints are used to confine each trajectory in its own Voronoi cell. In Figure 5.8, we also show the projections of the OPs for several snapshots of these trajectories, in which different colors represent different trajectories. Figure 5.8 suggests that the trajectories spend most of the simulation time in their own Voronoi cells; they can also occasionally escape from their own Voronoi cell and go to neighboring cells. This is the result of the soft walls restraints. Another observation is the MFEP lies approximately in the center of the transition tube obtained by the trajectory of each cell, which indicates the string evolves slowly around the MFEP. The snapshots of the final configurations from the Markovian milestoning procedure are very similar to those shown in Fig. 5.4 (converged string from the SMCV).

From the data $t_{n,}N_{n,m}$, $N_{a,b}{}^{n}$ and $t_{a}{}^{n}$ (explained in Section 5.2.4) obtained from Markovian milestoning, we can calculate the free energy along a coordinate parameterizing the transition using equations (5.4)-(5.7), as well as the MFPTs from equations (5.8)-(5.11). In Figure 5.9, the free energy for the heterogeneous nucleation process is shown as a function of the Voronoi cell index. From Figure 5.9, we found the free energy difference between the supercooled liquid and the configuration at the maximum of the curve is about 49 kcal/mol, and the difference in free energy between the crystal and liquid [$dmim^{+}$][Cl^{-}] is about 165 kcal/mol. The overall shape of this curve is very similar to that of the PMF (Fig. 5.3), but the free energy differences are significantly smaller. As discussed by Ovchinnikov *et al*[267]., the PMF computed from SMCV is

different from the free energy computed from Markovian milestoning. In the SMCV, the string is restricted to evolve in the direction of the negative gradient of the free energy in its OPs space, which includes restraining 180 degrees of freedom. In the Markovian milestoning simulation, less entropy is removed because each trajectory can evolve in its own Voronoi cell. In another word, the PMF is the integral of the restraint force along a single path (the MFEP), while the free energy profile is the integral of many paths (described by the transition tubes in Figure 5.8). Therefore, the free energy profile is a more accurate representation of the free energy involved in the heterogeneous nucleation process than the PMF (Fig. 5.3). Comparing the free energy profile from homogeneous nucleation at the same temperature and same system size (Fig. 4.8), we found the free energy barrier for the heterogeneous is much smaller (for the homogeneous nucleation, the free energy barrier is 85 kcal/mol). These observations suggest that the graphene surface can promote the nucleation of IL, with the critical nucleus forming near the carbon disk surface, rather than at the grapheme surface or far away from it (Figs. 5.4 and 5.5).

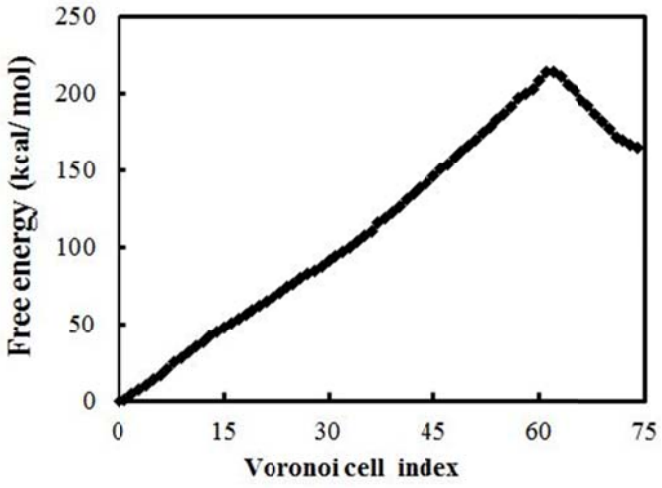

Figure 5.9 Free energy associated with the heterogeneous nucleation of a crystal of [$dmim^+$][Cl^-] from its supercooled liquid phase at 340 K and 1 bar, as obtained from the simulations using Markovian milestoning with Voronoi tessellations. The left and right sides of the curve correspond to crystal and liquid states.

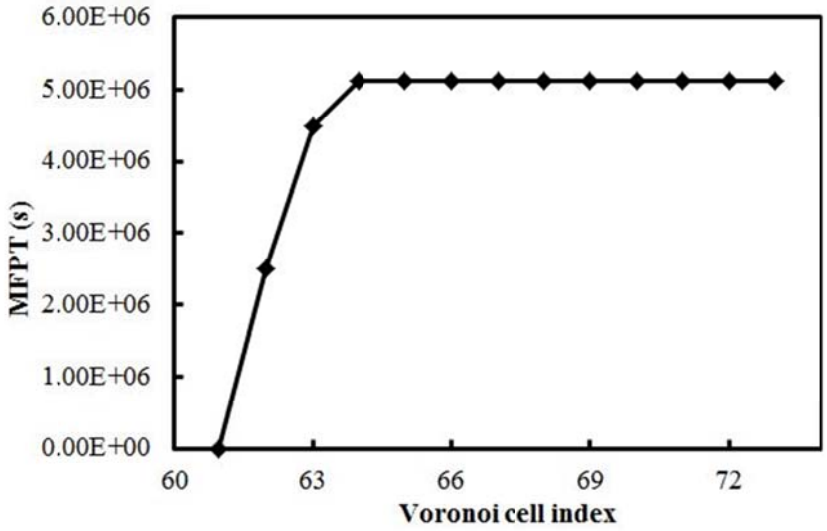

Figure 5.10 Mean first passage time from each milestone on the liquid side of the free energy profile to the milestone corresponding to the peak of the free energy profile in Figure 5.9.

In Figure 5.10, we show the MFPTs from each milestone on the liquid side of the free energy profile to the milestone at the peak of the free energy profile. Here we only consider the transitions between adjacent cells. As discussed by Ovchinnikov *et al*[267]., the transitions between non-adjacent Voronoi cells can affect the accuracy of the computation. Therefore the images on the converged string from the SMCV are carefully distributed to avoid large density images on the regions of high curvature of the MFEP (Fig. 5.8). In our simulation, the transitions between non-adjacent cells only represent about 14 % of the total number of of transitions. If we consider the transitions between adjacent cells and non-adjacent cells, the MFPTs are very similar to those reported in Figure 5.10 (the maximum difference is only about 8 %). This observation indicates that the contribution of non-adjacent isocommittor surfaces to the kinetics of the nucleation process can be ignored. Figure 5.10 indicates that the characteristic time for the transformation to the critical nucleus is 5.1×10^{6} s. By taking our data, multiplied it by the volume of our simulation box and took the inverse of all the resulting data, finally we get a nucleation rate of 4.75×10^{11}

cm^{-3} s^{-1}. The nucleation rate for the heterogeneous nucleation is one order of magnitude larger than the one determined for the homogeneous nucleation of the same system at the same temperature (6.6×10^{10} cm^{-3} s^{-1}).

5.4 Conclusions

We studied the heterogeneous nucleation of an IL [$dmim^{+}$][Cl^{-}] from supercooled liquid phase in contact with a graphene disk of diameter 3 nm and a supercooling of 58 K, using molecular dynamics simulations. First, the string method in collective variables (SMCV) was used to map a minimum free energy path (MFEP) connecting the liquid and the crystal basins, by evolvingg a set of replicas of the system guided by the negative gradient of the free energy in the order parameter (OP) space. Then, the Markovian milestoning with Voronoi tessellations method was used to obtain accurate estimates of the free energy and rates involved in the nucleation process, by matching together information obtained from multiple simulations where each trajectory is confined to remain within its own Voronoi cell in OP space, using soft wall restraints. In these methods, OPs are used to measure local structure and distinguish between the crystal, liquid and intermediate states. Our approach has the advantage of not requiring the system follow the time evolution of the transition between liquid and solid states. From the simulation, we can obtain some insights about the heterogeneous nucleation, such as the nucleation mechanism, critical nucleus size, free energy barrier and nucleation rate.

Our results suggest the critical nucleus forms near the carbon surface and has a size on the order of ~3.0 nm, which is smaller than the one observed for the homogeneous nucleation of the same system at the same temperature (~3.6 nm). The overall crystal structure is slightly different from the crystal observed in the bulk. The layers of ions next to the graphene surface lie with their imidazolium rings parallel to the carbon disk, and thus exhibit a structure that is

different from that of the crystal formed during the homogeneous nucleation process. When the critical nucleus forms during the nucleation process, these few layers of ions also separate the critical nucleus from the graphene disk. Our results also indicate that, at a super-cooling of 58 K, the subcooled liquid in contact with the carbon surface has to overcome a free energy barrier of ~49 kcal/mol to reach the thermodynamically stable crystal phase. This free energy barrier is much smaller than that found for the homogenous nucleation process (~85 kcal/mol), suggesting that the graphene surface can promote the nucleation of the IL. The rate determined for the heterogeneous nucleation process (~4.75×10^{11} [cm^{-3} s^{-1}]) was one order of magnitude larger than the one determined for homogeneous nucleation (6.6×10^{10} cm^{-3} s^{-1}). This study is a further step to a series of research aimed at understanding the nucleation and crystallization of organic salts inside nanomaterials.

Chapter 6 Summary and Future Work

6.1 Conclusions

We have conducted a series of molecular simulation studies aimed at understanding the structure and dynamical properties of liquid phases of ionic liquids (ILs) confined inside nanoporous carbons, as well as the homogeneous and heterogeneous nucleation of crystal phases of ILs. We first studied the properties of liquid phases of the ILs [$dmim^+$][Cl^-] and [$emim^+$][NTf_2] when confined inside the ordered mesoporous carbon CMK-5[303]. The findings were compared with similar results observed for the same ILs inside an isolated amorphous carbon nanopipe (ACNP) (i.e., no IL adsorbed on the outer surface of the ACNP) and inside a model CMK-3 ordered mesoporous carbon of similar pore size. These carbon nanomaterials, CMK-3 and CMK-5, consist of nanorods (CMK-3) or nanopipes (CMK-5) arranged in a hexagonal array and thus exhibit regularly interconnected nanopores; the walls of the rods and pipes are made of amorphous carbon. Systems of ILs inside ordered mesoporous carbons are relevant for applications in electrochemical double-layer capacitors (EDLCs). Our results indicate that the interactions between the ions and the pore walls significantly influence the structure and dynamics of the ILs in these systems. In all these models, ions inside the pore form different layers near the nanomaterials and their mobility is slower than that of the bulk ions. The ions far away from the nanomaterials have properties similar to those of the bulk ions. We also found the ILs in the outside of the ACNPs of CMK-5 exhibit faster dynamics than the ILs when they are in CMK-3 material of the same pore size. By comparing different models, we found that the ions prefer to stay closer to the carbon walls in CMK-5 due to the presence of ions inside and outside the thin walls of the ACNPs. Another observation is that there are more ions confined inside the ACNPs of CMK-5 (i.e., with IL also adsorbed inside the nanopipes) model than ions inside an

isolated ACNP. ILs adsorbed outside of the ACNPs of CMK-5 have faster dynamics and remain closer to the carbon surfaces when compared to the same ILs adsorbed in CMK-3 materials. The trends are IL-specific: [$dmim^+$][Cl^-] have slower dynamics when they are inside an isolated ACNP than the circumstance when they are inside the ACNPs of CMK-5; in contrast, [$emim^+$][NTf_2^-] move faster when they are inside an isolated ACNP than the situation when they are inside the ACNPs of CMK-5.

In our second project[298], the homogeneous nucleation of the ionic liquid [$dmim^+$][Cl^-] from its supercooled liquid phase in the bulk was studied using molecular simulations. The string method in collective variables (SMCV)[264] was used to sketch a minimum free energy path (MFEP) connecting the supercooled liquid and the crystal phases, from which we can estimate the size of critical nucleus as well as the nucleation mechanism. The converged string from SMCV was used as the input to the Markovian milestoning with Voronoi tessellations[232]. This method yields the free energy profile and mean first passage times (MFPTs) along the nucleation process. In the above two methods, the OPs developed by Santiso and Trout[268] were used to measure the local order in nm-sized regions and distinguish between crystal-like and amorphous (liquid-like) groups of ions. Our results indicate that, at a supercooling of 58 K, the free energy barrier for the supercooled liquid is about 85 kcal/mol and the critical nucleus size is about 3.6 nm. A simulated homogeneous nucleation rate of 6.6×10^{10} cm^{-3} s^{-1} was obtained for our system, which agrees qualitatively with the homogeneous nucleation of ice at the similar degree of supercooling in literature. Furthermore, in order to understand the physical significance of the states along the MFEP, the finite size effects were discussed based on the classical nucleation theory and the results from a bigger system. We found the relative size ratio of critical nucleus to the total system size can influent the results of MFEP and the free energy profile along it.

Finally, the SMCV and Markovian milestoning were also used to investigate the heterogeneous nucleation of IL [$dmim^+$][Cl^-] at the same temperature. We determined that the critical nucleus size is about 3 nm, which is smaller than that observed during a homogeneous nucleation process at the same temperature. Another observation is that the cations in the two molecular layers adjacent to the graphitic surface have a structure that is different from that in the bulk liquid or solid during the nucleation process. Our results from the Markovian milestoning in Voronoi tessellations indicate that the free energy barrier is about 49 kcal/mol (lower than the one observed during homogeneous nucleation) and the nucleation rate is 4.75×10^{11} cm^{-3} s^{-1} (one order of magnitude larger than the one observed during homogeneous nucleation). These results suggest that the graphitic surface can promote the nucleation of ILs. Results from this study will be submitted for publication soon.

In all these projects, MD simulations have assisted us in understanding the properties of ILs at the molecular level. To the best of our knowledge, this is the first time that homogeneous and heterogeneous nucleation of systems as complex as ILs has been studied using molecular simulations. In addition to adding to fundamental knowledge, our simulations can provide molecular-level information that, when combined with relevant experiments, can lead to useful insights for applications related to energy storage in EDLCs, and developing IL-based nanomaterials.

6.2 Proposed work

A proposed research in this area could be studying the nucleation of ILs confined inside nanoporous materials. Furthermore, we can focus on how nucleation of ILs in confinement is affected by the pore shape, surface roughness, and the chemical heterogeneity. Many researchers have reported that the new physics (such as shifting in the freezing temperature, new phases,

inhomogeneous properties) can occur due to surface forces and reduced dimensionality[77, 83, 277, 304]. For example, Hung *et al*[304] used Monte Carlo simulation to study the freezing and melting of Lennard-Jones carbon tetrachloride confined within multiwalled carbon nanotube of different diameters. They found the frozen confined phase forms concentric layers rather than a 3D crystal. Lepi *et al*[83] performed MD simulation and found that the atomically flat carbon surfaces can promote the heterogeneous nucleation of ice, while molecularly rough surfaces do not. Besides, studying the nucleation of ILs confined inside nanomaterials will be directly related the synthesis of GUMBOS.

References

1. Thomas;, W. P. W., *Ionic liquids in Synthesis*. Wilet-VCH: Weinheim, 2008.

2. Plechkova, N. V.; Seddon, K. R., Applications of ionic liquids in the chemical industry. *Chemical Society Reviews* **2008,** *37* (1), 123-150.

3. BASF, BASF to present BASIL ionic liquid process at technology transfer forum.

4. Walden, P., Organic solutions- and ionisation means. III. Chapter: Internal friction and its connection with conductivity. *Zeitschrift Fur Physikalische Chemie--Stochiometrie Und Verwandtschaftslehre* **1906,** *55* (2), 207-249.

5. Lin, R.; Taberna, P. L.; Chmiola, J.; Guay, D.; Gogotsi, Y.; Simon, P., Microelectrode Study of Pore Size, Ion Size, and Solvent Effects on the Charge/Discharge Behavior of Microporous Carbons for Electrical Double-Layer Capacitors. *Journal of the Electrochemical Society* **2009,** *156* (1), A7-A12.

6. Service, R. F., Materials science - New 'supercapacitor' promises to pack more electrical punch. *Science* **2006,** *313* (5789), 902-902.

7. Miller, J. R.; Simon, P., Materials science - Electrochemical capacitors for energy management. *Science* **2008,** *321* (5889), 651-652.

8. Simon, P.; Gogotsi, Y., Materials for electrochemical capacitors. *Nature Materials* **2008,** *7* (11), 845-854.

9. Armand, M.; Tarascon, J. M., Building better batteries. *Nature* **2008,** *451* (7179), 652-657.

10. Hagiwara, R.; Lee, J. S., Ionic liquids for electrochemical devices. *Electrochemistry* **2007,** *75* (1), 23-34.

11. Lu, W.; Fadeev, A. G.; Qi, B. H.; Smela, E.; Mattes, B. R.; Ding, J.; Spinks, G. M.; Mazurkiewicz, J.; Zhou, D. Z.; Wallace, G. G.; MacFarlane, D. R.; Forsyth, S. A.; Forsyth, M., Use of ionic liquids for pi-conjugated polymer electrochemical devices. *Science* **2002,** *297* (5583), 983-987.

12. Largeot, C.; Portet, C.; Chmiola, J.; Taberna, P.-L.; Gogotsi, Y.; Simon, P., Relation between the ion size and pore size for an electric double-layer capacitor. *Journal of the American Chemical Society* **2008,** *130* (9), 2730-+.

13. Fernicola, A.; Scrosati, B.; Ohno, H., Potentialities of ionic liquids as new electrolyte media in advanced electrochemical devices. *Ionics* **2006,** *12* (2), 95-102.

14. Galinski, M.; Lewandowski, A.; Stepniak, I., Ionic liquids as electrolytes. *Electrochimica Acta* **2006,** *51* (26), 5567-5580.

15. Kotz, R.; Carlen, M., Principles and applications of electrochemical capacitors. *Electrochimica Acta* **2000,** *45* (15-16), 2483-2498.

16. Abdallah, T.; Lemordant, D.; Claude-Montigny, B., Are room temperature ionic liquids able to improve the safety of supercapacitors organic electrolytes without degrading the performances? *Journal of Power Sources* **2012,** *201*, 353-359.

17. McEwen, A. B.; McDevitt, S. F.; Koch, V. R., Nonaqueous electrolytes for electrochemical capacitors: Imidazolium cations and inorganic fluorides with organic carbonates. *Journal of the Electrochemical Society* **1997,** *144* (4), L84-L86.

18. McEwen, A. B.; Ngo, H. L.; LeCompte, K.; Goldman, J. L., Electrochemical properties of imidazolium salt electrolytes for electrochemical capacitor applications. *Journal of the Electrochemical Society* **1999,** *146* (5), 1687-1695.

19. Timperman, L.; Galiano, H.; Lemordant, D.; Anouti, M., Phosphonium-based protic ionic liquid as electrolyte for carbon-based supercapacitors. *Electrochemistry Communications* **2011,** *13* (10), 1112-1115.

20. Jarosik, A.; Krajewski, S. R.; Lewandowski, A.; Radzimski, P., Conductivity of ionic liquids in mixtures. *Journal of Molecular Liquids* **2006,** *123* (1), 43-50.

21. Pandolfo, A. G.; Hollenkamp, A. F., Carbon properties and their role in supercapacitors. *Journal of Power Sources* **2006,** *157* (1), 11-27.

22. Simon, P.; Gogotsi, Y., Capacitive Energy Storage in Nanostructured Carbon-Electrolyte Systems. *Accounts of Chemical Research* **2013,** *46* (5), 1094-1103.

23. Rajput, N. N.; Monk, J.; Singh, R.; Hung, F. R., On the Influence of Pore Size and Pore Loading on Structural and Dynamical Heterogeneities of an Ionic Liquid Confined in a Slit Nanopore. *Journal of Physical Chemistry C* **2012,** *116* (8), 5170-5182.

24. Rajput, N. N.; Monk, J.; Hung, F. R., Structure and Dynamics of an Ionic Liquid Confined Inside a Charged Slit Graphitic Nanopore. *Journal of Physical Chemistry C* **2012,** *116* (27), 14504-14513.

25. Singh, R.; Monk, J.; Hung, F. R., Heterogeneity in the Dynamics of the Ionic Liquid BMIM+ PF6- Confined in a Slit Nanopore. *Journal of Physical Chemistry C* **2011,** *115* (33), 16544-16554.

26. Sha, M.; Wu, G.; Liu, Y.; Tang, Z.; Fang, H., Drastic Phase Transition in Ionic Liquid Dmim CI Confined Between Graphite Walls: New Phase Formation. *Journal of Physical Chemistry C* **2009,** *113* (11), 4618-4622.

27. Wu, P.; Huang, J.; Meunier, V.; Sumpter, B. G.; Qiao, R., Voltage Dependent Charge Storage Modes and Capacity in Subnanometer Pores. *Journal of Physical Chemistry Letters* **2012,** *3* (13), 1732-1737.

28. Shim, Y.; Jung, Y.; Kim, H. J., Graphene-Based Supercapacitors: A Computer Simulation Study. *Journal of Physical Chemistry C* **2011,** *115* (47), 23574-23583.

29. Singh, R.; Monk, J.; Hung, F. R., A Computational Study of the Behavior of the Ionic Liquid BMIM+ PF6- Confined Inside Multiwalled Carbon Nanotubes. *Journal of Physical Chemistry C* **2010,** *114* (36), 15478-15485.

30. Aparicio, S.; Atilhan, M., Choline-Based Ionic Liquids on Graphite Surfaces and Carbon Nanotubes Solvation: A Molecular Dynamics Study. *Journal of Physical Chemistry C* **2012,** *116* (22), 12055-12065.

31. Frolov, A. I.; Kirchner, K.; Kirchner, T.; Fedorov, M. V., Molecular-scale insights into the mechanisms of ionic liquids interactions with carbon nanotubes. *Faraday Discussions* **2012,** *154*, 235-247.

32. Dou, Q.; Sha, M.; Fu, H.; Wu, G., Melting Transition of Ionic Liquid bmim PF6 Crystal Confined in Nanopores: A Molecular Dynamics Simulation. *Journal of Physical Chemistry C* **2011,** *115* (39), 18946-18951.

33. Shim, Y.; Kim, H. J., Solvation of Carbon Nanotubes in a Room-Temperature Ionic Liquid. *Acs Nano* **2009,** *3* (7), 1693-1702.

34. Shim, Y.; Kim, H. J., Nanoporous Carbon Supercapacitors in an Ionic Liquid: A Computer Simulation Study. *Acs Nano* **2010,** *4* (4), 2345-2355.

35. Ganesh, P.; Kent, P. R. C.; Mochalin, V., Formation, characterization, and dynamics of onion-like carbon structures for electrical energy storage from nanodiamonds using reactive force fields. *Journal of Applied Physics* **2011,** *110* (7).

36. Li, S.; Feng, G.; Fulvio, P. F.; Hillesheim, P. C.; Liao, C.; Dai, S.; Cummings, P. T., Molecular Dynamics Simulation Study of the Capacitive Performance of a Binary Mixture of Ionic Liquids near an Onion-like Carbon Electrode. *Journal of Physical Chemistry Letters* **2012,** *3* (17), 2465-2469.

37. Feng, G.; Jiang, D.-e.; Cummings, P. T., Curvature Effect on the Capacitance of Electric Double Layers at Ionic Liquid/Onion-Like Carbon Interfaces. *Journal of Chemical Theory and Computation* **2012,** *8* (3), 1058-1063.

38. McDonough, J. K.; Frolov, A. I.; Presser, V.; Niu, J.; Miller, C. H.; Ubieto, T.; Fedorov, M. V.; Gogotsi, Y., Influence of the structure of carbon onions on their electrochemical performance in supercapacitor electrodes. *Carbon* **2012,** *50* (9), 3298-3309.

39. Soolo, E.; Brandell, D.; Liivat, A.; Kasemaegi, H.; Tamm, T.; Aabloo, A., Molecular dynamics simulations of EMI-BF4 in nanoporous carbon actuators. *Journal of Molecular Modeling* **2012,** *18* (4), 1541-1552.

40. Merlet, C.; Rotenberg, B.; Madden, P. A.; Taberna, P.-L.; Simon, P.; Gogotsi, Y.; Salanne, M., On the molecular origin of supercapacitance in nanoporous carbon electrodes. *Nature Materials* **2012,** *11* (4), 306-310.

41. Monk, J.; Singh, R.; Hung, F. R., Effects of Pore Size and Pore Loading on the Properties of Ionic Liquids Confined Inside Nanoporous CMK-3 Carbon Materials. *Journal of Physical Chemistry C* **2011,** *115* (7), 3034-3042.

42. Chmiola, J.; Yushin, G.; Gogotsi, Y.; Portet, C.; Simon, P.; Taberna, P. L., Anomalous increase in carbon capacitance at pore sizes less than 1 nanometer. *Science* **2006,** *313* (5794), 1760-1763.

43. Chmiola, J.; Yushin, G.; Dash, R.; Gogotsi, Y., Effect of pore size and surface area of carbide derived carbons on specific capacitance. *Journal of Power Sources* **2006,** *158* (1), 765-772.

44. Janes, A.; Permann, L.; Arulepp, M.; Lust, E., Electrochemical characteristics of nanoporous carbide-derived carbon materials in non-aqueous electrolyte solutions. *Electrochemistry Communications* **2004,** *6* (3), 313-318.

45. Tesfai, A.; El-Zahab, B.; Bwambok, D. K.; Baker, G. A.; Fakayode, S. O.; Lowry, M.; Warner, I. M., Controllable formation of ionic liquid micro- and nanoparticles via a melt-emulsion-quench approach. *Nano Letters* **2008,** *8* (3), 897-901.

46. Tesfai, A.; El-Zahab, B.; Kelley, A. T.; Li, M.; Garno, J. C.; Baker, G. A.; Warner, I. M., Magnetic and Nonmagnetic Nanoparticles from a Group of Uniform Materials Based on Organic Salts. *ACS Nano* **2009,** *3* (10), 3244-3250.

47. Bwambok, D. K.; El-Zahab, B.; Challa, S. K.; Li, M.; Chandler, L.; Baker, G. A.; Warner, I. M., Near-Infrared Fluorescent NanoGUMBOS for Biomedical Imaging. *Acs Nano* **2009,** *3* (12), 3854-3860.

48. Das, S.; Bwambok, D.; El-Zahab, B.; Monk, J.; de Rooy, S. L.; Challa, S.; Li, M.; Hung, F. R.; Baker, G. A.; Warner, I. M., Nontemplated Approach to Tuning the Spectral Properties of Cyanine-Based Fluorescent NanoGUMBOS. *Langmuir* **2010,** *26* (15), 12867-12876.

49. Dumke, J. C.; El-Zahab, B.; Challa, S.; Das, S.; Chandler, L.; Tolocka, M.; Hayes, D. J.; Warner, I. M., Lanthanide-Based Luminescent NanoGUMBOS. *Langmuir* **2010,** *26* (19), 15599-15603.

50. Vereda, F.; de Vicente, J.; Hidalgo-Alvarez, R., Physical Properties of Elongated Magnetic Particles: Magnetization and Friction Coefficient Anisotropies. *Chemphyschem* **2009,** *10* (8), 1165-1179.

51. Sun, L.; Hao, Y.; Chien, C. L.; Searson, P. C., Tuning the properties of magnetic nanowires. *Ibm Journal of Research and Development* **2005,** *49* (1), 79-102.

52. Day, E. S.; Morton, J. G.; West, J. L., Nanoparticles for Thermal Cancer Therapy. *Journal of Biomechanical Engineering-Transactions of the Asme* **2009,** *131* (7).

53. Fortin, J.-P.; Wilhelm, C.; Servais, J.; Menager, C.; Bacri, J.-C.; Gazeau, F., Size-sorted anionic iron oxide nanomagnets as colloidal mediators for magnetic hyperthermia. *Journal of the American Chemical Society* **2007,** *129* (9), 2628-2635.

54. Hergt, R.; Dutz, S.; Mueller, R.; Zeisberger, M., Magnetic particle hyperthermia: nanoparticle magnetism and materials development for cancer therapy. *Journal of Physics-Condensed Matter* **2006,** *18* (38), S2919-S2934.

55. Gupta, A. K.; Gupta, M., Synthesis and surface engineering of iron oxide nanoparticles for biomedical applications. *Biomaterials* **2005,** *26* (18), 3995-4021.

56. Boisselier, E.; Astruc, D., Gold nanoparticles in nanomedicine: preparations, imaging, diagnostics, therapies and toxicity. *Chemical Society Reviews* **2009,** *38* (6), 1759-1782.

57. Huang, X. H.; El-Sayed, I. H.; Qian, W.; El-Sayed, M. A., Cancer cell imaging and photothermal therapy in the near-infrared region by using gold nanorods. *Journal of the American Chemical Society* **2006,** *128* (6), 2115-2120.

58. Mornet, S.; Vasseur, S.; Grasset, F.; Veverka, P.; Goglio, G.; Demourgues, A.; Portier, J.; Pollert, E.; Duguet, E., Magnetic nanoparticle design for medical applications. *Progress in Solid State Chemistry* **2006,** *34* (2-4), 237-247.

59. Neouze, M.-A.; Le Bideau, J.; Gaveau, P.; Bellayer, S.; Vioux, A., Ionogels, new materials arising from the confinement of ionic liquids within silica-derived networks. *Chemistry of Materials* **2006,** *18* (17), 3931-3936.

60. Le Bideau, J.; Gaveau, P.; Bellayer, S.; Neouze, M. A.; Vioux, A., Effect of confinement on ionic liquids dynamics in monolithic silica ionogels: H-1 NMR study. *Physical Chemistry Chemical Physics* **2007,** *9* (40), 5419-5422.

61. Lunstroot, K.; Driesen, K.; Nockemann, P.; Van Hecke, K.; Van Meervelt, L.; Goerller-Walrand, C.; Binnemans, K.; Bellayer, S.; Viau, L.; Le Bideau, J.; Vioux, A., Lanthanide-doped luminescent ionogels. *Dalton Transactions* **2009,** (2), 298-306.

62. Lunstroot, K.; Driesen, K.; Nockemann, P.; Gorller-Walrand, C.; Binnemans, K.; Bellayer, S.; Le Bideau, J.; Vioux, A., Luminescent ionogels based on europium-doped ionic liquids confined within silica-derived networks. *Chemistry of Materials* **2006,** *18* (24), 5711-5715.

63. Le Bideau, J.; Viau, L.; Vioux, A., Ionogels, ionic liquid based hybrid materials. *Chemical Society Reviews* **2011,** *40* (2), 907-925.

64. de Rooy, S. L.; El-Zahab, B.; Li, M.; Das, S.; Broering, E.; Chandler, L.; Warner, I. M., Fluorescent one-dimensional nanostructures from a group of uniform materials based on organic salts. *Chemical Communications* **2011,** *47* (31), 8916-8918.

65. Pruppacher, H. R.; Klett, J. D., *Microphysics of Clouds and Precipitation*. Kluwer Academic Publishers: The Netherlands, 1997.

66. Abraham, F. F., *Homogeneous nucleation theory: the pretransition theory of vapor condensation*. Academic Press: 1974.

67. Auer, S.; Frenkel, D., Prediction of absolute crystal-nucleation rate in hard-sphere colloids. *Nature* **2001,** *409* (6823), 1020-1023.

68. Dillmann, A.; Meier, G. E. A., A REFINED DROPLET APPROACH TO THE PROBLEM OF HOMOGENEOUS NUCLEATION FROM THE VAPOR-PHASE. *Journal of Chemical Physics* **1991,** *94* (5), 3872-3884.

69. Dillmann, A.; Meier, G. E. A., HOMOGENEOUS NUCLEATION OF SUPERSATURATED VAPORS. *Chemical Physics Letters* **1989,** *160* (1), 71-74.

70. Ford, I. J.; Laaksonen, A.; Kulmala, M., MODIFICATION OF THE DILLMANN-MEIER THEORY OF HOMOGENEOUS NUCLEATION. *Journal of Chemical Physics* **1993,** *99* (1), 764-765.

71. Chiang, P. P.; Donohue, M. D.; Katz, J. L., A KINETIC APPROACH TO CRYSTALLIZATION FROM IONIC SOLUTION .2. CRYSTAL NUCLEATION. *Journal of Colloid and Interface Science* **1988,** *122* (1), 251-265.

72. Girshick, S. L.; Chiu, C. P., KINETIC NUCLEATION THEORY - A NEW EXPRESSION FOR THE RATE OF HOMOGENEOUS NUCLEATION FROM AN IDEAL SUPERSATURATED VAPOR. *Journal of Chemical Physics* **1990,** *93* (2), 1273-1277.

73. Gelb, L. D.; Gubbins, K. E.; Radhakrishnan, R.; Sliwinska-Bartkowiak, M., Phase separation in confined systems. *Reports on Progress in Physics* **1999,** *62* (12), 1573-1659.

74. Overloop, K.; Vangerven, L., FREEZING PHENOMENA IN ADSORBED WATER AS STUDIED BY NMR. *Journal of Magnetic Resonance Series A* **1993,** *101* (2), 179-187.

75. Morishige, K.; Kawano, K., Freezing and melting of water in a single cylindrical pore: The pore-size dependence of freezing and melting behavior. *Journal of Chemical Physics* **1999,** *110* (10), 4867-4872.

76. Morishige, K.; Shikimi, M., Adsorption hysteresis and pore critical temperature in a single cylindrical pore. *Journal of Chemical Physics* **1998,** *108* (18), 7821-7824.

77. Sliwinska-Bartkowiak, M.; Gras, J.; Sikorski, R.; Radhakrishnan, R.; Gelb, L.; Gubbins, K. E., Phase transitions in pores: Experimental and simulation studies of melting and freezing. *Langmuir* **1999,** *15* (18), 6060-6069.

78. Iiyama, T.; Nishikawa, K.; Otowa, T.; Kaneko, K., AN ORDERED WATER MOLECULAR ASSEMBLY STRUCTURE IN A SLIT-SHAPED CARBON NANOSPACE. *Journal of Physical Chemistry* **1995,** *99* (25), 10075-10076.

79. Iiyama, T.; Nishikawa, K.; Suzuki, T.; Kaneko, K., Study of the structure of a water molecular assembly in a hydrophobic nanospace at low temperature with in situ X-ray diffraction. *Chemical Physics Letters* **1997,** *274* (1-3), 152-158.

80. Klein, J.; Kumacheva, E., CONFINEMENT-INDUCED PHASE-TRANSITIONS IN SIMPLE LIQUIDS. *Science* **1995,** *269* (5225), 816-819.

81. Watanabe, A.; Iiyama, T.; Kaneko, K., Melting temperature elevation of benzene confined in graphitic micropores. *Chemical Physics Letters* **1999,** *305* (1-2), 71-74.

82. Booth, H. F.; Strange, J. H., Organic nanocrystals: an NMR study of cyclohexane in porous silica. *Molecular Physics* **1998,** *93* (2), 263-269.

83. Lupi, L.; Hudait, A.; Molinero, V., Heterogeneous Nucleation of Ice on Carbon Surfaces. *Journal of the American Chemical Society* **2014,** *136* (8), 3156-3164.

84. Lopes, J. N. C.; Deschamps, J.; Padua, A. A. H., Modeling ionic liquids using a systematic all-atom force field. *Journal of Physical Chemistry B* **2004,** *108* (6), 2038-2047.

85. Lopes, J. N. C.; Padua, A. A. H., Molecular force field for ionic liquids composed of triflate or bistriflylimide anions. *Journal of Physical Chemistry B* **2004,** *108* (43), 16893-16898.

86. Canongia Lopes, J. N.; Padua, A. A. H., Molecular force field for ionic liquids III: Imidazolium, pyridinium, and phosphonium cations; Chloride, bromide, and dicyanamide anions. *Journal of Physical Chemistry B* **2006,** *110* (39), 19586-19592.

87. Lopes, J. N. C.; Padua, A. A. H.; Shimizu, K., Molecular force field for ionic liquids IV: Trialkylimidazolium and alkoxycarbonyl-imidazolium cations; alkylsulfonate and alkylsulfate anions. *Journal of Physical Chemistry B* **2008,** *112* (16), 5039-5046.

88. Shimizu, K.; Almantariotis, D.; Gomes, M. F. C.; Padua, A. A. H.; Lopes, J. N. C., Molecular Force Field for Ionic Liquids V: Hydroxyethylimidazolium, Dimethoxy-2-Methylimidazolium, and Fluoroalkylimidazolium Cations and Bis(Fluorosulfonyl)Amide, Perfluoroalkanesulfonylamide, and Fluoroalkylfluorophosphate Anions. *Journal of Physical Chemistry B* **2010,** *114* (10), 3592-3600.

89. Vatamanu, J.; Borodin, O.; Smith, G. D., Molecular Insights into the Potential and Temperature Dependences of the Differential Capacitance of a Room-Temperature Ionic Liquid at Graphite Electrodes. *Journal of the American Chemical Society* **2010,** *132* (42), 14825-14833.

90. Vatamanu, J.; Borodin, O.; Bedrov, D.; Smith, G. D., Molecular Dynamics Simulation Study of the Interfacial Structure and Differential Capacitance of Alkylimidazolium Bis(trifluoromethanesulfonyl)imide C(n)mim TFSI Ionic Liquids at Graphite Electrodes. *Journal of Physical Chemistry C* **2012,** *116* (14), 7940-7951.

91. Jayaraman, S.; Maginn, E. J., Computing the melting point and thermodynamic stability of the orthorhombic and monoclinic crystalline polymorphs of the ionic liquid 1-n-butyl-3-methylimidazolium chloride. *Journal of Chemical Physics* **2007,** *127* (21).

92. Morrow, T. I.; Maginn, E. J., Molecular dynamics study of the ionic liquid 1-n-butyl-3-methylimidazolium hexafluorophosphate. *Journal of Physical Chemistry B* **2002,** *106* (49), 12807-12813.

93. Bhargava, B. L.; Balasubramanian, S.; Klein, M. L., Modelling room temperature ionic liquids. *Chemical Communications* **2008,** (29), 3339-3351.

94. Koddermann, T.; Paschek, D.; Ludwig, R., Molecular dynamic simulations of ionic liquids: A reliable description of structure, thermodynamics and dynamics. *Chemphyschem* **2007,** *8* (17), 2464-2470.

95. Sambasivarao, S. V.; Acevedo, O., Development of OPLS-AA Force Field Parameters for 68 Unique Ionic Liquids. *Journal of Chemical Theory and Computation* **2009,** *5* (4), 1038-1050.

96. Bedrov, D.; Borodin, O.; Li, Z.; Smith, G. D., Influence of Polarization on Structural, Thermodynamic, and Dynamic Properties of Ionic Liquids Obtained from Molecular Dynamics Simulations. *Journal of Physical Chemistry B* **2010,** *114* (15), 4984-4997.

97. Bedrov, D.; Borodin, O., Thermodynamic, Dynamic, and Structural Properties of Ionic Liquids Comprised of 1-Butyl-3-methylimidazolium Cation and Nitrate, Azide, or Dicyanamide Anions. *Journal of Physical Chemistry B* **2010,** *114* (40), 12802-12810.

98. Borodin, O., Polarizable Force Field Development and Molecular Dynamics Simulations of Ionic Liquids. *Journal of Physical Chemistry B* **2009,** *113* (33), 11463-11478.

99. Borodin, O.; Gorecki, W.; Smith, G. D.; Armand, M., Molecular Dynamics Simulation and Pulsed-Field Gradient NMR Studies of Bis(fluorosulfonyl)imide (FSI) and Bis (trifluoromethyl)sulfonyl imide (TFSI)-Based Ionic Liquids. *Journal of Physical Chemistry B* **2010,** *114* (20), 6786-6798.

100. Maginn, E. J., Atomistic simulation of the thermodynamic and transport properties of ionic liquids. *Accounts of Chemical Research* **2007,** *40* (11), 1200-1207.

101. Maginn, E. J., Molecular simulation of ionic liquids: current status and future opportunities. *Journal of Physics-Condensed Matter* **2009,** *21* (37).

102. Yan, T.; Wang, Y.; Knox, C., On the Dynamics of Ionic Liquids: Comparisons between Electronically Polarizable and Nonpolarizable Models II. *Journal of Physical Chemistry B* **2010,** *114* (20), 6886-6904.

103. Yan, T.; Wang, Y.; Knox, C., On the Structure of Ionic Liquids: Comparisons between Electronically Polarizable and Nonpolarizable Models I. *Journal of Physical Chemistry B* **2010,** *114* (20), 6905-6921.

104. Hooper, J. B.; Borodin, O., Molecular dynamics simulations of N,N,N,N-tetramethylammonium dicyanamide plastic crystal and liquid using a polarizable force field. *Physical Chemistry Chemical Physics* **2010,** *12* (18), 4635-4643.

105. Armand, M.; Endres, F.; MacFarlane, D. R.; Ohno, H.; Scrosati, B., Ionic-liquid materials for the electrochemical challenges of the future. *Nature Materials* **2009,** *8* (8), 621-629.

106. Arbizzani, C.; Biso, M.; Cericola, D.; Lazzari, M.; Soavi, F.; Mastragostino, M., Safe, high-energy supercapacitors based on solvent-free ionic liquid electrolytes. *Journal of Power Sources* **2008,** *185* (2), 1575-1579.

107. Largeot, C.; Portet, C.; Chmiola, J.; Taberna, P. L.; Gogotsi, Y.; Simon, P., Relation between the ion size and pore size for an electric double-layer capacitor. *Journal of the American Chemical Society* **2008,** *130* (9), 2730-2731.

108. Lin, R.; Huang, P.; Segalini, J.; Largeot, C.; Taberna, P. L.; Chmiola, J.; Gogotsi, Y.; Simon, P., Solvent effect on the ion adsorption from ionic liquid electrolyte into sub-nanometer carbon pores. *Electrochimica Acta* **2009,** *54* (27), 7025-7032.

109. Choi, N. S.; Chen, Z. H.; Freunberger, S. A.; Ji, X. L.; Sun, Y. K.; Amine, K.; Yushin, G.; Nazar, L. F.; Cho, J.; Bruce, P. G., Challenges Facing Lithium Batteries and Electrical Double-Layer Capacitors. *Angewandte Chemie-International Edition* **2012,** *51* (40), 9994-10024.

110. Orita, A.; Kamijima, K.; Yoshida, M., Allyl-functionalized ionic liquids as electrolytes for electric double-layer capacitors. *Journal of Power Sources* **2010,** *195* (21), 7471-7479.

111. Matsumoto, K.; Hagiwara, R., Electrochemical Properties of the Ionic Liquid 1-Ethyl-3-methylimidazolium Difluorophosphate as an Electrolyte for Electric Double-Layer Capacitors. *Journal of The Electrochemical Society* **2010,** *157* (5), A578-A581.

112. Zhai, Y. P.; Dou, Y. Q.; Zhao, D. Y.; Fulvio, P. F.; Mayes, R. T.; Dai, S., Carbon Materials for Chemical Capacitive Energy Storage. *Advanced Materials* **2011,** *23* (42), 4828-4850.

113. Chakrabarti, M. H.; Mjalli, F. S.; AiNashef, I. M.; Hashim, M. A.; Hussain, M. A.; Bahadori, L.; Low, C. T. J., Prospects of applying ionic liquids and deep eutectic solvents for renewable energy storage by means of redox flow batteries. *Renewable & Sustainable Energy Reviews* **2014,** *30*, 254-270.

114. Hagfeldt, A.; Boschloo, G.; Sun, L.; Kloo, L.; Pettersson, H., Dye-Sensitized Solar Cells. *Chemical Reviews* **2010,** *110* (11), 6595-6663.

115. Cao, Y.; Zhang, J.; Bai, Y.; Li, R.; Zakeeruddin, S. M.; GraÌˆtzel, M.; Wang, P., Dye-Sensitized Solar Cells with Solvent-Free Ionic Liquid Electrolytes. *The Journal of Physical Chemistry C* **2008,** *112* (35), 13775-13781.

116. Ito, S.; Zakeeruddin, S. M.; Comte, P.; Liska, P.; Kuang, D.; Gratzel, M., Bifacial dye-sensitized solar cells based on an ionic liquid electrolyte. *Nat Photon* **2008,** *2* (11), 693-698.

117. Kuang, D.; Wang, P.; Ito, S.; Zakeeruddin, S. M.; GrÃ¤tzel, M., Stable Mesoscopic Dye-Sensitized Solar Cells Based on Tetracyanoborate Ionic Liquid Electrolyte. *Journal of the American Chemical Society* **2006,** *128* (24), 7732-7733.

118. Kuang, D.; Uchida, S.; Humphry-Baker, R.; Zakeeruddin, S. M.; Grätzel, M., Organic Dye-Sensitized Ionic Liquid Based Solar Cells: Remarkable Enhancement in Performance through Molecular Design of Indoline Sensitizers. *Angewandte Chemie International Edition* **2008,** *47* (10), 1923-1927.

119. MacFarlane, D. R.; Tachikawa, N.; Forsyth, M.; Pringle, J. M.; Howlett, P. C.; Elliott, G. D.; Davis, J. H.; Watanabe, M.; Simon, P.; Angell, C. A., Energy applications of ionic liquids. *Energy & Environmental Science* **2014,** *7* (1), 232-250.

120. Burt, R.; Birkett, G.; Zhao, X. S., A review of molecular modelling of electric double layer capacitors. *Physical Chemistry Chemical Physics* **2014,** *16* (14), 6519-6538.

121. Fedorov, M. V.; Kornyshev, A. A., Ionic Liquids at Electrified Interfaces. *Chemical Reviews* **2014,** *114* (5), 2978-3036.

122. Kornyshev, A. A.; Qiao, R., Three-Dimensional Double Layers. *The Journal of Physical Chemistry C* **2014,** *118* (32), 18285-18290.

123. Ike, I. S.; Sigalas, I.; Iyuke, S.; Ozoemena, K. I., An overview of mathematical modeling of electrochemical supercapacitors/ultracapacitors. *Journal of Power Sources* **2015,** *273*, 264-277.

124. Tesfai, A. E.-Z., B.; Bwambok, D. K.; Baker, G. A.; Fakayode, S. O.; Lowry, M.; Warner, I. M. , Controllable Formation of Ionic Liquid Micro- and Nanoparticles via a Melt-Emulsion-Quench Approach. *Nano Lett.* **2008,** *8*, 897-901

125. Das, S.; Bwambok, D.; Ei-Zahab, B.; Monk, J.; de Rooy, S. L.; Challa, S.; Li, M.; Hung, F. R.; Baker, G. A.; Warner, I. M., Nontemplated Approach to Tuning the Spectral Properties of Cyanine-Based Fluorescent NanoGUMBOS. *Langmuir* **2010,** *26* (15), 12867-12876.

126. Regmi, B. P.; Monk, J.; El-Zahab, B.; Das, S.; Hung, F. R.; Hayes, D. J.; Warner, I. M., A novel composite film for detection and molecular weight determination of organic vapors. *Journal of Materials Chemistry* **2012,** *22* (27), 13732-13741.

127. Lunstroot, K.; Driesen, K.; Nockemann, P.; Van Hecke, K.; Van Meervelt, L.; Gorller-Walrand, C.; Binnemans, K.; Bellayer, S.; Viau, L.; Le Bideau, J.; Vioux, A., Lanthanide-doped luminescent ionogels. *Dalton Transactions* **2009,** (2), 298-306.

128. Néouze, M.-A.; Bideau, J. L.; Gaveau, P.; Bellayer, S. v.; Vioux, A., Ionogels, New Materials Arising from the Confinement of Ionic Liquids within Silica-Derived Networks. *Chemistry of Materials* **2006,** *18* (17), 3931-3936.

129. Lu, A. H.; Schuth, F., Nanocasting: A versatile strategy for creating nanostructured porous materials. *Advanced Materials* **2006,** *18* (14), 1793-1805.

130. Joo, S. H.; Choi, S. J.; Oh, I.; Kwak, J.; Liu, Z.; Terasaki, O.; Ryoo, R., Ordered nanoporous arrays of carbon supporting high dispersions of platinum nanoparticles. *Nature* **2001,** *412* (6843), 169-172.

131. Jun, S.; Joo, S. H.; Ryoo, R.; Kruk, M.; Jaroniec, M.; Liu, Z.; Ohsuna, T.; Terasaki, O., Synthesis of new, nanoporous carbon with hexagonally ordered mesostructure. *Journal of the American Chemical Society* **2000,** *122* (43), 10712-10713.

132. Lee, J.; Yoon, S.; Hyeon, T.; Oh, S. M.; Kim, K. B., Synthesis of a new mesoporous carbon and its application to electrochemical double-layer capacitors. *Chemical Communications* **1999,** (21), 2177-2178.

133. Joo, S. H.; Choi, S. J.; Oh, I.; Kwak, J.; Liu, Z.; Terasaki, O.; Ryoo, R., Ordered nanoporous arrays of carbon supporting high dispersions of platinum nanoparticles (vol 412, pg 169, 2001). *Nature* **2001,** *414* (6862), 470-470.

134. Fuertes, A. B.; Pico, F.; Rojo, J. M., Influence of pore structure on electric double-layer capacitance of template mesoporous carbons. *Journal of Power Sources* **2004,** *133* (2), 329-336.

135. Lee, J.; Kim, J.; Hyeon, T., Recent progress in the synthesis of porous carbon materials. *Advanced Materials* **2006,** *18* (16), 2073-2094.

136. Su, D. S.; Schlogl, R., Nanostructured Carbon and Carbon Nanocomposites for Electrochemical Energy Storage Applications. *Chemsuschem* **2010,** *3* (2), 136-168.

137. Zhang, L. L.; Zhao, X. S., Carbon-based materials as supercapacitor electrodes. *Chemical Society Reviews* **2009,** *38* (9), 2520-2531.

138. Liu, C.; Li, F.; Ma, L. P.; Cheng, H. M., Advanced Materials for Energy Storage. *Advanced Materials* **2010,** *22* (8), E28-+.

139. Hess, B.; Kutzner, C.; van der Spoel, D.; Lindahl, E., GROMACS 4: Algorithms for Highly Efficient, Load-Balanced, and Scalable Molecular Simulation. *Journal of Chemical Theory and Computation* **2008,** *4* (3), 435-447.

140. Fredlake, C. P.; Crosthwaite, J. M.; Hert, D. G.; Aki, S.; Brennecke, J. F., Thermophysical properties of imidazolium-based ionic liquids. *Journal of Chemical and Engineering Data* **2004,** *49* (4), 954-964.

141. Dommert, F.; Wendler, K.; Berger, R.; Delle Site, L.; Holm, C., Force Fields for Studying the Structure and Dynamics of Ionic Liquids: A Critical Review of Recent Developments. *Chemphyschem* **2012,** *13* (7), 1625-1637.

142. Maginn, E. J., Molecular simulation of ionic liquids: current status and future opportunities. *Journal of Physics-Condensed Matter* **2009,** *21* (37), 373101.

143. Bhargava, B. L.; Balasubramanian, S., Dynamics in a room-temperature ionic liquid: A computer simulation study of 1,3-dimethylimidazolium chloride. *The Journal of Chemical Physics* **2005,** *123* (14), -.

144. Kowsari, M. H.; Alavi, S.; Ashrafizaadeh, M.; Najafi, B., Molecular dynamics simulation of imidazolium-based ionic liquids. I. Dynamics and diffusion coefficient. *Journal of Chemical Physics* **2008,** *129* (22), 224508.

145. Fannin, A. A.; Floreani, D. A.; King, L. A.; Landers, J. S.; Piersma, B. J.; Stech, D. J.; Vaughn, R. L.; Wilkes, J. S.; Williams, J. L., PROPERTIES OF 1,3-DIALKYLIMIDAZOLIUM CHLORIDE ALUMINUM-CHLORIDE IONIC LIQUIDS .2. PHASE-TRANSITIONS, DENSITIES, ELECTRICAL CONDUCTIVITIES, AND VISCOSITIES. *Journal of Physical Chemistry* **1984,** *88* (12), 2614-2621.

146. Jain, S. K., Molecular modeling of microporous and templated mesoporous carbons. *Ph.D Thesis, North Carolina State University, (http://www.lib.ncsu.edu/resolver/1840.16/4386)* **2008**.

147. Hung, F. R.; Bhattacharya, S.; Coasne, B.; Thommes, M.; Gubbins, K. E., Argon and krypton adsorption on templated mesoporous silicas: molecular simulation and experiment. *Adsorption-Journal of the International Adsorption Society* **2007,** *13* (5-6), 425-437.

148. Coasne, B.; Hung, F. R.; Pellenq, R. J. M.; Siperstein, F. R.; Gubbins, K. E., Adsorption of Simple Gases in MCM-41 Materials:â€‰ The Role of Surface Roughness. *Langmuir* **2005,** *22* (1), 194-202.

149. Bhattacharya, S.; Coasne, B.; Hung, F. R.; Gubbins, K. E., Modeling Micelle-Templated Mesoporous Material SBA-15: Atomistic Model and Gas Adsorption Studies. *Langmuir* **2009,** *25* (10), 5802-5813.

150. Brenner, D. W., Empirical potential for hydrocarbons for use in simulating the chemical vapor deposition of diamond films. *Physical Review B* **1990,** *42* (15), 9458-9471.

151. Pellenq, R. J. M.; Nicholson, D., Intermolecular Potential Function for the Physical Adsorption of Rare Gases in Silicalite. *The Journal of Physical Chemistry* **1994,** *98* (50), 13339-13349.

152. Gelb, L. D.; Gubbins, K. E., Pore Size Distributions in Porous Glasses:â€‰ A Computer Simulation Study. *Langmuir* **1998,** *15* (2), 305-308.

153. Thomson, K. T.; Gubbins, K. E., Modeling Structural Morphology of Microporous Carbons by Reverse Monte Carlo. *Langmuir* **2000,** *16* (13), 5761-5773.

154. Turner, C. H.; Pikunic, J.; Gubbins, K. E., Influence of chemical and physical surface heterogeneity on chemical reaction equilibria in carbon micropores. *Molecular Physics* **2001,** *99* (24), 1991-2001.

155. Palmer, J. C.; Brennan, J. K.; Hurley, M. M.; Balboa, A.; Gubbins, K. E., Detailed structural models for activated carbons from molecular simulation. *Carbon* **2009,** *47* (12), 2904-2913.

156. Rajput, N. N.; Monk, J.; Hung, F. R., Ionic Liquids Confined in a Realistic Activated Carbon Model: A Molecular Simulation Study. *The Journal of Physical Chemistry C* **2014,** *118* (3), 1540-1553.

157. Singh, R.; Monk, J.; Hung, F. R., A computational study of the behavior of the ionic liquid [BMIM+][PF6-] confined inside multi-walled carbon nanotubes. *Journal of Physical Chemistry C* **2010,** *114*, 15478-15485.

158. Singh, R.; Monk, J.; Hung, F. R., Heterogeneity in the Dynamics of the Ionic Liquid BMIM(+) PF(6)(-) Confined in a Slit Nanopore. *Journal of Physical Chemistry C* **2011,** *115* (33), 16544-16554.

159. Rajput, N. N.; Monk, J.; Singh, R.; Hung, F. R., On the Influence of Pore Size and Pore Loading on Structural and Dynamical Heterogeneities of an Ionic Liquid Confined in a Slit Nanopore. *The Journal of Physical Chemistry C* **2012,** *116* (8), 5169-5181.

160. Rajput, N. N.; Monk, J.; Hung, F. R., Structure and Dynamics of an Ionic Liquid Confined Inside a Charged Slit Graphitic Nanopore. *J. Phys. Chem. C* **2012,** *116* (27), 14504-14513.

161. Singh, R.; Rajput, N. N.; He, X.; Monk, J.; Hung, F. R., Molecular dynamics simulations of the ionic liquid [EMIM+][TFMSI-] confined inside rutile (110) slit nanopores. *Physical Chemistry Chemical Physics* **2013,** *15* (38), 16090-16103.

162. Radhakrishnan, R.; Gubbins, K. E., Quasi-one-dimensional phase transitions in nanopores: Pore-pore correlation effects. *Physical review letters* **1997,** *79* (15), 2847.

163. Peterson, B. K.; Gubbins, K. E.; Heffelfinger, G. S.; Marconi, U. M. B.; Vanswol, F., LENNARD-JONES FLUIDS IN CYLINDRICAL PORES - NONLOCAL THEORY AND COMPUTER-SIMULATION. *Journal of Chemical Physics* **1988,** *88* (10), 6487-6500.

164. Menzl, G.; Koefinger, J.; Dellago, C., Phase Transition and Interpore Correlations of Water in Nanopore Membranes. *Physical Review Letters* **2012,** *109* (2), 020602.

165. Kondrat, S.; Wu, P.; Qiao, R.; Kornyshev, A. A., Accelerating charging dynamics in subnanometre pores. *Nat Mater* **2014,** *13* (4), 387-393.

166. Péan, C.; Merlet, C.; Rotenberg, B.; Madden, P. A.; Taberna, P.-L.; Daffos, B.; Salanne, M.; Simon, P., On the Dynamics of Charging in Nanoporous Carbon-Based Supercapacitors. *ACS Nano* **2014,** *8* (2), 1576-1583.

167. Welton, T., Room-temperature ionic liquids. Solvents for synthesis and catalysis. *Chemical Reviews* **1999,** *99* (8), 2071-2083.

168. Swatloski, R. P.; Spear, S. K.; Holbrey, J. D.; Rogers, R. D., Dissolution of cellose with ionic liquids. *Journal of the American Chemical Society* **2002,** *124* (18), 4974-4975.

169. Zhang, S.; Sun, J.; Zhang, X.; Xin, J.; Miao, Q.; Wang, J., Ionic liquid-based green processes for energy production. *Chemical Society reviews* **2014,** *43* (22), 7838-69.

170. Ramdin, M.; de Loos, T. W.; Vlugt, T. J. H., State-of-the-Art of CO2 Capture with Ionic Liquids. *Industrial & Engineering Chemistry Research* **2012,** *51* (24), 8149-8177.

171. Zakeeruddin, S. M.; Graetzel, M., Solvent-Free Ionic Liquid Electrolytes for Mesoscopic Dye-Sensitized Solar Cells. *Advanced Functional Materials* **2009,** *19* (14), 2187-2202.

172. de Rooy, S. L.; Li, M.; Bwambok, D. K.; El-Zahab, B.; Challa, S.; Warner, I. M., Ephedrinium-Based Protic Chiral Ionic Liquids for Enantiomeric Recognition. *Chirality* **2011,** *23* (1), 54-62.

173. Warner, I. M.; El-Zahab, B.; Siraj, N., Perspectives on Moving Ionic Liquid Chemistry into the Solid Phase. *Analytical Chemistry* **2014,** *86* (15), 7184-7191.

174. Li, M.; De Rooy, S. L.; Bwambok, D. K.; El-Zahab, B.; DiTusa, J. F.; Warner, I. M., Magnetic chiral ionic liquids derived from amino acids. *Chemical Communications* **2009,** (45), 6922-6924.

175. Dumke, J. C.; Oureshi, A.; Hamden, S.; El-Zaha, B.; Das, S.; Hayes, D. J.; Boldor, D.; Rupnik, K.; Warner, I. M., Photothermal Response of Near-Infrared-Absorbing NanoGUMBOS. *Applied Spectroscopy* **2014,** *68* (3), 340-352.

176. Dumke, J. C.; Qureshi, A.; Hamdan, S.; Rupnik, K.; El-Zahab, B.; Hayes, D. J.; Warner, I. M., In vitro activity studies of hyperthermal near-infrared nanoGUMBOS in MDA-MB-231 breast cancer cells. *Photochemical & Photobiological Sciences* **2014,** *13* (9), 1270-1280.

177. Vioux, A.; Viau, L.; Volland, S.; Le Bideau, J., Use of ionic liquids in sol-gel; ionogels and applications. *Comptes Rendus Chimie* **2010,** *13* (1-2), 242-255.

178. Ha, J. M.; Hamilton, B. D.; Hillmyer, M. A.; Ward, M. D., Phase Behavior and Polymorphism of Organic Crystals Confined within Nanoscale Chambers. *Crystal Growth & Design* **2009,** *9* (11), 4766-4777.

179. Hamilton, B. D.; Weissbuch, I.; Lahav, M.; Hillmyer, M. A.; Ward, M. D., Manipulating Crystal Orientation in Nanoscale Cylindrical Pores by Stereochemical Inhibition. *Journal of the American Chemical Society* **2009,** *131* (7), 2588-2596.

180. Hamilton, B. D.; Hillmyer, M. A.; Ward, M. D., Glycine polymorphism in nanoscale crystallization chambers. *Crystal Growth & Design* **2008,** *8* (9), 3368-3375.

181. Rengarajan, G. T.; Enke, D.; Steinhart, M.; Beiner, M., Stabilization of the amorphous state of pharmaceuticals in nanopores. *Journal of Materials Chemistry* **2008,** *18* (22), 2537-2539.

182. Beiner, M.; Rengarajan, G. T.; Pankaj, S.; Enke, D.; Steinhart, M., Manipulating the crystalline state of pharmaceuticals by nanoconfinement. *Nano Letters* **2007,** *7* (5), 1381-1385.

183. Diao, Y.; Harada, T.; Myerson, A. S.; Hatton, T. A.; Trout, B. L., The role of nanopore shape in surface-induced crystallization. *Nat Mater* **2011,** *10* (11), 867-871.

184. Debenedetti, P. G., *Metastable Liquids: Concepts and Principles*. Princeton University Press: Princeton, NJ, 1996.

185. Kaschiev, D., *Nucleation: Basic Theory with Applications*. Butterworth-Heinemann: Oxford, 2000.

186. Price, S. L., Computed Crystal Energy Landscapes for Understanding and Predicting Organic Crystal Structures and Polymorphism. *Accounts of Chemical Research* **2008,** *42* (1), 117-126.

187. Erdemir, D.; Lee, A. Y.; Myerson, A. S., Nucleation of Crystals from Solution: Classical and Two-Step Models. *Accounts of Chemical Research* **2009,** *42* (5), 621-629.

188. Vekilov, P. G., Nucleation. *Crystal Growth & Design* **2010,** *10* (12), 5007-5019.

189. Auer, S.; Frenkel, D., Quantitative Prediction of Crystal-Nucleation Rates for Spherical Colloids: A Computational Approach. *Annual Review of Physical Chemistry* **2004,** *55* (1), 333-361.

190. Anwar, J.; Zahn, D., Uncovering Molecular Processes in Crystal Nucleation and Growth by Using Molecular Simulation. *Angewandte Chemie-International Edition* **2011,** *50* (9), 1996-2013.

191. Palmer, J. C.; Debenedetti, P. G., Recent Advances in Molecular Simulation: A Chemical Engineering Perspective. *Aiche Journal* **2015,** *61* (2), 370-383.

192. tenWolde, P. R.; RuizMontero, M. J.; Frenkel, D., Numerical calculation of the rate of crystal nucleation in a Lennard-Jones system at moderate undercooling. *Journal of Chemical Physics* **1996,** *104* (24), 9932-9947.

193. Vehkamäki, H.; Ford, I. J., Critical cluster size and droplet nucleation rate from growth and decay simulations of Lennard-Jones clusters. *The Journal of Chemical Physics* **2000,** *112* (9), 4193-4202.

194. Moroni, D.; ten Wolde, P. R.; Bolhuis, P. G., Interplay between Structure and Size in a Critical Crystal Nucleus. *Physical Review Letters* **2005,** *94* (23), 235703.

195. Trudu, F.; Donadio, D.; Parrinello, M., Freezing of a Lennard-Jones Fluid: From Nucleation to Spinodal Regime. *Physical Review Letters* **2006,** *97* (10), 105701.

196. Desgranges, C.; Delhommelle, J., Insights into the Molecular Mechanism Underlying Polymorph Selection. *Journal of the American Chemical Society* **2006,** *128* (47), 15104-15105.

197. Desgranges, C.; Delhommelle, J., Polymorph selection during the crystallization of Yukawa systems. *The Journal of Chemical Physics* **2007,** *126* (5), 054501.

198. Jungblut, S.; Dellago, C., Heterogeneous crystallization on tiny clusters. *EPL (Europhysics Letters)* **2011,** *96* (5), 56006.

199. Beckham, G. T.; Peters, B., Optimizing Nucleus Size Metrics for Liquid–Solid Nucleation from Transition Paths of Near-Nanosecond Duration. *The Journal of Physical Chemistry Letters* **2011,** *2* (10), 1133-1138.

200. Chkonia, G.; Wölk, J.; Strey, R.; Wedekind, J.; Reguera, D., Evaluating nucleation rates in direct simulations. *The Journal of Chemical Physics* **2009,** *130* (6), 064505.

201. Radhakrishnan, R.; Trout, B. L., Nucleation of Hexagonal Ice (Ih) in Liquid Water. *Journal of the American Chemical Society* **2003,** *125* (25), 7743-7747.

202. Li, T.; Donadio, D.; Russo, G.; Galli, G., Homogeneous ice nucleation from supercooled water. *Physical Chemistry Chemical Physics* **2011,** *13* (44), 19807-19813.

203. Reinhardt, A.; Doye, J. P. K., Free energy landscapes for homogeneous nucleation of ice for a monatomic water model. *The Journal of Chemical Physics* **2012,** *136* (5), 054501.

204. Sanz, E.; Vega, C.; Espinosa, J. R.; Caballero-Bernal, R.; Abascal, J. L. F.; Valeriani, C., Homogeneous Ice Nucleation at Moderate Supercooling from Molecular Simulation. *Journal of the American Chemical Society* **2013,** *135* (40), 15008-15017.

205. Sear, R. P., The non-classical nucleation of crystals: microscopic mechanisms and applications to molecular crystals, ice and calcium carbonate. *International Materials Reviews* **2012,** *57* (6), 328-356.

206. Andrey, V. B.; Jamshed, A.; Ruslan, D.; Richard, H., Challenges in molecular simulation of homogeneous ice nucleation. *Journal of Physics: Condensed Matter* **2008,** *20* (49), 494243.

207. Reinhardt, A.; Doye, J. P. K., Note: Homogeneous TIP4P/2005 ice nucleation at low supercooling. *The Journal of Chemical Physics* **2013,** *139* (9), 096102.

208. Joswiak, M. N.; Duff, N.; Doherty, M. F.; Peters, B., Size-Dependent Surface Free Energy and Tolman-Corrected Droplet Nucleation of TIP4P/2005 Water. *The Journal of Physical Chemistry Letters* **2013,** *4* (24), 4267-4272.

209. Holten, V.; Limmer, D. T.; Molinero, V.; Anisimov, M. A., Nature of the anomalies in the supercooled liquid state of the mW model of water. *The Journal of Chemical Physics* **2013,** *138* (17), 174501.

210. Valeriani, C.; Sanz, E.; Frenkel, D., Rate of homogeneous crystal nucleation in molten NaCl. *The Journal of Chemical Physics* **2005,** *122* (19), -.

211. Quigley, D.; Rodger, P. M., Free energy and structure of calcium carbonate nanoparticles during early stages of crystallization. *The Journal of Chemical Physics* **2008,** *128* (22), 221101.

212. Li, T.; Donadio, D.; Galli, G., Nucleation of tetrahedral solids: A molecular dynamics study of supercooled liquid silicon. *The Journal of Chemical Physics* **2009,** *131* (22), 224519.

213. Yi, P.; Rutledge, G. C., Molecular simulation of crystal nucleation in n-octane melts. *The Journal of Chemical Physics* **2009,** *131* (13), 134902.

214. Saika-Voivod, I.; Poole, P. H.; Bowles, R. K., Test of classical nucleation theory on deeply supercooled high-pressure simulated silica. *The Journal of Chemical Physics* **2006,** *124* (22), 224709.

215. Agarwal, V.; Peters, B., Nucleation near the eutectic point in a Potts-lattice gas model. *The Journal of Chemical Physics* **2014,** *140* (8), 084111.

216. Singh, M.; Dhabal, D.; Nguyen, A. H.; Molinero, V.; Chakravarty, C., Triplet Correlations Dominate the Transition from Simple to Tetrahedral Liquids. *Physical Review Letters* **2014,** *112* (14), 147801.

217. Shah, M.; Santiso, E. E.; Trout, B. L., Computer Simulations of Homogeneous Nucleation of Benzene from the Melt. *Journal of Physical Chemistry B* **2011,** *115* (35), 10400-10412.

218. Giberti, F.; Salvalaglio, M.; Mazzotti, M.; Parrinello, M., Insight into the nucleation of urea crystals from the melt. *Chemical Engineering Science* **2015,** *121* (0), 51-59.

219. Yu, T.-Q.; Chen, P.-Y.; Chen, M.; Samanta, A.; Vanden-Eijnden, E.; Tuckerman, M., Order-parameter-aided temperature-accelerated sampling for the exploration of crystal polymorphism and solid-liquid phase transitions. *Journal of Chemical Physics* **2014,** *140* (21), 214109.

220. Samanta, A.; Tuckerman, M. E.; Yu, T.-Q.; E, W., Microscopic mechanisms of equilibrium melting of a solid. *Science* **2014,** *346* (6210), 729-732.

221. Sha, M. L.; Wu, G. Z.; Fang, H. P.; Zhu, G. L.; Liu, Y. S., Liquid-to-Solid Phase Transition of a 1,3-Dimethylimidazolium Chloride Ionic Liquid Monolayer Confined between Graphite Walls. *Journal of Physical Chemistry C* **2008,** *112* (47), 18584-18587.

222. Sha, M. L.; Wu, G. Z.; Liu, Y. S.; Tang, Z. F.; Fang, H. P., Drastic Phase Transition in Ionic Liquid [Dmim][CI] Confined Between Graphite Walls: New Phase Formation. *Journal of Physical Chemistry C* **2009,** *113* (11), 4618-4622.

223. Pinilla, C.; Del Popolo, M. G.; Lynden-Bell, R. M.; Kohanoff, J., Structure and Dynamics of a Confined Ionic Liquid. Topics of Relevance to Dye-Sensitized Solar Cells. *The Journal of Physical Chemistry B* **2005,** *109* (38), 17922-17927.

224. Pinilla, C.; Del Popolo, M. G.; Kohanoff, J.; Lynden-Bell, R. M., Polarization relaxation in an ionic liquid confined between electrified walls. *Journal of Physical Chemistry B* **2007,** *111* (18), 4877-4884.

225. Youngs, T. G. A.; Hardacre, C., Application of static charge transfer within an ionic-liquid force field and its effect on structure and dynamics. *Chemphyschem* **2008,** *9* (11), 1548-1558.

226. Hanke, C. G.; Atamas, N. A.; Lynden-Bell, R. M., Solvation of small molecules in imidazolium ionic liquids: a simulation study. *Green Chemistry* **2002,** *4* (2), 107-111.

227. Del Popolo, M. G.; Lynden-Bell, R. M.; Kohanoff, J., Ab Initio Molecular Dynamics Simulation of a Room Temperature Ionic Liquid. *The Journal of Physical Chemistry B* **2005,** *109* (12), 5895-5902.

228. Buhl, M.; Chaumont, A.; Schurhammer, R.; Wipff, G., Ab initio molecular dynamics of liquid 1,3-dimethylimidazolium chloride. *Journal of Physical Chemistry B* **2005,** *109* (39), 18591-18599.

229. Ovchinnikov, V.; Karplus, M.; Vanden-Eijnden, E., Free energy of conformational transition paths in biomolecules: The string method and its application to myosin VI. *Journal of Chemical Physics* **2011,** *134* (8), 085103.

230. Maragliano, L.; Fischer, A.; Vanden-Eijnden, E.; Ciccotti, G., String method in collective variables: Minimum free energy paths and isocommittor surfaces. *Journal of Chemical Physics* **2006,** *125* (2), 024106.

231. Vanden-Eijnden, E.; Venturoli, M., Revisiting the finite temperature string method for the calculation of reaction tubes and free energies. *Journal of Chemical Physics* **2009,** *130* (19), 194103.

232. Maragliano, L.; Vanden-Eijnden, E.; Roux, B., Free Energy and Kinetics of Conformational Transitions from Voronoi Tessellated Milestoning with Restraining Potentials. *Journal of Chemical Theory and Computation* **2009,** *5* (10), 2589-2594.

233. Vanden-Eijnden, E.; Venturoli, M., Markovian milestoning with Voronoi tessellations. *The Journal of Chemical Physics* **2009,** *130* (19), 194101.

234. E, W.; Ren, W.; Vanden-Eijnden, E., Simplified and improved string method for computing the minimum energy paths in barrier-crossing events. *Journal of Chemical Physics* **2007,** *126* (16), 164103.

235. Maragliano, L.; Vanden-Eijnden, E., On-the-fly string method for minimum free energy paths calculation. *Chemical Physics Letters* **2007,** *446* (1-3), 182-190.

236. Ren, W.; Vanden-Eijnden, E.; Maragakis, P.; E, W. N., Transition pathways in complex systems: Application of the finite-temperature string method to the alanine dipeptide. *Journal of Chemical Physics* **2005,** *123* (13), 134109.

237. Miller, T. F., III; Vanden-Eijnden, E.; Chandler, D., Solvent coarse-graining and the string method applied to the hydrophobic collapse of a hydrated chain. *Proceedings of the National Academy of Sciences of the United States of America* **2007,** *104* (37), 14559-14564.

238. Bellucci, M. A.; Trout, B. L., Bezier curve string method for the study of rare events in complex chemical systems. *Journal of Chemical Physics* **2014,** *141* (7), 074110.

239. Ovchinnikov, V.; Karplus, M., Investigations of alpha-helix <->beta-sheet transition pathways in a miniprotein using the finite-temperature string method. *Journal of Chemical Physics* **2014,** *140* (17), 175103.

240. Zinovjev, K.; Javier Ruiz-Pernia, J.; Tunon, I., Toward an Automatic Determination of Enzymatic Reaction Mechanisms and Their Activation Free Energies. *Journal of Chemical Theory and Computation* **2013,** *9* (8), 3740-3749.

241. Santiso, E. E.; Trout, B. L., A general set of order parameters for molecular crystals. *Journal of Chemical Physics* **2011,** *134* (6), 064109.

242. Santiso, E. E.; Trout, B. L., A General Method for Molecular Modeling of Nucleation from the Melt. *The Journal of Chemical Physics* **2015**, submitted.

243. Allen, F. H., The Cambridge Structural Database: a quarter of a million crystal structures and rising. *Acta Crystallographica Section B-Structural Science* **2002,** *58*, 380-388.

244. Arduengo, A. J.; Dias, H. V. R.; Harlow, R. L.; Kline, M., ELECTRONIC STABILIZATION OF NUCLEOPHILIC CARBENES. *Journal of the American Chemical Society* **1992,** *114* (14), 5530-5534.

245. Fannin, A. A.; Floreani, D. A.; King, L. A.; Landers, J. S.; Piersma, B. J.; Stech, D. J.; Vaughn, R. L.; Wilkes, J. S.; Williams, J. L., Properties of 1,3-Dialkylimidazolium Chloride Aluminum-Chloride Ionic Liquids .2. Phase-Transitions, Densities, Electrical Cconductivities, and Viscosities. *Journal of Physical Chemistry* **1984,** *88* (12), 2614-2621.

246. Alavi, S.; Thompson, D. L., Molecular dynamics studies of melting and some liquid-state properties of 1-ethyl-3-methylimidazolium hexafluorophosphate emim PF6. *Journal of Chemical Physics* **2005,** *122* (15), 154704.

247. Zhang, Y.; Maginn, E. J., A comparison of methods for melting point calculation using molecular dynamics simulations. *The Journal of Chemical Physics* **2012,** *136* (14), 144116.

248. Phillips, J. C.; Braun, R.; Wang, W.; Gumbart, J.; Tajkhorshid, E.; Villa, E.; Chipot, C.; Skeel, R. D.; Kale, L.; Schulten, K., Scalable molecular dynamics with NAMD. *Journal of Computational Chemistry* **2005,** *26* (16), 1781-1802.

249. Darden, T.; York, D.; Pedersen, L., PARTICLE MESH EWALD - AN N.LOG(N) METHOD FOR EWALD SUMS IN LARGE SYSTEMS. *Journal of Chemical Physics* **1993,** *98* (12), 10089-10092.

250. Hess, B.; Bekker, H.; Berendsen, H. J. C.; Fraaije, J., LINCS: A linear constraint solver for molecular simulations. *Journal of Computational Chemistry* **1997,** *18* (12), 1463-1472.

251. Vanden-Eijnden, E., Some Recent Techniques for Free Energy Calculations. *Journal of Computational Chemistry* **2009,** *30* (11), 1737-1747.

252. Alt, H.; Godau, M., Measuring the resemblance of polygonal curves. In *Proceedings of the eighth annual symposium on Computational geometry*, ACM: Berlin, Germany, 1992; pp 102-109.

253. Alt, H.; Godau, M., Computing the Fréchet Distance Between Two Polygonal Curves. *International Journal of Computational Geometry & Applications* **1995,** *05* (01n02), 75-91.

254. Lankin, A. V.; Norman, G. E.; Stegailov, V. V., Atomistic Simulation of the Interaction of an Electrolyte with Graphite Nanostructures in Perspective Supercapacitors. *High Temperature* **2010,** *48* (6), 837-845.

255. Honeycutt, J. D.; Andersen, H. C., The effect of periodic boundary conditions on homogeneous nucleation observed in computer simulations. *Chemical Physics Letters* **1984,** *108* (6), 535-538.

256. Honeycutt, J. D.; Andersen, H. C., Small system size artifacts in the molecular dynamics simulation of homogeneous crystal nucleation in supercooled atomic liquids. *The Journal of Physical Chemistry* **1986,** *90* (8), 1585-1589.

257. Swope, W. C.; Andersen, H. C., ${10}^{6}$-particle molecular-dynamics study of homogeneous nucleation of crystals in a supercooled atomic liquid. *Physical Review B* **1990,** *41* (10), 7042-7054.

258. Jayaraman, S.; Maginn, E. J., Computing the melting point and thermodynamic stability of the orthorhombic and monoclinic crystalline polymorphs of the ionic liquid 1-n-butyl-3-methylimidazolium chloride. *The Journal of Chemical Physics* **2007,** *127* (21), 214504.

259. Pruppacher, H. R., A NEW LOOK AT HOMOGENEOUS ICE NUCLEATION IN SUPERCOOLED WATER DROPS. *Journal of the Atmospheric Sciences* **1995,** *52* (11), 1924-1933.

260. Taborek, P., NUCLEATION IN EMULSIFIED SUPERCOOLED WATER. *Physical Review B* **1985,** *32* (9), 5902-5906.

261. Sha, M.; Wu, G.; Fang, H.; Zhu, G.; Liu, Y., Liquid-to-Solid Phase Transition of a 1,3-Dimethylimidazolium Chloride Ionic Liquid Monolayer Confined between Graphite Walls. *Journal of Physical Chemistry C* **2008,** *112* (47), 18584-18587.

262. Pinilla, C.; Del Popolo, M. G.; Lynden-Bell, R. M.; Kohanoff, J., Structure and dynamics of a confined ionic liquid. topics of relevance to dye-sensitized solar cells. *Journal of Physical Chemistry B* **2005,** *109* (38), 17922-17927.

263. Pedersen, U. R.; Hummel, F.; Dellago, C., Computing the crystal growth rate by the interface pinning method. *Journal of Chemical Physics* **2015,** *142* (4).

264. Maragliano, L.; Fischer, A.; Vanden-Eijnden, E.; Ciccotti, G., String method in collective variables: Minimum free energy paths and isocommittor surfaces. *Journal of Chemical Physics* **2006,** *125* (2).

265. Vanden-Eijnden, E.; Venturoli, M., Revisiting the finite temperature string method for the calculation of reaction tubes and free energies. *Journal of Chemical Physics* **2009,** *130* (19).

266. Vanden-Eijnden, E.; Venturoli, M., Markovian milestoning with Voronoi tessellations. *Journal of Chemical Physics* **2009,** *130* (19).

267. Ovchinnikov, V.; Karplus, M.; Vanden-Eijnden, E., Free energy of conformational transition paths in biomolecules: The string method and its application to myosin VI. *Journal of Chemical Physics* **2011,** *134* (8).

268. Santiso, E. E.; Trout, B. L., A general set of order parameters for molecular crystals. *Journal of Chemical Physics* **2011,** *134* (6).

269. He, X.; Shen, Y.; Hung, F. R.; Santiso, E. E., Molecular simulation of homogeneous nucleation of crystals of an ionic liquid from the melt. *The Journal of chemical physics* **2015,** *143* (12), 124506-124506.

270. Rogers, R. D.; Seddon, K. R., Ionic liquids - Solvents of the future? *Science* **2003,** *302* (5646), 792-793.

271. Zhao, D. B.; Wu, M.; Kou, Y.; Min, E., Ionic liquids: applications in catalysis. *Catalysis Today* **2002,** *74* (1-2), 157-189.

272. Chiappe, C.; Pieraccini, D., Ionic liquids: solvent properties and organic reactivity. *Journal of Physical Organic Chemistry* **2005,** *18* (4), 275-297.

273. Earle, M. J.; Seddon, K. R., Ionic liquids. Green solvents for the future. *Pure and Applied Chemistry* **2000,** *72* (7), 1391-1398.

274. Rehman, A.; Zeng, X., Ionic liquids as green solvents and electrolytes for robust chemical sensor development. *Accounts of chemical research* **2012,** *45* (10), 1667-77.

275. Shim, Y.; Kim, H. J.; Jung, Y., Graphene-based supercapacitors in the parallel-plate electrode configuration: Ionic liquids versus organic electrolytes. *Faraday Discussions* **2012,** *154*, 249-263.

276. Kawano, R.; Matsui, H.; Matsuyama, C.; Sato, A.; Susan, M.; Tanabe, N.; Watanabe, M., High performance dye-sensitized solar cells using ionic liquids as their electrolytes. *Journal of Photochemistry and Photobiology a-Chemistry* **2004,** *164* (1-3), 87-92.

277. Alba-Simionesco, C.; Coasne, B.; Dosseh, G.; Dudziak, G.; Gubbins, K. E.; Radhakrishnan, R.; Sliwinska-Bartkowiak, M., Effects of confinement on freezing and melting. *Journal of Physics-Condensed Matter* **2006,** *18* (6), R15-R68.

278. Laaksonen, A.; Talanquer, V.; Oxtoby, D. W., NUCLEATION - MEASUREMENTS, THEORY, AND ATMOSPHERIC APPLICATIONS. *Annual Review of Physical Chemistry* **1995,** *46*, 489-524.

279. Price, S. L., Computational prediction of organic crystal structures and polymorphism. *International Reviews in Physical Chemistry* **2008,** *27* (3), 541-568.

280. Zahn, D.; Leoni, S., Nucleation and growth in pressure-induced phase transitions from molecular dynamics simulations: Mechanism of the reconstructive transformation of NaCl to the CsCl-Type structure. *Physical Review Letters* **2004,** *92* (25).

281. Boulfelfel, S. E.; Oganov, A. R.; Leoni, S., Understanding the nature of "superhard graphite". *Scientific Reports* **2012,** *2*.

282. Jungblut, S.; Dellago, C., Heterogeneous crystallization on tiny clusters. *Epl* **2011,** *96* (5).

283. Peters, B.; Trout, B. L., Obtaining reaction coordinates by likelihood maximization. *Journal of Chemical Physics* **2006,** *125* (5), 10.

284. Zahn, D.; Grin, Y.; Leoni, S., Mechanism of the pressure-induced wurtzite to rocksalt transition of CdSe. *Physical Review B* **2005,** *72* (6).

285. Peters, B., Recent advances in transition path sampling: accurate reaction coordinates, likelihood maximisation and diffusive barrier-crossing dynamics. *Molecular Simulation* **2010,** *36* (15), 1265-1281.

286. ten Wolde, P. R.; Frenkel, D., Computer simulation study of gas-liquid nucleation in a Lennard-Jones system. *Journal of Chemical Physics* **1998,** *109* (22), 9901-9918.

287. Shen, V. K.; Debenedetti, P. G., A computational study of homogeneous liquid-vapor nucleation in the Lennard-Jones fluid. *Journal of Chemical Physics* **1999,** *111* (8), 3581-3589.

288. ten Wolde, P. R.; Ruiz-Montero, M. J.; Frenkel, D., Numerical calculation of the rate of homogeneous gas-liquid nucleation in a Lennard-Jones system. *Journal of Chemical Physics* **1999,** *110* (3), 1591-1599.

289. Chen, B.; Siepmann, J. I.; Oh, K. J.; Klein, M. L., Aggregation-volume-bias Monte Carlo simulations of vapor-liquid nucleation barriers for Lennard-Jonesium. *Journal of Chemical Physics* **2001,** *115* (23), 10903-10913.

290. Valeriani, C.; Sanz, E.; Frenkel, D., Rate of homogeneous crystal nucleation in molten NaCl. *Journal of Chemical Physics* **2005,** *122* (19).

291. Allen, R. J.; Valeriani, C.; ten Wolde, P. R., Forward flux sampling for rare event simulations. *Journal of Physics-Condensed Matter* **2009,** *21* (46).

292. Li, T.; Donadio, D.; Galli, G., Nucleation of tetrahedral solids: A molecular dynamics study of supercooled liquid silicon. *Journal of Chemical Physics* **2009,** *131* (22).

293. Wang, Z.-J.; Valeriani, C.; Frenkel, D., Homogeneous Bubble Nucleation Driven by Local Hot Spots: A Molecular Dynamics Study. *Journal of Physical Chemistry B* **2009,** *113* (12), 3776-3784.

294. Bi, Y.; Li, T., Probing Methane Hydrate Nucleation through the Forward Flux Sampling Method. *Journal of Physical Chemistry B* **2014,** *118* (47), 13324-13332.

295. Meadley, S. L.; Escobedo, F. A., Thermodynamics and kinetics of bubble nucleation: Simulation methodology. *Journal of Chemical Physics* **2012,** *137* (7).

296. Bellucci, M. A.; Trout, B. L., Bezier curve string method for the study of rare events in complex chemical systems. *Journal of Chemical Physics* **2014,** *141* (7).

297. Qiu, C.; Qian, T.; Ren, W., Application of the string method to the study of critical nuclei in capillary condensation. *Journal of Chemical Physics* **2008,** *129* (15).

298. He, X.; Shen, Y.; Hung, F. R.; Santiso, E. E., Molecular simulation of homogeneous nucleation of crystals of an ionic liquid from the melt. *The Journal of chemical physics* **2015,** *143* (124506).

299. Humphrey, W.; Dalke, A.; Schulten, K., VMD: Visual molecular dynamics. *Journal of Molecular Graphics & Modelling* **1996,** *14* (1), 33-38.

300. Chunsrivirot, S.; Santiso, E.; Trout, B. L., Binding Affinity of a Small Molecule to an Amorphous Polymer in a Solvent. Part 2: Preferential Binding to Local Sites on a Surface. *Langmuir* **2011,** *27* (20), 12396-12404.

301. Rogers, F. D., *An Introduction to NURBS with Historical Perspective*. Morgan Kaufmann: San Francisco, 2001.

302. Singh, R.; Rajput, N. N.; He, X. X.; Monk, J.; Hung, F. R., Molecular dynamics simulations of the ionic liquid EMIM+ TFMSI- confined inside rutile (110) slit nanopores. *Physical Chemistry Chemical Physics* **2013,** *15* (38), 16090-16103.

303. He, X.; Monk, J.; Singh, R.; Hung, F. R., Molecular modeling of ionic liquids in the ordered mesoporous carbon CMK-5. *molecular simulation* **2015,** *In press*.

304. Hung, F. R.; Coasne, B.; Santiso, E. E.; Gubbins, K. E.; Siperstein, F. R.; Sliwinska-Bartkowiak, M., Molecular modeling of freezing of simple fluids confined within carbon nanotubes. *Journal of Chemical Physics* **2005,** *122* (14), 14.

Appendix A Letters of Permission

The Chapter 2 is reproduced with permission from a research paper published on *Molecular simulation*: He, X.; Monk, J.; Singh, R.; Hung, F. R., Molecular modeling of ionic liquids in the ordered mesoporous carbon CMK-5. *Molecular Simulation*, 2015, DOI:10.1080/08927022.2015.1089992

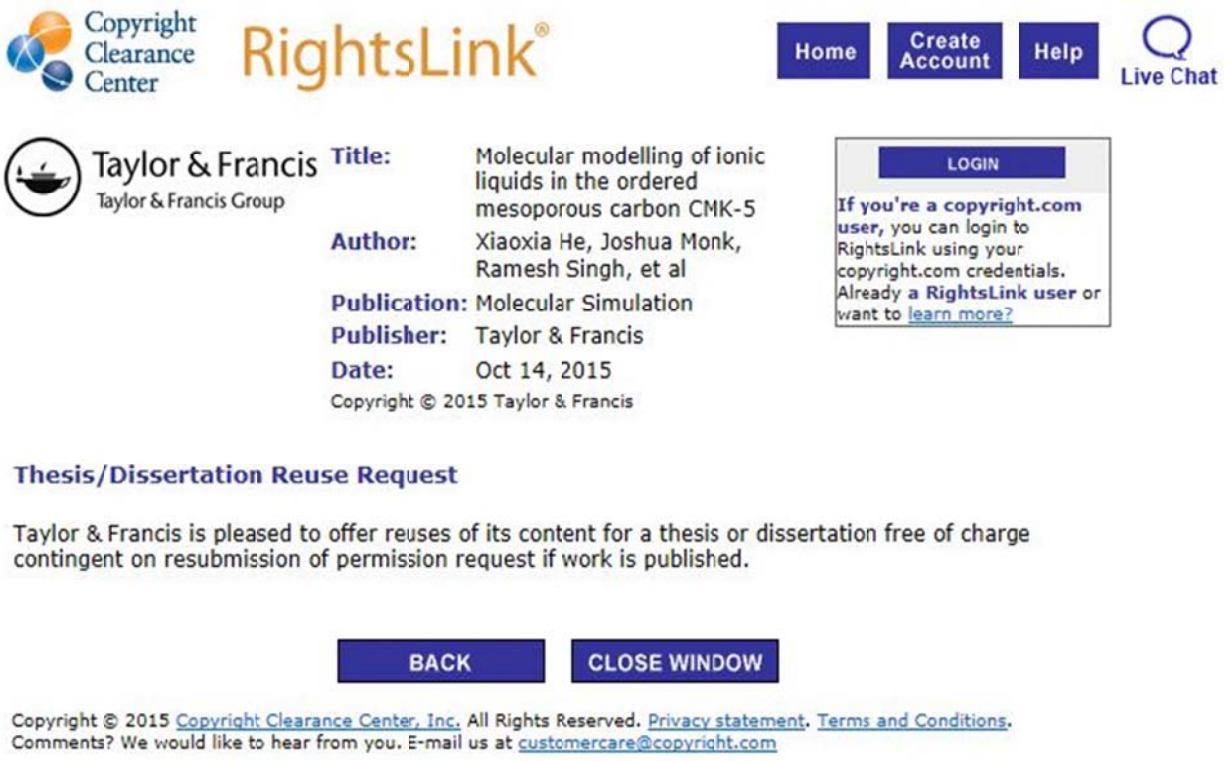

Figure A1 The approval letter of rewriting Chapter 2 by a published research paper in *Molecular simulation.*

The Chapter 3 is reproduced with permission from the research paper published on Journal of chemical physics: He, X.; Shen, Y.; Hung, F. R.; Santiso, E. E., Molecular simulation of homogeneous nucleation of crystals of an ionic liquid from the melt. *J. Chem.Phys.* **2015,** 143, 124506

AIP PUBLISHING LLC LICENSE
TERMS AND CONDITIONS

Oct 08, 2015

All payments must be made in full to CCC. For payment instructions, please see information listed at the bottom of this form.

License Number	3724250035550
Order Date	Oct 08, 2015
Publisher	AIP Publishing LLC
Publication	Journal of Chemical Physics
Article Title	Molecular simulation of homogeneous nucleation of crystals of an ionic liquid from the melt
Author	Xiaoxia He,Yan Shen,Francisco R. Hung, et al.
Online Publication Date	Sep 29, 2015
Volume number	143
Issue number	12
Type of Use	Thesis/Dissertation
Requestor type	Author (original article)
Format	Electronic
Portion	Excerpt (> 800 words)
Will you be translating?	No
Title of your thesis / dissertation	Applications of Molecular Dynamics Simulations on Studying Structure, Dynamics and Crystallization of Ionic Liquids under Confinement and Low Temperature
Expected completion date	Dec 2015
Estimated size (number of pages)	150
Total	0.00 USD

Terms and Conditions

AIP Publishing LLC -- Terms and Conditions: Permissions Uses

Figure A2 The approval letter of rewriting Chapter 3 by a published research paper in *J. Chem.Phys.*

The Chapter 4 is reproduced from the conference proceeding on Molecular Modeling and the Materials Genome (FOMMS): He, X.; Shen, Y.; Hung, F. R.; Santiso, E. E., homogeneous nucleation of [dmim+][Cl-] from its supercooled liquid phase. **2015,** submitted

Appendix B Material Related to Chapter 2

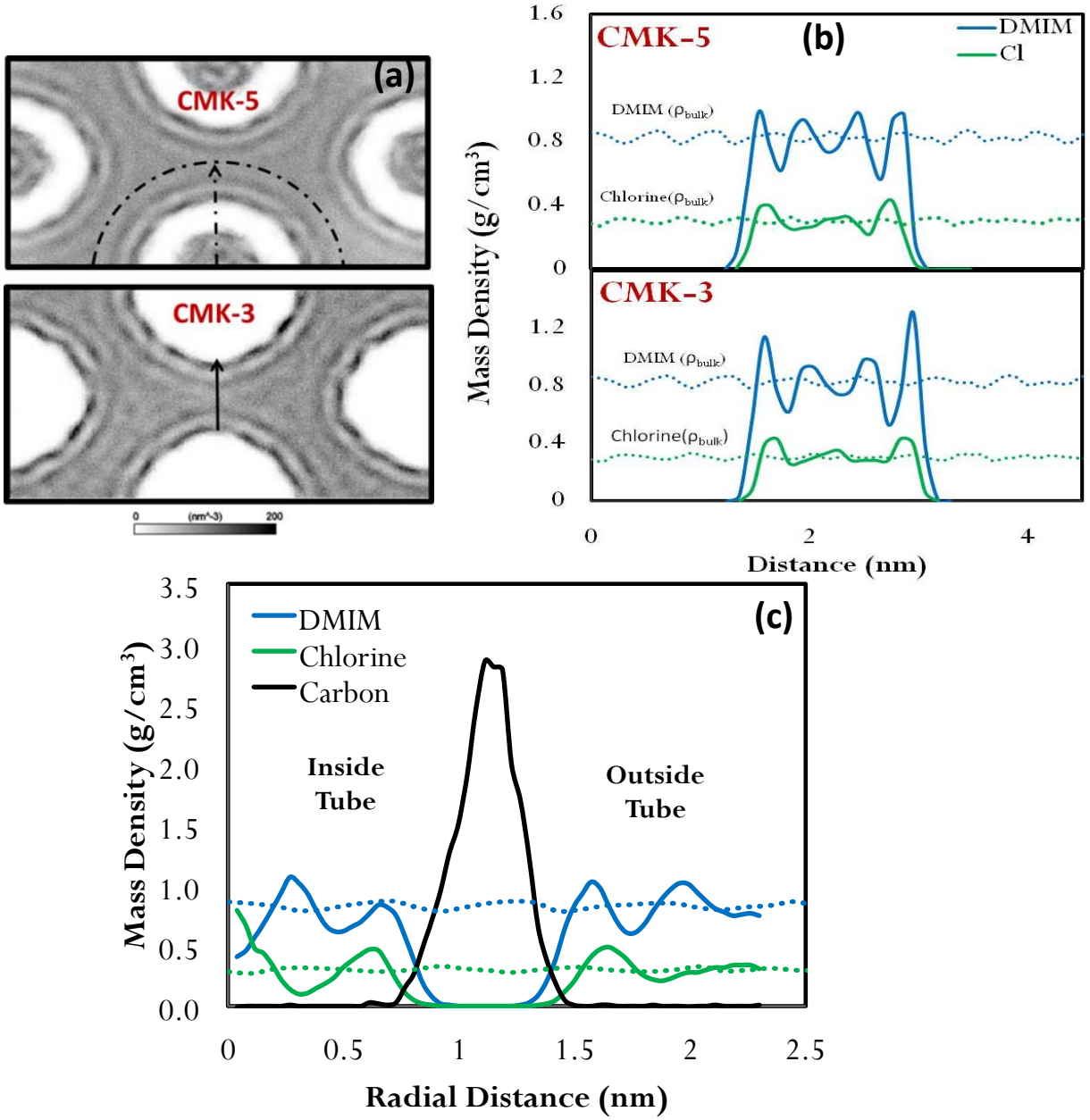

Figure B1 (a) Density map of the [dmim$^+$] cations inside the model CMK-5 and CMK-3 materials (H = 1.8 nm). Areas with higher density of cations are depicted in darker shades of grey. (b) Density profiles of [dmim$^+$][Cl$^-$] outside the carbon nanopipes of CMK-5 or the carbon nanorods of CMK-3, along the shortest pore distance (indicated by the solid arrow in the CMK-3 density map, bottom of Figure B1a). (c) Density profile of [dmim$^+$][Cl$^-$] inside and outside the ACNPs of CMK-5, where distance zero represents the center of the ACNP (indicated by the dashed arrow in the CMK-5 density map, top of Figure B1a).

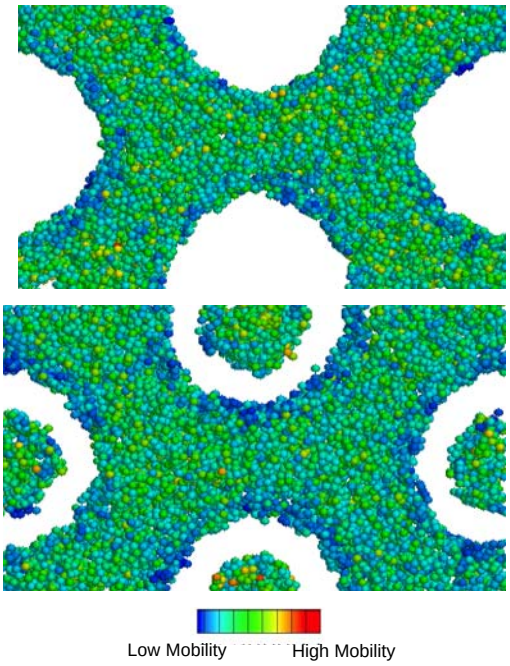

Figure B2 Representative simulation snapshots of [dmim$^+$][Cl$^-$] inside the CMK-3 (top) and CMK-5 (bottom) model materials. The ions are colored according to their displacement over a time of 10 ns. Carbon atoms in CMK-3 and CMK-5 are not shown.

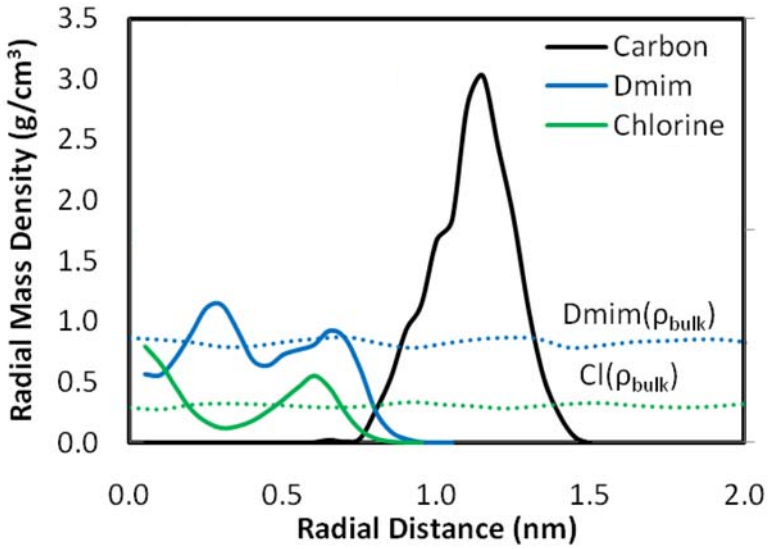

Figure B3 Mass density profile in the radial direction for [dmim$^+$][Cl$^-$] inside an isolated ACNP. The dotted line represents the cation and anion densities in a simulated bulk IL system.

Appendix C Material Related to Chapter 3

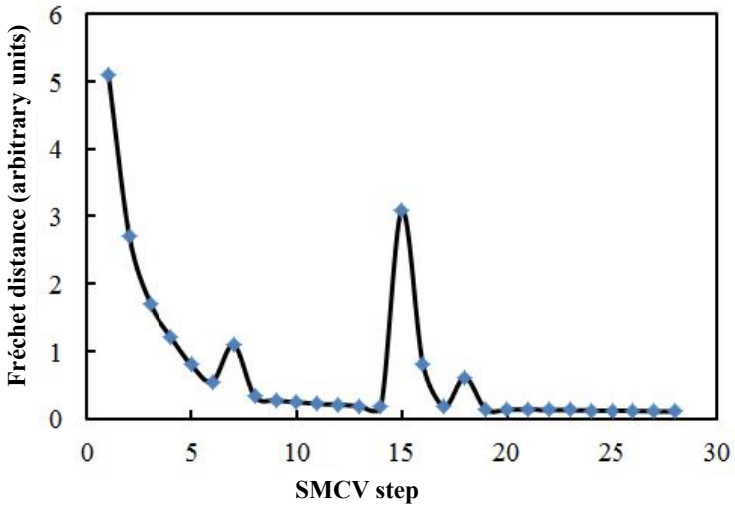

Figure C1 Fréchet distance between PMF curves obtained in successive SMCV steps. To accelerate the convergence of the SMCV method, we redistributed the images manually before steps 7, 15 and 18, which produced the sudden increases in the Fréchet distances in those steps.

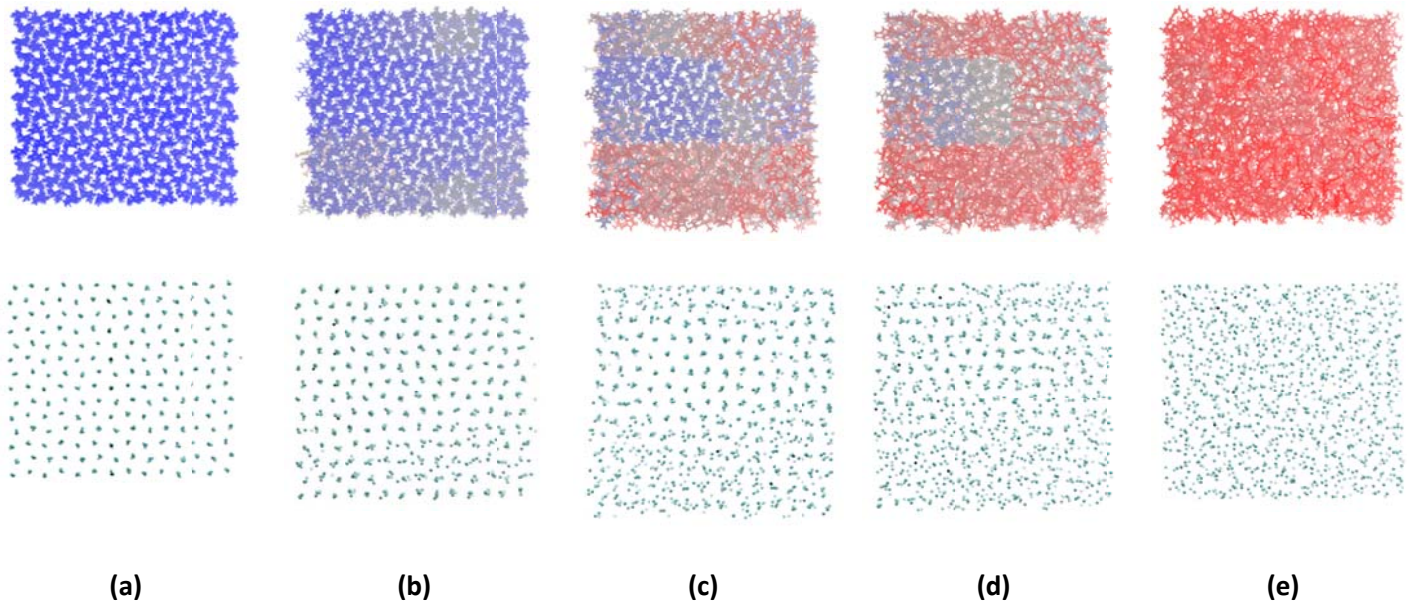

Figure C2 Side views (*x*-*y*) of representative simulation snapshots of relevant states along the MFEP mapped in Figure 3 (system with 1372 ion pairs). Cations are color-coded using the same criteria as in Figure 3.4.

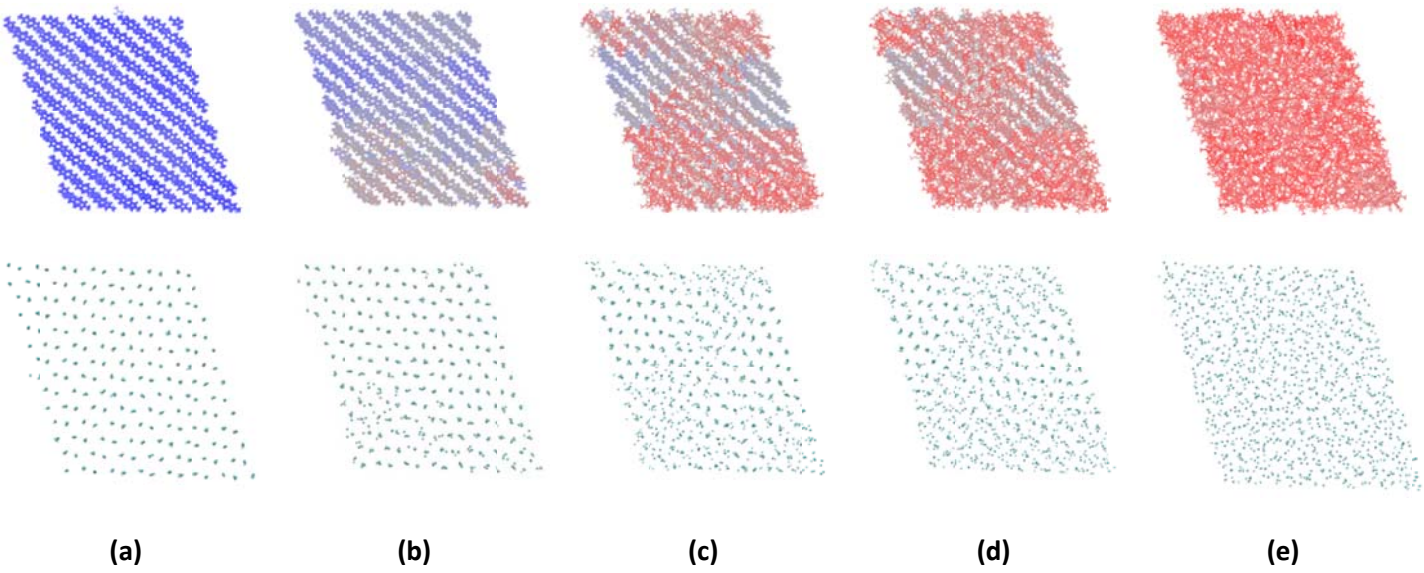

Figure C3 Side views (*x*-*z*) of representative simulation snapshots of relevant states along the MFEP mapped in Figure 3 (system with 1372 ion pairs). Cations are color-coded using the same criteria as in Figure 3.4.

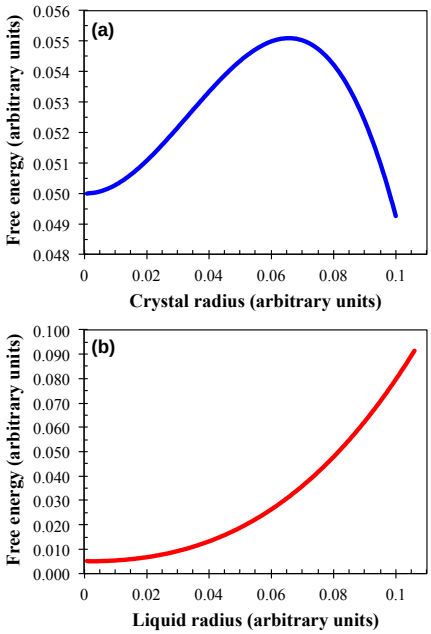

Figure C4 Classical nucleation theory (CNT) calculation of the free energy of (a) a crystal nucleating within a liquid phase, and (b) a liquid nucleating within a solid phase. The free energies are plotted as a function of the radius of the crystal or liquid nucleus. The model system is at a temperature below its melting point.

Vita

Xiaoxia He was born in 1986 in Anyang, Henan Province, China. She completed his high school at Neihuang High School in 2004. In the same year, she joined Henan University of Science and Technology. She received her Bachelor's degree in Chemical Engineering in July 2010. From August, 2008 to May, 2010, she spent two years in Tianjin University as a graduate student. In 2010, she was issued the Master's degree majoring in Industrial Catalysis the Chmical Engineering Department of Tianjin University. In 2010, she joined the Chemical Engineering Department at Louisiana State University (LSU). She has been working on the research projects related to molecular modeling of ionic liquids in LSU under the supervision of Prof. Francisco Hung.